TECHNISCHE UNIVERSITÄT WIEN

ATOMINSTITUT

Diploma Thesis

Application of total reflection x-ray fluorescence analysis down to carbon

---

DIPLOMARBEIT

Anwendung von Totalreflektions-Röntgenfluoreszenzanalyse von leichten Elementen bis zum Kohlenstoff

ausgeführt zum Zwecke der Erlangung des akademischen Grades eines / einer
Diplom-Ingenieurs/ Diplom-Ingenieurin
eingereicht an der Technischen Universität Wien, Fakultät für Physik

von

Dragic Krstajic
Matr.Nr.: 01630084

unter der Anleitung von

Ao. Univ.-Prof. Dipl.-Ing. Dr.techn. Christina Streli
Ao. Univ.-Prof.iR Dr. Peter Wobrauschek

Atominstitut
der Technischen Universität Wien,
Stadionallee 2, 1020 Wien

Wien, im Mai 2022

Abstract

Light element analysis with Total Reflection X-Ray Fluorescence (TXRF) is a rapidly developing field of x-ray fluorescence analysis, and offers many advantages to commercially available x-ray- and particle-based systems. To test the limits of this technique and assess its potential for mineralogical and environmental studies, two different sets of samples were measured and quantified.

The first part of this work focuses on the measurement and quantification of polystyrene spheres, prepared in cooperation with the University of Utrecht. Various sizes of polystyrene spheres were spin coated in various densities, first on silicon, and then on quartz wafers, and then measured and quantified. While the interpretation of results is rather challenging, the technique shows definitive promise in measuring the presence of nanoplastics, as well as differentiating between different sizes of these particles.

The second part of this work revolves around the analysis of aluminosilicate rock samples, in cooperation with I. Allegretta from the University of Bari. A set of six different certified reference materials were prepared in suspension and pipetted onto clean quartz wafers, with silver added as an internal standard. These samples were then measured, and the calibration data obtained was used to quantify three other certified reference materials for validation. The results for the analyzed elements (fluorine to iron) showed good values, with a few exceptions, and demonstrated the viability of TXRF as a tool in mineralogical and geological studies.

Based on both of these endeavors, it is surmised that a properly optimized TXRF spectrometer can successfully be employed in light element analysis down to carbon. Thanks to the ease of sample preparation and operation, exceptional sensitivity, as well cost efficiency, TXRF can be recommended as a fast, relatively cheap, and reliable quantification method, especially when it comes to the lightest elements.

Kurzfassung

Die Analyse leichter Elemente mit Totalreflektions-Röntgenfluoreszenzanalyse (TXRF) ist ein sich schnell entwickelndes Gebiet der Röntgenfluoreszenzanalyse und bietet viele Vorteile gegenüber kommerziell erhältlichen röntgen- und partikelbasierten Systemen. Um die Leistungsfähigkeit dieser Technik zu testen und ihr Potenzial für mineralogische und Umweltstudien zu bewerten, wurden zwei verschiedene Probenarten gemessen und quantifiziert.

Der erste Teil dieser Arbeit konzentriert sich auf die Messung und Quantifizierung von Polystyrol-Nanopartikel, die in Zusammenarbeit mit der Universität Utrecht erstellt wurden. Verschiedene Größen von Polystyrol-NanoPartikel wurden in verschiedenen Dichten zuerst auf Silizium und dann auf Quarzwafer durch spincoating Technik aufgebracht, dann gemessen und quantifiziert. Die Technik ist definitiv vielversprechend, um das Vorhandensein von Nanoplastik zu messen und zwischen verschiedenen Größen dieser Partikel zu unterscheiden, die detailiierte Interpretation der Ergebnisse ist allerdings nicht trivial.

Der zweite Teil dieser Arbeit behandelt die Analyse von Alumosilikat-Gesteinsproben in Zusammenarbeit mit I. Allegretta von der Universität Bari. Ein Satz von sechs verschiedenen zertifizierten Referenzmaterialien wurde in Suspension hergestellt und auf saubere Quarzwafer pipettiert, wobei Silber als interner Standard hinzugefügt wurde. Diese Proben wurden gemessen und damit eine Kalibrierung erstellt, drei weitere zertifizierte Referenzmaterialien wurden für die Validierung verwendet. Die Ergebnisse für die analysierten Elemente (Fluor bis Eisen) zeigten mit wenigen Ausnahmen zufriedenstellende Werte, wodurch die die Anwendbarkeit der TXRF mineralogischen und geologischen Studien gezeigt werden konnte.

Dank der einfachen Probenvorbereitung, der außergewöhnlichen Empfindlichkeit, sowie der Kosteneffizienz kann TXRF als schnelle, relativ kostengünstige und zuverlässige Quantifizierungsmethode empfohlen werden, auch für die Analyse leichter Elemente bis zu Kohlenstoff.

Acknowledgements

This work would not come to be without the help and support of many people. I would like to express my gratitude to each and every one of them:

Ao. Univ.-Prof. Dipl.-Ing. Dr. Christina Streli for her mentorship, guidance and support, both academically as well as professionally.

Ao. Univ.-Prof.iR. Dr. Peter Wobrauschek for his unending enthusiasm about x-ray physics, boundless wealth of knowledge and experience, and a down-to-earth approach to problem solving.

Dipl.-Ing. Dr. Peter Kregsamer and *Dipl.-Ing. Dr. Dieter Ingerle* for their constant availability, warm presence and helpful input about parts of work outside of my area of expertise.

Our partners from the University of Utrecht, *Ao. Univ.-Prof. Dr. Florian Meirer* and *Kirsten Siebers* for their diligence, regular communication and help with sample preparation, as well as interpretation of results.

And finally, my *fiancée*, as well as my *friends and family* for all their support, love and care.

Contents

1 Motivation

Environmental problems, especially the pollution of soil, water and atmosphere, are ever present in the modern human society, and grow in importance and urgency by the year. While the impact of human civilization on the ecosphere grows exponentially, the tools at our disposal to deal with the issue at hand are also being developed at an accelerating pace.

One of the issues being actively tackled at the moment is the permeation of pollutants through water and soil. The most notable among them is plastic, or more specifically nano- and microplastics, the end products of slow plastic breakdown over time. Difficult to detect, and yet more challenging to filter out of the environment, nanoplastics are poised to become a serious issue affecting the entire biosphere if not handled correctly, and soon. On the other hand, other types of pollutants exist in the soil as well, and once again, adequate chemical analytical tools are required to properly detect and quantify the wide range of elements relevant for environmental studies of these samples.

The analysis of light elements with x-rays is notoriously difficult due to the many fundamental laws of x-ray physics severely limiting the excitation, emission and detection of x-ray fluorescence in light elements. Special optimizations need to be in place for light elements to be properly detected and quantified, and total reflection x-ray fluorescence analysis (TXRF) lends itself well to this issue due the high intensities of exciting x-rays it guarantees through total external reflection. To investigate the possibility and feasibility of using TXRF for to fit these roles, a TXRF spectrometer at Atominstitut will be used to measure different samples containing light elements.

The results of this work form the basis for future advancements in the field, and more specifically the building of a new TXRF spectrometer in Utrecht, Netherlands. The end goal of the new spectrometer is the quantification of carbon in real seawater samples, and this work aims to be a proof of concept, as well as a working prototype based on which recommendations for further optimizations which can be made.

2 Theory

This chapter deals with the theoretical knowledge necessary to fully understand the theme of this work. It covers the basics of X-ray generation and interaction with matter, beam optics, physics of fluorescence and detector function. This should give an insight into the core principles of X-ray fluorescence analysis and why its use for the quantification of light elements is such a challenge.

2.1 X-ray generation

X-rays are conventionally defined as photons with energies comparable to the energies of quantum states of an atom's electron hull, which is to say between 0.1 and 100 keV. These photons are most often generated in so-called *X-ray tubes*.

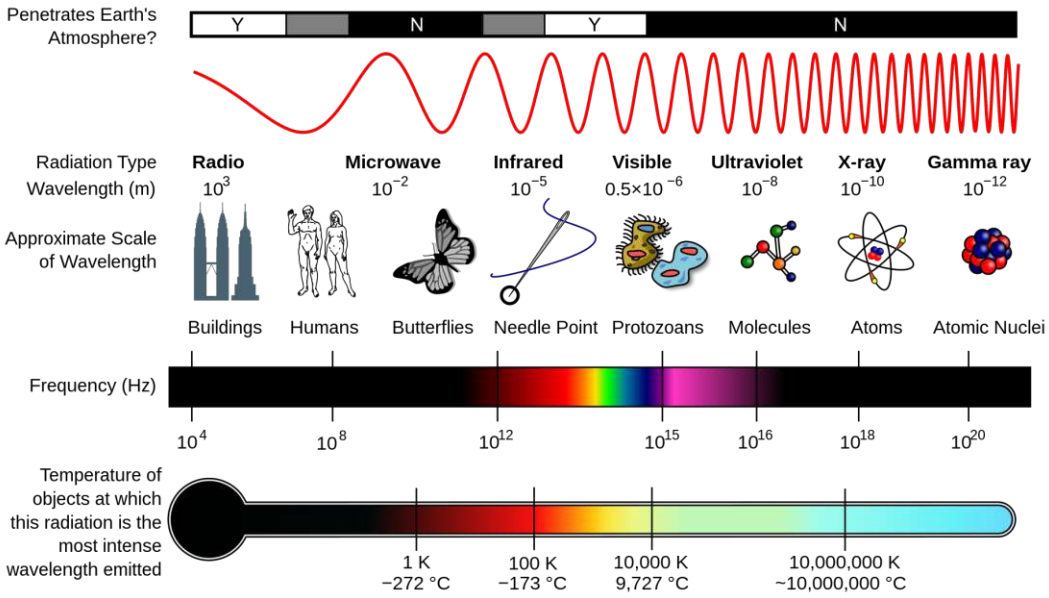

Figure 1: A visualization of the electromagnetic spectrum, showing the wavelength and wavelength examples, frequency and black body emission temperature. Figure from Ref. [6]

X-ray tubes consist of an evacuated cylinder with a beryllium exit window encasing a pair of electrodes. The cathode is usually a heated piece of wire that emits electrons via thermal emission, while the anode is made of copper and coated in another metallic material. The x-ray spectrum that the tube emits depends greatly on the choice of material for the metallic anode.

The electrodes are kept under an electrostatic voltage, with the power supplied by an external x-ray power generator. The intensity of the voltage is adjusted with regard to the metallic anode being used in the x-ray tube, with higher voltages of up to 150 kV used for

heavier metals like tungsten, and lower voltages of down to 30 kV for lighter metals like chrome. This voltage accelerates the electrons emitted by the cathode into the metallic anode, where the electrons interact with the atoms of the anode. These interactions are inelastic, and the kinetic energy of the electrons is converted into heat and x-rays. It must be noted that over 99 percent of energy spent on accelerating electrons is converted into heat, with the rest being converted into x-rays. Because of this, the metallic anode must be cooled, usually with water. The rest of the energy goes into generating x-rays, which is done through **bremsstrahlung** and **x-ray fluorescence**.

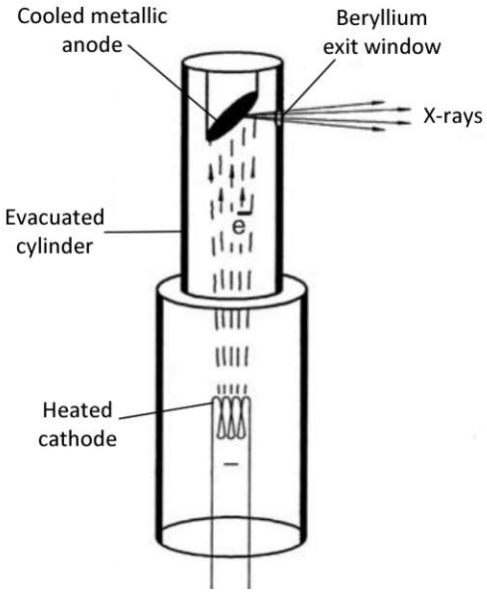

Figure 2: Basic x-ray tube. Text added to a figure from Ref. [1, p. 7]

2.1.1 Bremsstrahlung

Bremsstrahlung refers to the phenomenon of photon emission by an electron that scatters under the influence of an atomic core's Coulomb potential. Due to the probabilistic nature of the distance between the electron and the atomic core, as well as the electron's speed, the energy lost during this interaction is spread over a continuum, and therefore so is the energy of the emitted photons. Therefore, bremsstrahlung forms a *continuous spectrum* of radiation that depends on the kinetic energy of the electrons, and for an accelerating voltage of U has a cut-off at an energy of:

$$E_{photon,max} = eU$$

with e being the elemental charge.

This maximal energy is equivalent to a minimal wavelength of

$$\lambda_{min} = \frac{hc}{eU}$$

where h is the Planck constant, and c the speed of light.

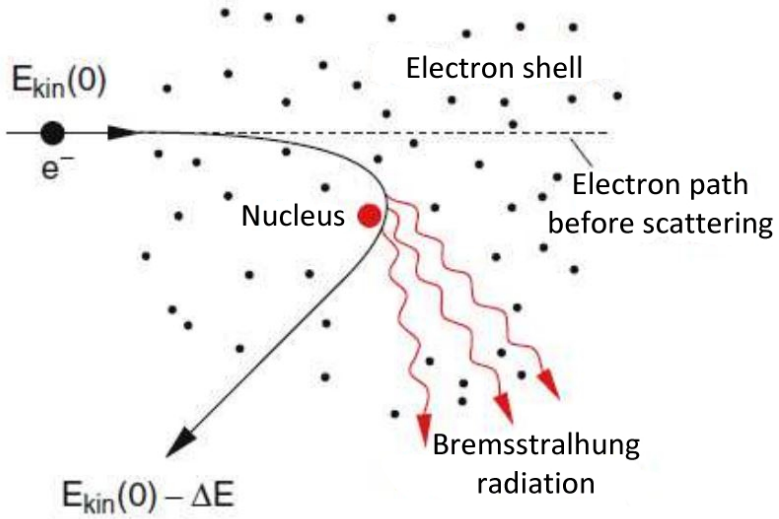

Figure 3: Visualization of the bremsstrahlung phenomenon. Figure taken from Ref. [7, p. 187], with the text translated to english.

2.1.2 X-ray fluorescence and Auger effect

Accelerated electrons can ionize the atoms of the metallic anode through collisions, leading to vacancies in their electron shells which can be filled out through two concurring processes: *X-ray fluorescence* and the *Auger effect*.

X-ray fluorescence refers to the emission of a photon by a higher bound electron transitioning into a vacant lower orbital left behind after ionization. This vacant orbital can be filled by any of the higher bound electrons of an atom, each with a certain probability. In the case of all of them, the emitted photon will have an energy exactly equal to the difference in energy levels the electron occupied before and after the transition. In other words, the energy of the photon follows Moseley's law, and can only assume certain values, which are unique, or characteristic, to the element at hand. This is the premise behind *characteristic radiation* which forms a line spectrum of peaks characteristic for the anode material used in an x-ray tube. Together with bremsstrahlung radiation, it forms the complete x-ray spectrum, which is a superposition of the two spectra.

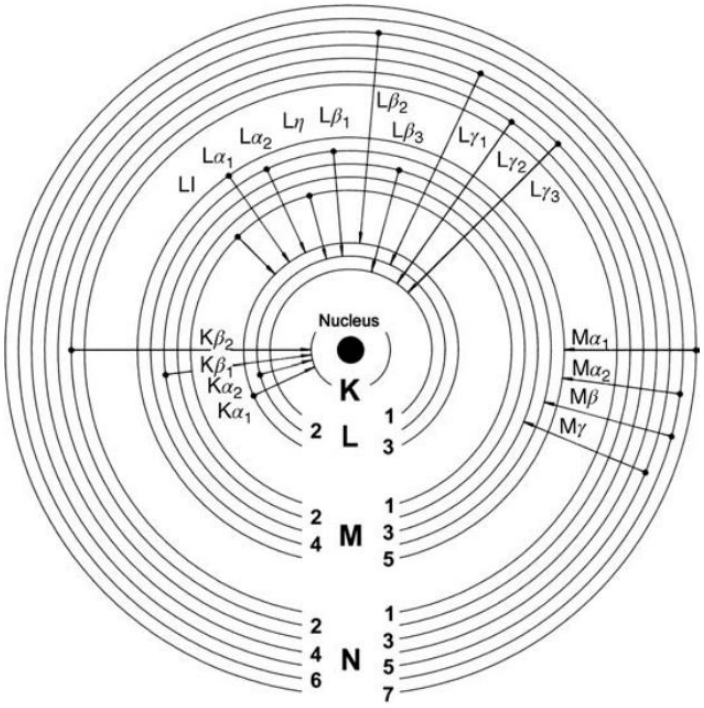

Figure 4: Illustration of the different dipole transitions. Figure from Ref. [1, p. 20]

Siegbahn	IUPAC	Siegbahn	IUPAC	Siegbahn	IUPAC	Siegbahn	IUPAC
$K\alpha_1$	$K–L_3$	$L\alpha_1$	$L_3–M_5$	$L\gamma_1$	$L_2–N_4$	$M\alpha_1$	$M_5–N_7$
$K\alpha_2$	$K–L_2$	$L\alpha_2$	$L_3–M_4$	$L\gamma_2$	$L_1–N_2$	$M\alpha_2$	$M_5–N_6$
$K\beta_1$	$K–M_3$	$L\beta_1$	$L_2–M_4$	$L\gamma_3$	$L_1–N_3$	$M\beta$	$M_4–N_6$
$K\beta_2^{I}$	$K–N_3$	$L\beta_2$	$L_3–N_5$	$L\gamma_4$	$L_1–O_3$	$M\gamma$	$M_3–N_5$
$K\beta_2^{II}$	$K–N_2$	$L\beta_3$	$L_1–M_3$	$L\gamma_4'$	$L_1–O_2$	$M\zeta$	$M_{4,5}–N_{2,3}$
$K\beta_3$	$K–M_2$	$L\beta_4$	$L_1–M_2$	$L\gamma_5$	$L_2–N_1$		
$K\beta_4^{I}$	$K–N_5$	$L\beta_5$	$L_3–O_{4,5}$	$L\gamma_6$	$L_2–O_4$		
$K\beta_4^{II}$	$K–N_4$	$L\beta_6$	$L_3–N_1$	$L\gamma_8$	$L_2–O_1$		
$K\beta_{4x}$	$K–N_4$	$L\beta_7$	$L_3–O_1$	$L\gamma_8'$	$L_2–N_{6,7}$		
$K\beta_5^{I}$	$K–M_5$	$L\beta_8$	$L_3–N_{6,7}$	$L\eta$	$L_2–M_1$		
$K\beta_5^{II}$	$K–M_4$	$L\beta_9$	$L_1–M_5$	Ll	$L_3–M_1$		
		$L\beta_{10}$	$L_1–M_4$	Ls	$L_3–M_3$		
		$L\beta_{15}$	$L_3–N_4$	Lt	$L_3–M_2$		
		$L\beta_{17}$	$L_2–M_3$	Lu	$L_3–N_{6,7}$		
				Lv	$L_2–N_{6,7}$		

Figure 5: X-ray fluorescence listed in the two conventionally used naming systems, that being the IUPAC and Siegbahn nomenclature. Table from Ref. [1, p. 21]

Other than x-ray fluorescence, the vacant state in an atom can be filled through the Auger effect. Instead of producing photons of characteristic energies, the Auger effect results in

electrons with kinetic energies characteristic for the element. The electron transitioning into the original vacant state interacts with another higher bound electron, which is promptly ejected from the atom. This Auger electron carries a kinetic energy equal to

$$E_{kin,Auger} = E_1 - E_2 - E_3$$

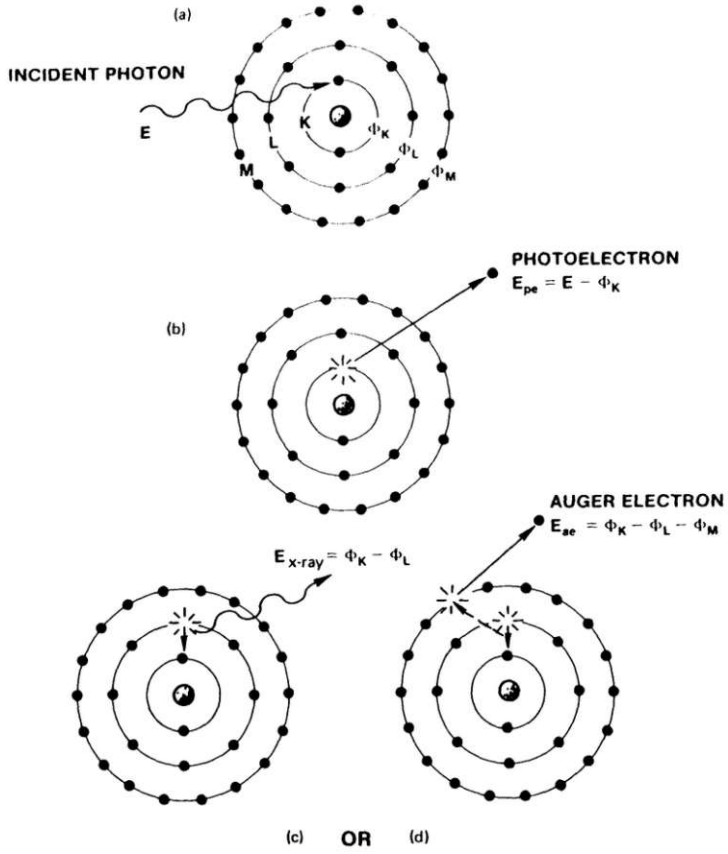

Figure 6: Visual representation of x-ray fluorescence and the Auger effect. Figure from Ref. [8]

Where E_1 is the binding energy of the higher bound electron, E_2 is the energy of the vacant state left behind by the first ejected electron, and E_3 is the binding energy of the Auger electron before ejection. This energy is characteristic for the element, and can form a basis for an analytical metod, called Auger Electron Spectroscopy (AES).

The probability that an atom in an excited state will undergo a radiative decay via x-ray fluorescence, instead of an Auger decay, is defined by the *fluorescence yield* ω_i. The fluorescence yield depends on the element and emission line in question, and is proportional to $Z^4/\left(A+Z^4\right)$. The fluorescence yield and the probability of Auger decay add up to exactly 1. Figure 7 shows the theoretical K line fluorescence yield for different elements plotted against their atomic number Z. For common x-ray tube anode metals like tungsten (Z=74)

and rhodium (Z=45) the fluorescence yield is greater than 0.5, indicating that radiative decays are preferred.

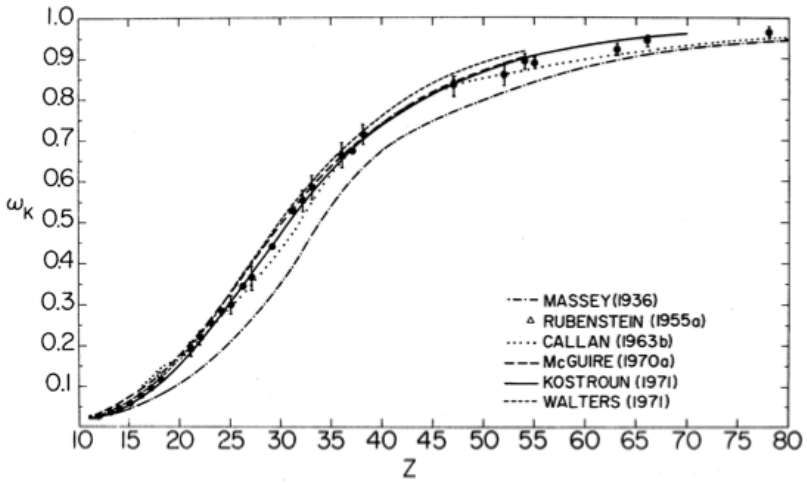

Figure 7: Theoretical K shell fluorescence yield as a function of atomic number, according to various authors: Massey and Burhop (1936), Rubenstein (1955a), Callan (1963b), McGuire (1970a), Kostroun, Chen and Crasemann (1971), and Walter and Bhalla (1971). Figure and description from Ref. [26].

In the case of XRF techniques, Auger electrons are usually an unwanted side-effect of x-ray generation and interaction with matter. They are filtered out together with photoelectrons, secondary electrons ejected through ionization and scattered electrons by the beryllium window, which only lets the x-rays through.

2.1.3 X-ray Spectrum

An x-ray spectrum that is emitted from an x-ray tube is a superposition of the characteristic lines produced via x-ray fluorescence and the continuous spectrum produced via bremsstrahlung. It has a maximal energy (shortest wavelength) as mentioned above at $E_{photon,max} = eU$.

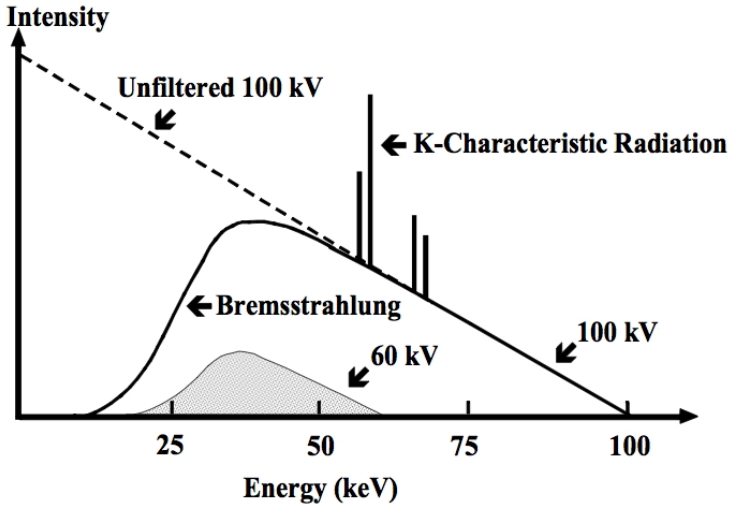

Figure 8: An example x-ray spectrum, showcasing the contributions from the two main processes that generate x-rays. Figure from Ref. [9]

The x-ray spectrum can be different depending on where it is being observed from. Due to the non-zero penetration of the accelerated electrons into the metallic anode, x-rays are being emitted from various depths. The distance traveled through the metallic anode changes with the take-off angle, and this influences the amount of radiation absorbed and scattered by the anode. Besides this, the cross section of the beam can change, depending on where the beryllium window is placed with respect to the metallic anode's incline. In summary, this makes the x-ray spectrum dependent on the position of the window, and opens the possibility for different tube configurations and beam shapes. In the case of this work, a fine focus tube was used.

2.2 X-ray interaction

When passing through matter, X-rays interact with it, causing the initial beam to exponentially lose intensity. This is called *attenuation*, and is caused by a combination of three processes: the *photoelectric effect*, *X-ray scattering* and *pair production*.

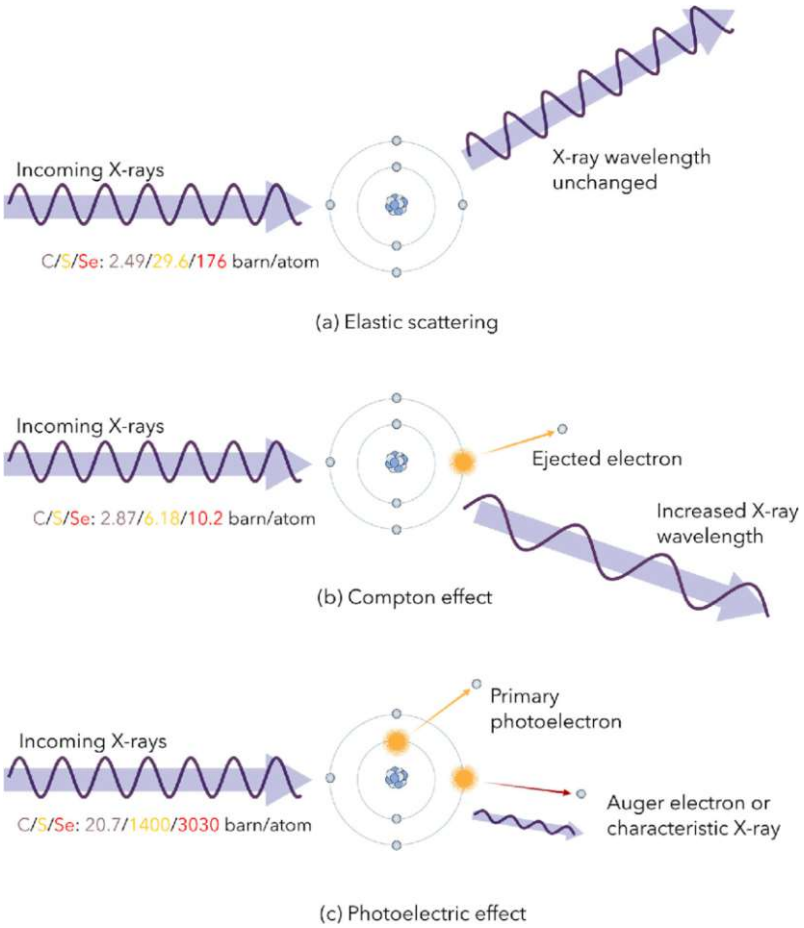

Figure 9: Visualization of the different ways in which x-rays can interact with matter. Figure from Ref. [10]

While absorption and scattering are very important in both XRF and the beam optics used in experiments, pair production is not relevant below an energy threshold of 1 MeV.

2.2.1 X-ray Attenuation

When passing through a homogeneous medium, an x-ray beam exponentially drops in intensity as it is scattered and absorbed by the atoms of that medium. The mathematical expression that desribes this phenomenon is the Beer-Lamber law. Upon passing through a material with a linear attenuation coefficient of μ and thickness d, an x-ray beam with the intensity I_0 will be attenuated to

$$I(d) = I_0 exp^{-\mu d}$$

.

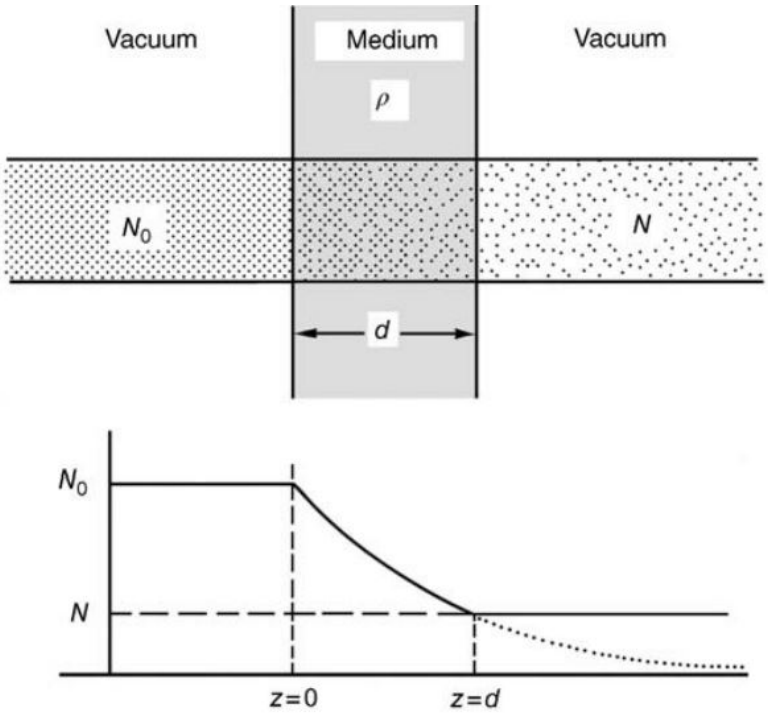

Figure 10: Attenuation of an x-ray beam passing through a homogeneous medium of density ρ and thickness d. The number of photons is reduced exponentially from N_0 to N. Figure and description from Ref. [1, p. 45]

If the medium consists of multiple elements, the total mass attenuation coefficient can be calculated from from the mass attenuation coefficients of the individual elements and their mass fractions.

$$\left(\frac{\mu}{\rho}\right)_{total} = \sum_i c_i \left(\frac{\mu}{\rho}\right)_i$$

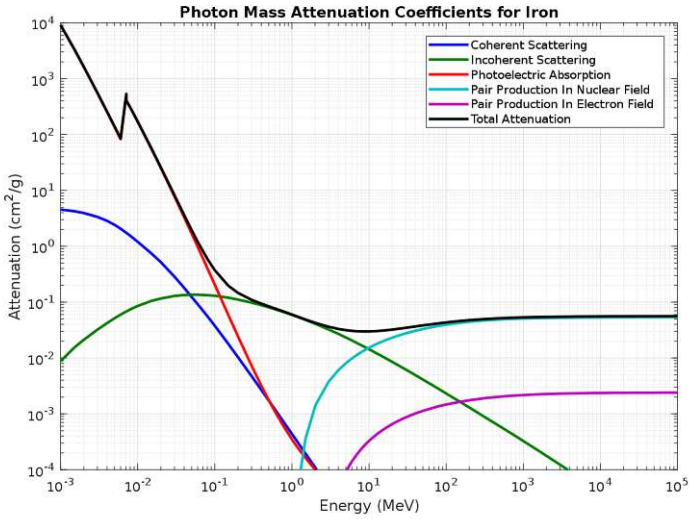

Figure 11: The total mass attenuation coefficient of an atom is equal to the sum of the mass attenuation coefficients of the different contributing interactions. The figure above shows the total mass attenuation coefficient of iron. Figure from Ref. [11]

2.2.2 Photoelectric effect

An incoming X-ray photon can be absorbed by a bound electron, which is promptly ejected from the atom with a kinetic energy equal to the difference between the energy of the incoming photon and its binding energy. The probability for the photoelectric effect to take place depends on the atom's electron structure and the energy of the incoming X-rays. To be absorbed by an electron, the X-ray needs to have a specific minimum energy. Above this energy, the photoelectric cross-section, and therefore the photoelectric mass absorption coefficient of each sub-shell j is described by the *Bragg-Pierce Law*

$$\left(\frac{\tau}{\rho}\right)_j = k_j \frac{Z^3}{E^{8/3}},$$

where k_j is a sub-shell-specific constant, and Z is the atomic number.

As a consequence of this law and minimal energy requirements for different atomic shells, the mass absorption coefficient has characteristic absorption edges, which signify points above which an X-ray has enough energy to ionize a lower, more strongly bound sub-shell.

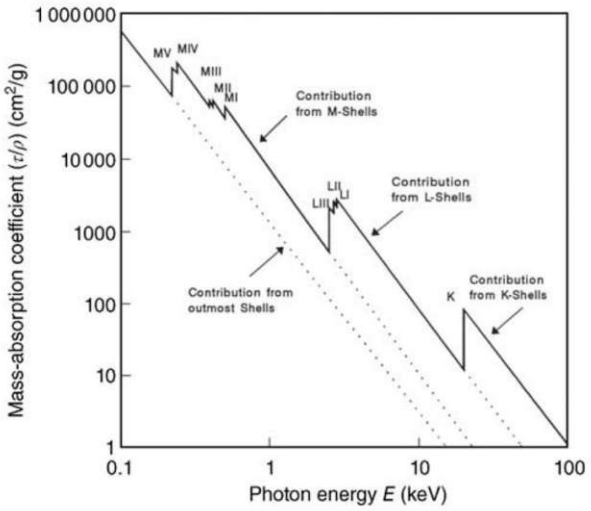

Figure 12: Total photoelectric mass-absorption coefficient (τ/ρ) for molybdenum vs. the photon energy E. Each discontinuity corresponds to an additional photoelectric process that occurs if the respective absorption edge K, L_I ...L_{III}, or M_I ...M_V is exceeded or jumped over. Figure and description from Ref. [1, p. 47]

Photoelectric absorption is the most important process for XRF analytical methods, as it produces excited atoms which can then decay via x-ray fluorescence or Auger effect, as mentioned previously. As stated above, x-ray fluorescence produces characteristic x-ray radiation, which is unique for every element, and this forms the basis of all XRF analytical methods. The mathematics behind this process, as well as the factors that influence it will be discussed in more detail later.

2.2.3 X-ray Scattering

There are three types of scattering that an X-ray can undergo:

- Elastic (Rayleigh) scattering.
- Inelastic (Compton) scattering.
- Inelastic Raman scattering, which has a negligible cross. section outside of resonant cases that are of no importance to this work

Elastic scattering occurs when an X-ray photon interacts with a strongly bound inner electron without any transfer of energy or excitation. The X-ray photon merely changes direction, and this phenomenon forms the basics of X-ray optics, which will be discussed in the next subsection.

Inelastic scattering occurs between an X-ray photon and a loosely bound electron. The x-ray photon transfers a part of its energy onto the electron, which is knocked out of its

bound state. By following the rules of conservation of energy and momentum, we can derive the photon energy change $E_{\gamma'}/E_{\gamma}$ depending on the scattering angle θ and the initial photon energy E_{γ}.

$$\frac{E_{\gamma'}}{E_{\gamma}} = \frac{1}{1 + \left(E_{\gamma}/m_e c^2\right)\left(1 - \cos\theta\right)}$$

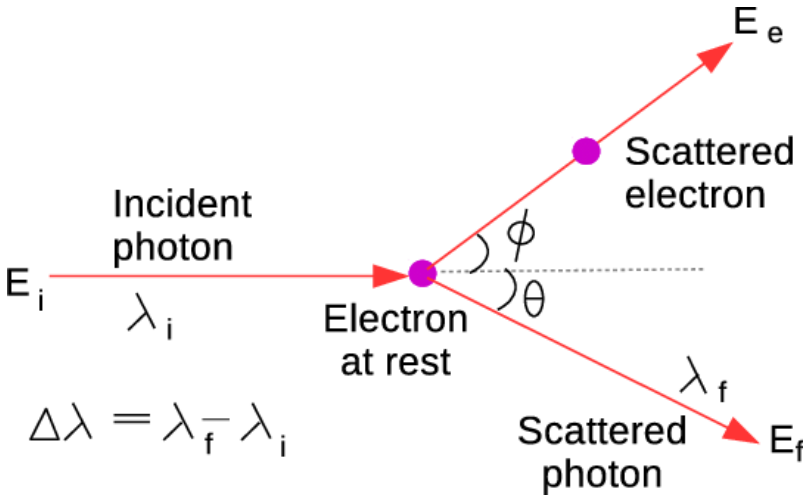

Figure 13: The Compton effect. Figure from Ref. [12]

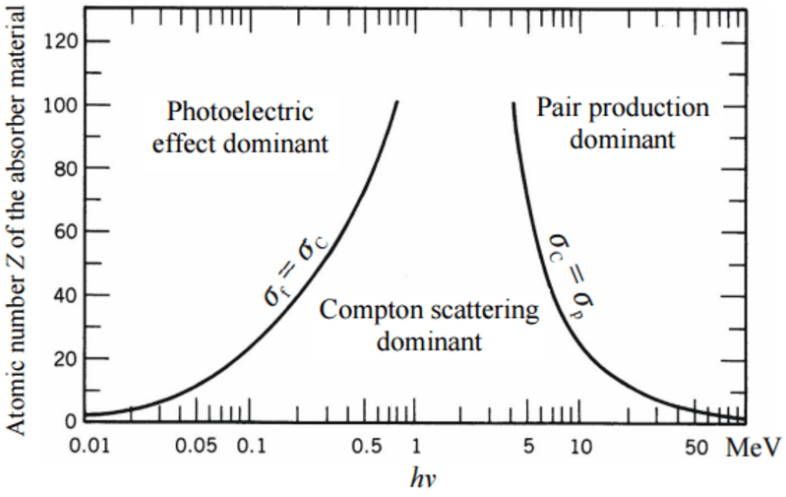

Figure 14: Predominant interaction for different elements, at different photon energies. Figure from Ref. [13]

2.3 X-ray optics

Like any form of electromagnetic radiation, x-rays experience *refraction* and *reflection* when passing from one medium into another. Refraction of electromagnetic radiation follows Snellius' law, which dictates the angle change of a refracted beam based on the refraction

indices of the two media. When passing through two media with refractive indices n_1 and n_2, the glancing angles of an x-ray beam in the two respective media follow the relation

$$n_1 \cos \alpha_1 = n_2 \cos \alpha_2$$

It should be noted that this equation uses the *glancing* angle values, which are complements of incident angles regularly used in optics. This is a matter of convention and convenience, as the glancing angles for x-rays are usually small, making them easier to work with as opposed to the incident angles which are close to 90°.

Reflection is bound by an even simpler law, which states that electromagnetic radiation (including x-rays) is reflected under the same angle as the incident beam.

$$\alpha_1 = \alpha_1'$$

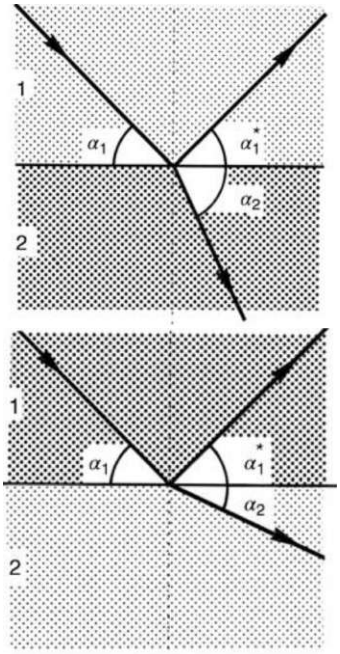

Figure 15: Illustration of reflection and refraction of an electromagnetic beam passing through media 1 and 2. Above, medium 2 is optically denser than medium 1 ($n_2 > n_1$). Below, the opposite is true. Figure from Ref. [1, p. 53]

2.3.1 Refractive index for x-rays

The *refractive index* describes the macroscopic optical behavior of a material, and can be described with the following relation:

$$n = 1 - \delta - i\beta$$

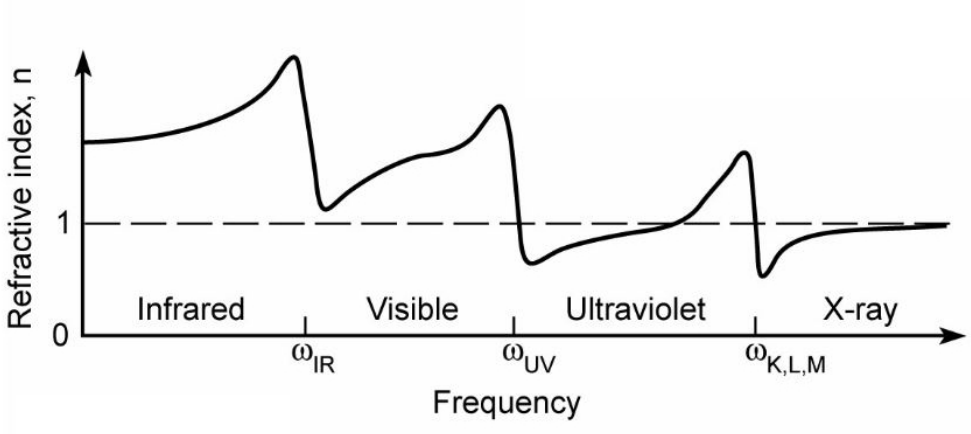

Figure 16: Example behavior of a medium's refractive index depending on the energy of the electromagnetic radiation. Figure from Ref. [14]

The imaginary part of the refractive index is tied to absorption, and can be expressed with

$$\beta = \frac{\lambda}{4\pi}\left(\frac{\mu}{\rho}\right)_{total}\rho$$

The real part is described by the *decrement*, which quantifies the deviation of the real part of the refractive index from unity. The decrement can be approximated as

$$\delta = \frac{N_A}{2\pi} r_{el} \frac{Z}{A} \rho \lambda^2$$

Which can be simplified into a multiplication of the square of the wavelength with a material constant C_m

$$C_m = \frac{N_A}{2\pi} r_{el} \frac{Z}{A} \rho$$

$$\delta = C_m \lambda^2$$

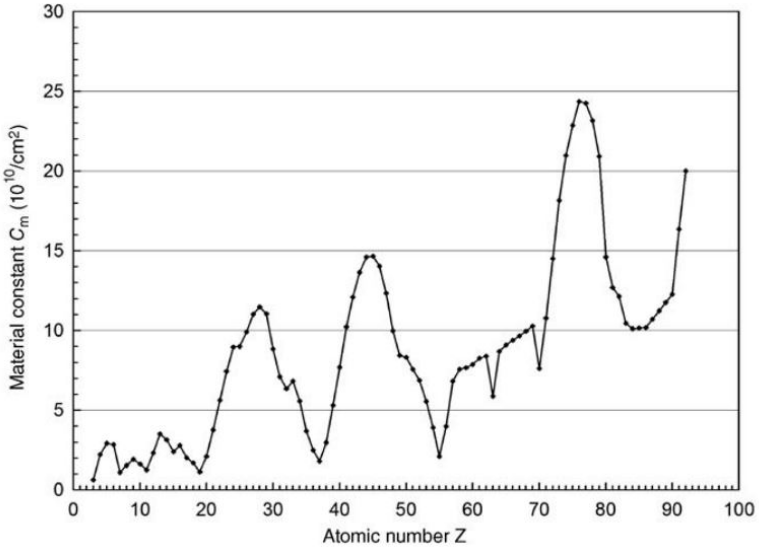

Figure 17: Material constant C_m calculated for different pure elements with atomic number Z. The maxima at Z = 14, 28, 45 and 77 reflect a small volume of the respective atoms while the minima at Z = 11, 19, 37, 55 and 85 occur for relatively large atoms (alkali metals). Figure and description from Ref. [1, p. 59]

Calculating the decrement for the wavelengths of x-rays results in very low values, which in turn makes the real part of the refractive index very slightly less than 1.

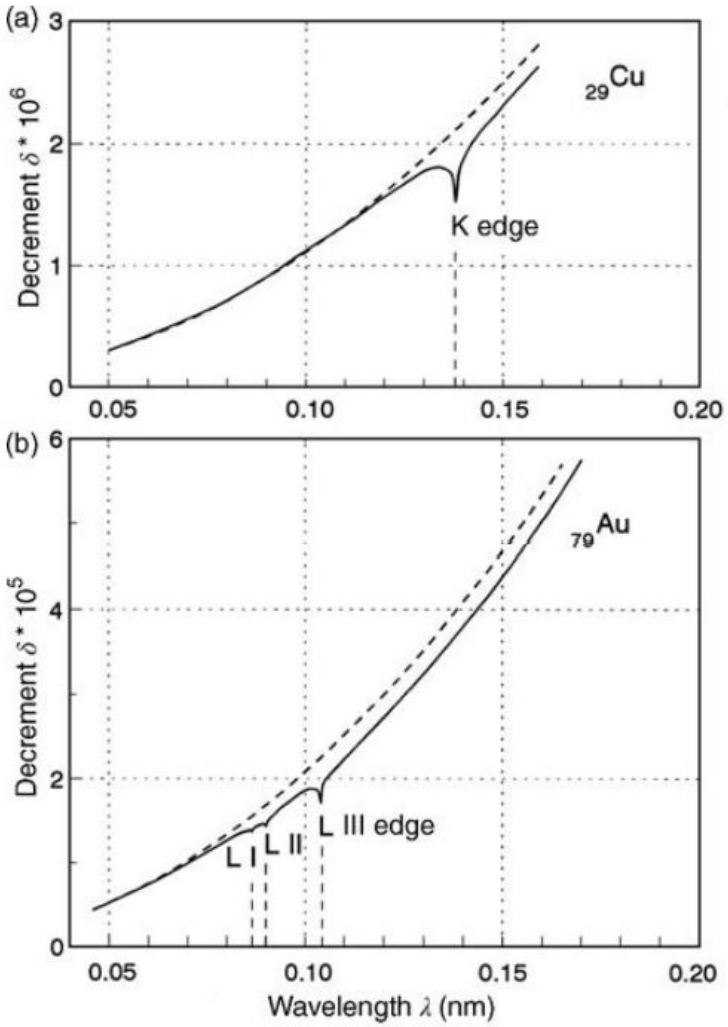

Figure 18: Dependence of the decrement δ on the wavelength λ for the elements (a) copper and (b) gold. The theory is based on forced oscillations of the atomic electrons - forced by the electromagnetic radiation of x-rays. At the "resonance" wavelengths of absorption edges, the decrement shows a strong variation. The asymptotic approximation for short wavelengths is represented by a dashed line. Figure and description from Ref. [1, p. 56]

2.3.2 Total external reflection

Total external reflection refers to a subset of total reflection, wherein an incoming electromagnetic wave is completely reflected on the border surface between an optically dense and optically thin medium, with none of the wave penetrating the optically thin medium. For visible light, total reflection is most often observed in water, which is optically more dense than air, and as such totally reflects light under a certain angle. If we consider the case of light passing from air/vacuum with a refractive index of $n_1 = 1$ into an optically denser medium

with an index of $n_2 > n_1$, and assume the refracted beam has the largest angle possible at 90 degrees, we get

$$\underbrace{n_1}_{=1 \text{ for air/vacuum}} \cos\alpha_1 = n_2 \cos 0°$$

$$\cos\alpha_1 = n_2$$

$$\alpha_1 = \phi_{crit} = \arccos n_2$$

The glancing angle that produces a refraction angle of 0 degrees is the critical angle, and any angle less than that (or greater if viewed as the incident angle used in regular optics) results in total reflection. For visible light, this is referred to as total *internal* reflection, as it takes place on the "inside" of an optically dense medium.

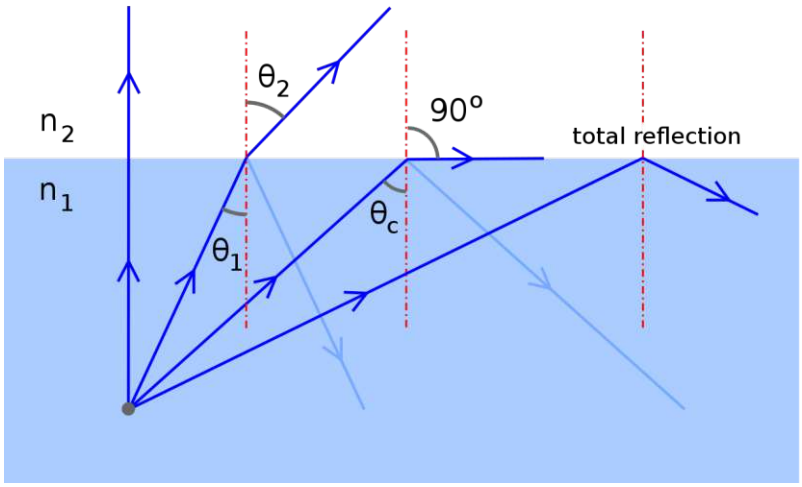

Figure 19: Behavior of a ray incident from a medium of higher refractive index n_1 to a medium of lower refractive index n_2, at increasing angles of incidence. Figure and description from Ref. [15]

Due to the nature of the refractive index for x-rays discussed above, total reflection functions slightly differently for x-rays. Due to the values the decrement takes for x-rays, most solid media have a refractive index whose real part is slightly less then 1. This makes them optically thinner than air, and results in total *external* reflection, whereupon an x-ray is totally reflected when attempting to pass a border from air/vacuum into a solid material. This makes it possible to totally reflect an x-ray beam off of most solid surfaces, which forms the basis of total reflection x-ray fluorescence analysis (TXRF).

2.3.3 Standing wave field

Electromagnetic interference refers to the phenomenon of superposition of two or more electromagnetic waves. This superposition results in a simple addition of the electromagnetic waves' electric field components.

$$\vec{E} = \vec{E}_1 + \vec{E}_2$$

From this, the total intensity can be derived

$$I = ||\vec{E}||^2 = \underbrace{||\vec{E}_1||^2}_{I_1} + \underbrace{||\vec{E}_2||^2}_{I_2} + \underbrace{2|\vec{E}_1 \cdot \vec{E}_2|}_{Interference\ term}$$

The interference term is dependant on the phase difference between the two waves, and for two electromagnetic waves of the same frequency with phase shifts of $\phi_1(\vec{r})$ and $\phi_2(\vec{r})$ respectively can be written down as

$$2||\vec{E}_1||||\vec{E}_2|| \cos[\phi_1(\vec{r}) - \phi_2(\vec{r})]$$

If the interfering waves with equal frequencies are travelling in opposite directions, the interference field becomes stationary, and its intensity distribution profile does not change with time. This is a so-called *standing wave field*.

In the case of total external reflection above a thick substrate, the incident and totally reflected x-ray beams interfere above the substrate surface. Due to the very small critical angles for x-rays for most solid surfaces, the incident and reflected beam are often almost parallel in TXRF. Because the glancing angles are very small compared to the width of the beams used, the overlap between the incident and reflected beam cannot be neglected. This results in interference in a triangular area above the substrate, and a standing wave field is formed. The pattern of this field moves from the incident to the reflected beam parallel to the reflecting surface. Perpendicular to the surface, standing waves with *nodes* and *antinodes* are formed. Parallel to the surface, one can observe nodal planes with zero field strength, and between them antinodal planes of maximal amplitudes.

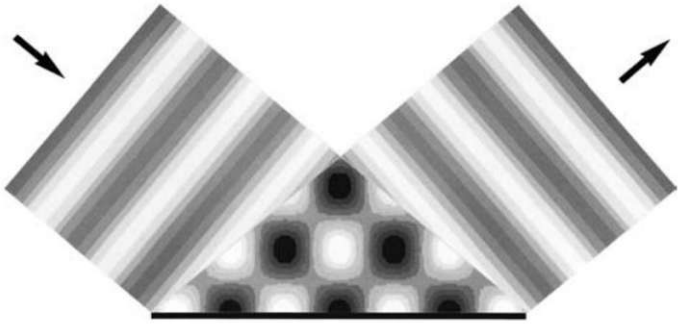

Figure 20: Interference of the incoming and the reflected X-ray waves in the triangular region above a flat and thick reflecting substrate. The strength of the electromagnetic field is represented in a gray scale with instantaneous crests (white) and troughs (dark or black). In the course of time, the pattern moves from the left to the right. Figure and description from Ref. [1, p. 88]

This structure can be seen if one mathematically describes the standing wave field that forms as a result of total external reflection. Assuming a reflective surface in the xy-plane with a reflectivity of $R = 1$, a monochromatic x-ray beam with a wavelength of λ, a glancing angle of α and an electric field strength E_0, an interference field is formed which can be expressed as

$$E_{int} = 2E_0 \underbrace{\sin\left(k_0 z \sin\alpha + \phi\right)}_{Stationary\ nodal\ and\ antinodal\ planes} \cdot \tag{1}$$

$$\underbrace{\cos\left(k_0 ct - k_0 x \cos\alpha\right)}_{Time-dependency\ and\ propagation\ in\ x-direction} \tag{2}$$

It can be seen that if x is fixed, a simple standing wave is obtained, which is indeed the case for directions perpendicular to the reflecting surface. In the case of planes parallel to the reflecting surface, z is constant, and that results in a propagating wave with an amplitude of $2E_0 \sin\left(k_0 z \sin\alpha + \phi\right)$. If one considers the minima and maxima of this amplitude function with respect to z, we get the above mentioned nodal and antinodal planes. The distance between these planes is

$$a_{vertical} = \frac{\lambda}{2\sin\alpha}$$

Following the derivation from *Klockenkämper*, one can arrive at the expression for the standing wave field intensity above an infinitely thick substrate surface.

$$I_{Int}\left(\alpha, z\right) = I_0\left[1 + R\left(\alpha\right) + 2\sqrt{R\left(\alpha\right)}\cos\left(2\pi z / a_{vertical} - \phi\left(\alpha\right)\right)\right]$$

The first term represents the incoming wave, the second term the reflected wave, and the third term is the interference term. It should be noted that the phase shift $\phi\left(\alpha\right)$ only occurs in the region of total reflection, and depends on the glancing angle.

$$\phi(\alpha) = \arccos\left[2\left(\frac{\alpha}{\alpha_{crit}}\right)^2 - 1\right]$$

The nodes and antinodes can respectively be characterized by a minimum or maximum of intensity

$$I_{min,max} = I_0\left[1 + R(\alpha) \mp 2\sqrt{R(\alpha)}\right]$$

The highest contrast is reached for $R = 1$, which is the ideal case for total external reflection. In this case $I_{min} = 0$ and $I_{max} = 4$, which explains the great potential that TXRF has for fluorescence signal boosting, as an increase of up to four times is theoretically possible. Below the surface of the substrate, the intensity drops off exponentially with depth, more specifically

$$I_{Int}(\alpha, z) = I_0\left[1 + R(\alpha) + 2\sqrt{R(\alpha)}\cos\phi\right] exp\left(-\frac{z}{z_n}\right)$$

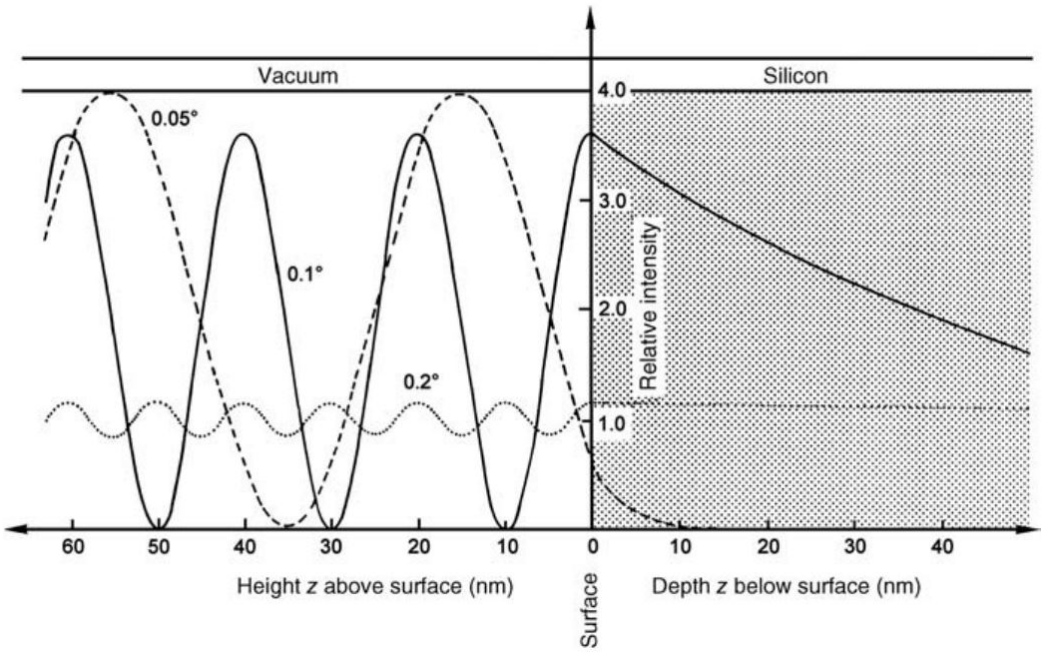

Figure 21: Cross-sections of the standing wave fields called "angle-cuts" at three glancing angles of 0.05°(dashed line), 0.1°(full line), 0.2°(dotted line). The normalized primary intensity is dependent on z (from left to right). Standing wave fields distinctly arise above the surface for glancing angles at and below the critical angle of total reflection, which is 0.1°. Figure and description from Ref. [1, p. 95]

When a thin layer is present on the substrate, additional steps need to be taken to account for the extra medium borders. It must be noted that the beam experiences additional reflection and refraction on the layer-vacuum border, and not just the layer-substrate border.

The principle however, remains the same, with a standing wave field forming above the substrate, with oscillations in intensity dependent on the glancing angle.

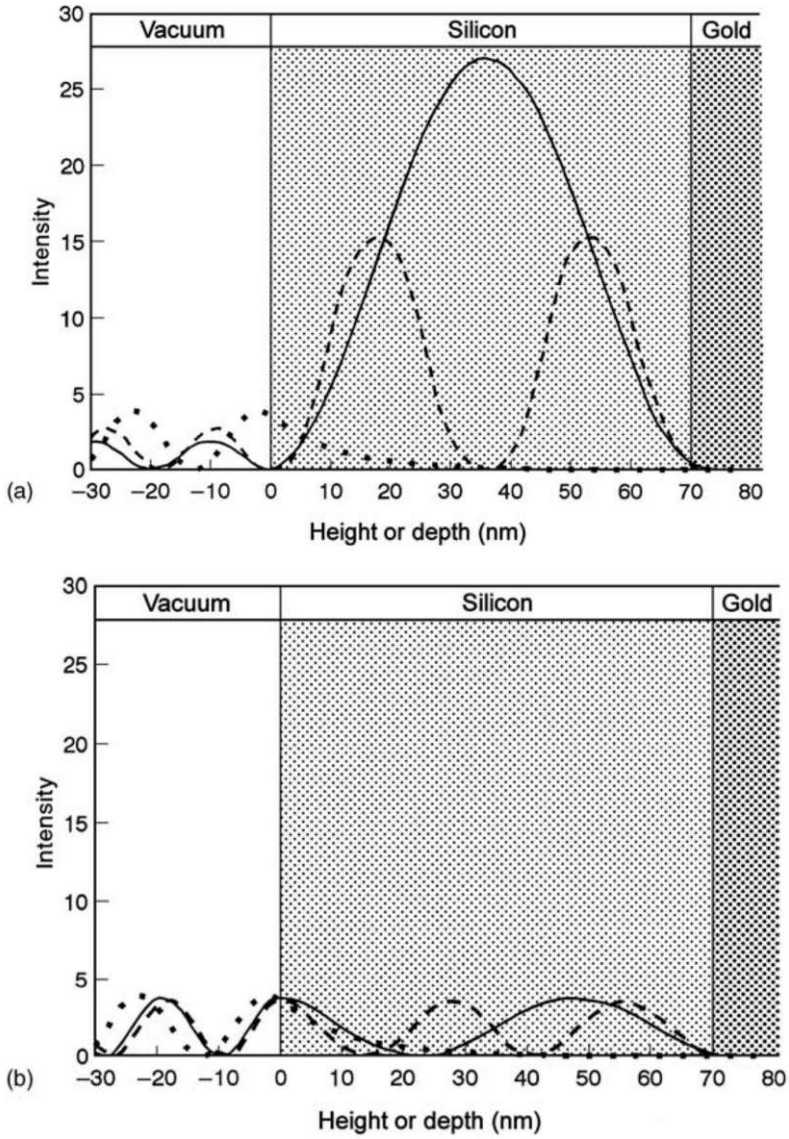

Figure 22: Standing waves in front of and within a thin layer deposited on a thick substrate. namely 70 nm silicon on gold. The normalized intensity is plotted vs. the depth normal to the Si layer at various glancing angles: (a) $\alpha = 0.189°$dotted, $0.203°$solid, $0.235°$dashed. (b) $\alpha = 0.189°$dotted, $0.214°$solid, and $0.253°$dashed. Figure and description from Ref. [1, p. 99]

2.4 X-ray fluorescence analysis

As stated earlier, x-rays can interact with matter via photoelectric absorption, exciting atoms that later decay through electron dipole transitions, or x-ray fluorescence. Using an initial beam of x-rays, one can excite an unknown sample and observe the emitted x-ray fluorescence, which as seen previously is characteristic for every element. Detecting and

quantifying this emitted x-ray fluorescence is the basis of *x-ray fluorescence analysis* (XRF). Depending on which prinicple is used to detect this radiation, XRF can be divided into *energy-dispersive*it XRF (EDXRF) and *wavelength-dispersive* XRF (WDXRF). Most TXRF spectrometers utilize energy-dispersive methods during operation, although a majority of XRF spectrometers in general use WDXRF.

2.4.1 Wavelength-dispersive x-ray fluorescence analysis

WDXRF uses detectors that exploit the *Bragg principle* to detect and quantify x-ray fluorescence of different wavelengths. The Bragg principle determines the angle at which constructive interference occurs for a reflected polychromatic x-ray beam for each wavelength, depending on the material properties of the reflecting surface and the wavelength. For an x-ray wavelength of λ, and a reflecting material with a crystal lattice distance of d, the angle at which constructive interference is achieved can be determined as

$$n\lambda = 2d \sin \alpha_1$$

The factor $n \in \mathbf{Z}$ is the diffraction order.

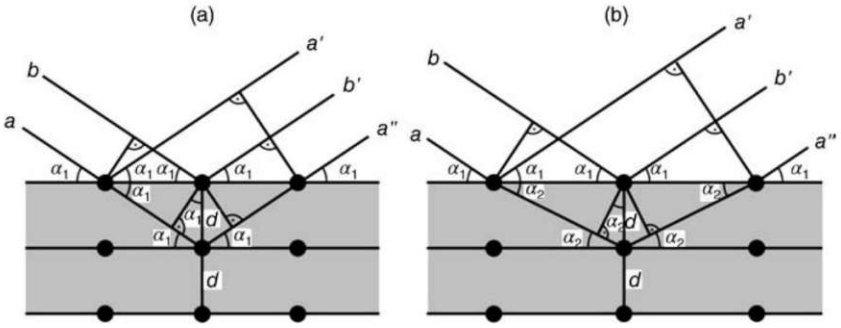

Figure 23: Bragg reflection of two parallel x-ray beams on a crystal surface with a lattice distance of d. Case (a) presents a case without refraction at the crystal surface, while case (b) shows the case with refraction. The path differences between the two beams for both cases come out to $2d \sin \alpha_1$ and $2d \sin \alpha_2$, respectively. For maximum reflectivity, the path difference needs to be equal to an integer multiple of the wavelength of the incoming beam λ_1 in case (a), or λ_2 in case (b). The relation $\lambda_2 \cos \alpha_1 = \lambda_1 \cos \alpha_2$ can be derived from the Snellius' law, and shows that both cases follow the same Bragg's law shown above. Figure from Ref. [1. p. 61]

This phenomenon can be utilized through the usage of a crystal with a known lattice structure, which diffracts the incoming x-ray fluorescence under known angles for each wavelength of a spectrum. Scanning over the range of angles and counting the incoming radiation with a scintillator or a proportional counter yields a spectrum which can be interpreted and

quantified.

WDXRF is a very precise analytical method, as the energy resolution is much better than EDXRF. This is somewhat offset by the duration of each measurement, as for a complete spectrum to be obtained, an angle range must be scanned step by step. This can be somewhat circumvented by installing several crystals and detectors at different angles, already aligned to detect specific fluorescence wavelengths of expected elements.

2.4.2 Energy-dispersive x-ray fluorescence analysis

As the name states, energy-dispersive x-ray analysis differentiates between the different incoming fluorescence photons based on their energy. To accomplish this, energy-dispersive detectors utilize cooled *semiconductor crystals*, wherein interacting x-ray fluorescence photons release electron-hole pairs in an amount proportional to their original energy. Due to a reverse bias electric field applied to the crystal, the electrons and holes drift to opposite sides of the crystal. Upon coming into contact with the electrodes at the ends of the crystal, a charge pulse is produced which is proportional to the energy of the original photon.

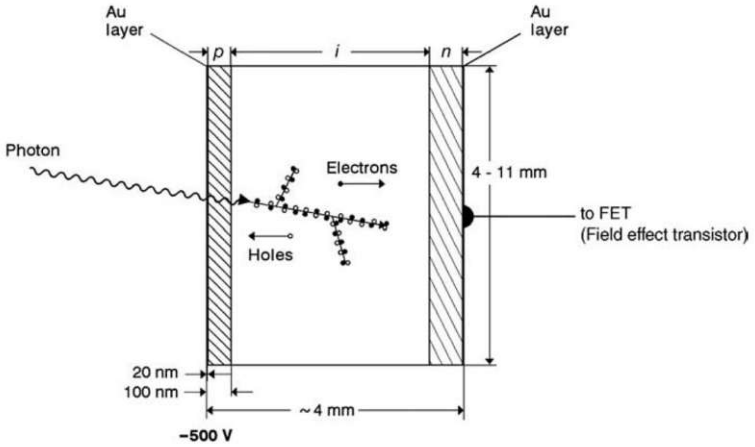

Figure 24: Energy dispersive x-ray detector function. Figure from Ref. [1, p. 166]

The *silicon drift detector* (SDD) is a more advanced type of energy-dispersive detector. While functioning on the same basic principle, it improves on the technology in a couple of major ways:

- Silicon of very high purity is used, leading to much lower leakage currents and the ability to be cooled with Peltier elements instead of liquid nitrogen.
- An architecture of concentric rings is employed for the electrodes, with the collecting anode in the center. This architecture makes the electrons drift transversally to a much smaller anode, guaranteeing a very low input capacitance.

- A junction field effect transistor is integrated into the center of the crystal, again as concentric rings inside the anode. This further lowers capacitance, allowing for shorter shaping times, higher throughput and better energy resolution.

For the purposes of this work, an SDD was used for measuring x-ray fluorescence emitted by the sample.

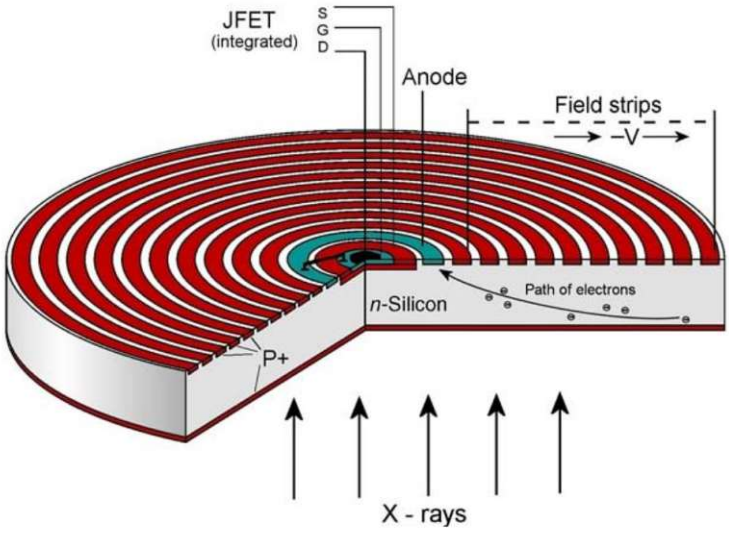

Figure 25: Scheme of a silicond drift detector. Figure from Ref. [1, p. 168]

2.4.3 Energy dispersive detector efficiency

An important aspect of an energy dispersive detector's function is its *efficiency*, defined as the ratio of the number of detected photons to the number of incoming photons. The efficiency of an energy dispersive detector is mainly influenced by two factors: entrance window transmission and the absorption effects inside the detector.

The entrance window is the first barrier that the incoming x-ray photons need to pass through to get to the detector. Most detectors utilize beryllium, due to its low energy absorption edges, making it highly unlikely to absorb high energy x-rays, while blocking out electrons. For light element XRF, beryllium is not suitable, as the low energy fluorescence coming from the light elements can be absorbed by beryllium with a much higher probability, severely dampening the already low fluorescence intensity. To combat this, different materials can be used, like polymers or silicon nitrate.

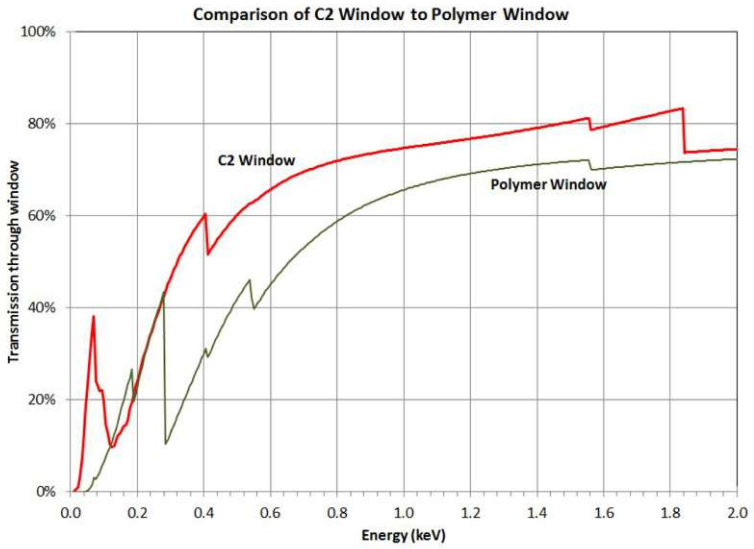

Figure 26: Example entrance window transmission data for different window materials offered by *Amptek*. Both curves exhibit characteristic drops in transmission efficiency correlating to absorption edges of the materials used. The spectrometer used in this work used a detector equipped with a *C2* window, which was specifically designed for light elements, most importantly carbon. Figure from Ref. [2]

Absorption effects that take place inside the detector but outside the active crystal can reduce efficiency, although most are negligible for x-rays between 5 keV and 10 keV (Ref. [1]). This mainly comes down to x-rays interacting with the contact layer and the inactive or dead layer of the semiconductor crystal. The total detector efficiency can be expressed through a formula

$$\varepsilon = exp\left[-\left(\frac{\mu}{\rho}\right)_{Be}\rho_{Be}d_{Be} - \left(\frac{\mu}{\rho}\right)_{Contact}\rho_{Contact}d_{Contact} - \left(\frac{\mu}{\rho}\right)_{Si}\rho_{Si}d_{Si}\right] \cdot \tag{3}$$

$$\left[1 - exp\left[-\left(\frac{\tau}{\rho}\right)_{Si}\rho_{Si}d_{Intrinsic}\right]\right] \tag{4}$$

where $\left(\frac{\mu}{\rho}\right)$ is the total mass absorption coefficient of a layer, ρ its density, and d its thickness. Silicon appears two times in the equation, and that is because both the inactive zone and the intrinsic region need to be taken into account, with their thicknesses d_{Si} and $d_{Intrinsic}$ respectively. While the inactive zone of the silicon crystal contributes to the drop in efficiency with its total mass absorption coefficient, only the photoelectric mass absorption coefficient $\left(\frac{\tau}{\rho}\right)$ is relevant for the intrinsic area.

2.4.4 Input-output yield

The *input-output yield* of an energy dispersive detector is another important characteristic that must be understood in order to fully grasp how such a detector functions under different

conditions.

The *input rate* is defined as the number of pulses the detector crystal produces in a unit of time, while the *output rate* is the number of puleses processed by the multichannel analyzer (MCA). These rates differ from one another due the limitations of the detector electronics, also known as the *dead time effect*.

The pulses collected and passed on by the detector have a certain peaking time, which can be tuned depending on what rate of incoming fluorescence photons is expected. This value ranges from 0.1 to 100 microseconds, with lower values more suitable for higher intensities, and higher values for lower intensities. This peaking time cannot be neglected when pulses are being registered because overlap of two or more pulses is possible. To prevent this, a pulse-pileup rejector ignores pulses which arrive too close to each other. This time period which must pass before another pulse can be accepted is the dead time of the detector, and because of it, the output rate of a detector is always lower than the input rate, as certain pulses are getting rejected during the dead time. As the input rate increases, so does the output rate, but the ratio between the two rises as the higher input rate triggers the pileup rejector more and more often.

The input-output ratio of a detector can be defined with an exponential expression

$$n_{out} = n_{in} exp\left(-\tau_{dead} \cdot n_{in}\right)$$

The dead time τ_{dead} is defined as the sum of the pulse peaking time, falling time and the analog-to-digital-converter (ADC) conversion time. For most cases, it is between three and five times the pulse peaking time.

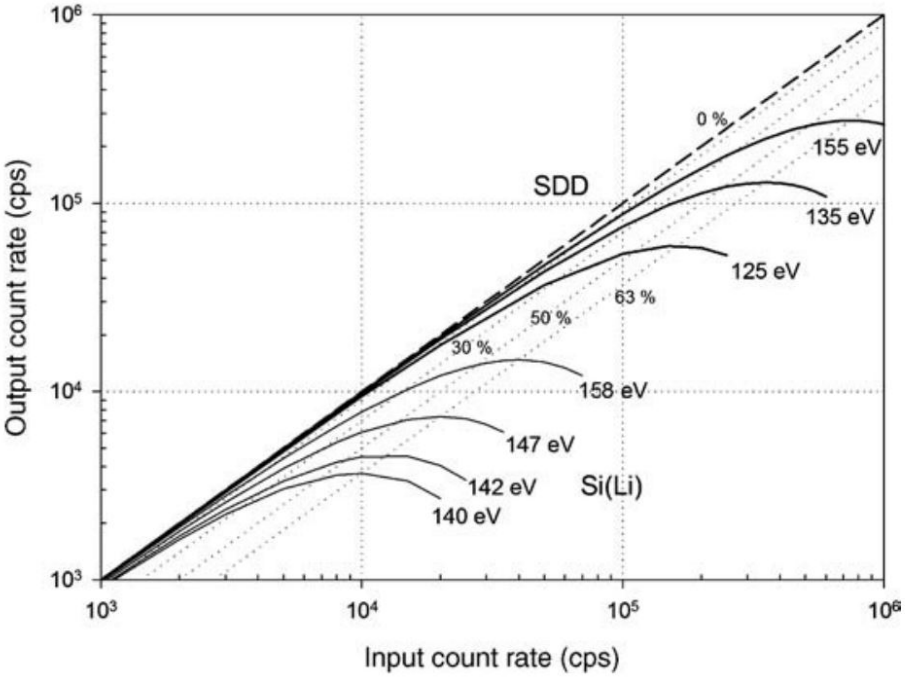

Figure 27: Input-output ratio dependent on the input rate of an SDD with a 25 mm^2 active surface area. Each curve corresponds to a certain spectral resolution, or a certain peaking time. Constant dead time losses are indicated by the dashed lines with their values expressed as percentages. It can be seen that each curve reaches its maximum (the choking point) at a dead time loss of 63.2%. Figure from Ref. [1, p. 196]

The figure above shows examples of input-output curves for different values of energy resolution (which inversely depends on the peaking time). As can be seen, the output rate rises linearly with the input rate up to a certain point, until the dead time losses increase and the curve reaches a peak, after which the output rate decreases even as the input rate increases. Calculating the output rate cannot be done unambiguously past this choking point.

In order to correct for dead time losses in practice, measurements are often prolonged to compensate. This "acquiring" time T is calculated from the "live" time t, which is how long the detector is supposed to be measuring pulses, and the dead time loss expressed as a percentage D of the total time.

$$D = 1 - exp\left(-\tau_{dead} n_{in}\right)$$

$$T = \frac{100}{100 - D} \cdot t$$

2.4.5 Spectrum artifacts

An important characteristic of energy dispersive spectra are the artifacts that can appear during measurements, usually expressed as peaks corresponding to nonexistent events. These artifacts can be divided into *escape peaks* and *sum peaks*.

Escape peaks usually appear as a consequence of a very strong fluorescence peak of a particular element. Normally, an incident x-ray photon interacts with the semiconductor crystal through scattering and the photoelectric effect. An ejected photoelectron leaves behind an excited atom, which can then decay through x-ray fluorescence, usually a $K\alpha$ or $K\beta$ emission. Most of the time, this emitted fluorescence will interact further with the crystal and be properly registered by the detector, adding to the total energy of the original incoming photon. If the rate of these incoming photons is high enough however, some of these fluorescence x-rays emitted by the semiconductor atoms can escape the crystal, carrying with them the distinct $K\alpha$ or $K\beta$ energy of the semiconductor atom. This produces a smaller low energy peak with an energy exactly equal to the original, minus the escaped $K\alpha$ or $K\beta$ energy. This peak is called an escape peak, and can appear when an element is strongly present in a given sample. These escape peaks can pose problems during quantification if they overlap with other real peaks in the low energy region of the spectrum.

A sum peak is a consequence of the input rate being higher than ideal for the preset peaking time of the detector. In this case, some pulses may exactly overlap, creating a pulse with the energy equal to the sum of the original pulses. This in turn creates a high energy peak, which can overlap with other real fluorescence peaks in high energy regions of the spectrum.

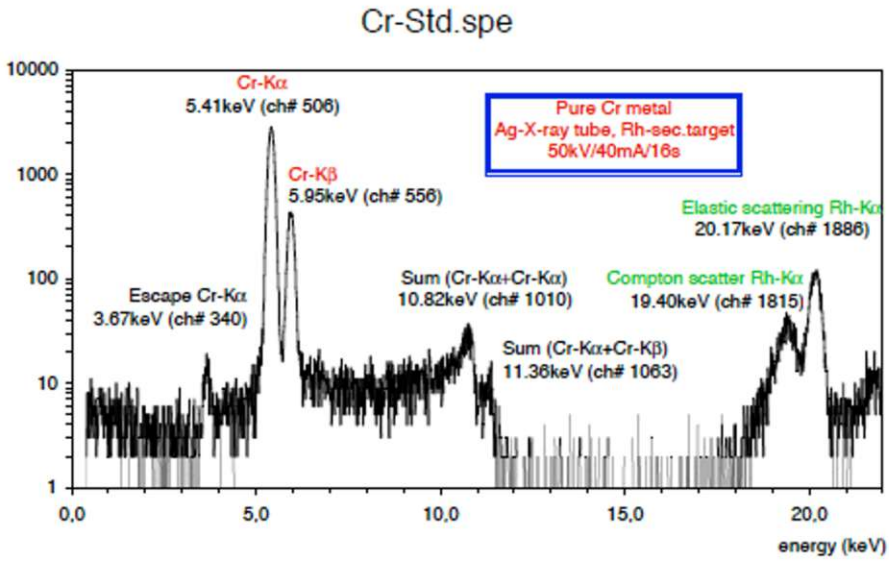

Figure 28: An example spectrum showing a chromium sample measured with an x-ray tube utilizing a silver anode and a rhodium secondary target. The spectrum clearly shows the Cr-Kα escape peak, as well as the Cr-Kα and Cr-Kβ sum peaks. Figure provided by Prof. P. Kregsamer.

It is important to take note of these artifacts and properly identify them in an energy dispersive spectrum during quantification. To properly quantify energy dispersive spectra, dedicated x-ray analysis software can be used to deconvolute overlapping peaks.

2.4.6 Fluorescence intensity calculation

Considering the theoretical model and all the factors that influence it, one can mathematically describe the correlation between the concentration of a certain element in a sample and the observed intensity of its emitted fluorescence radiation. For this to be calculated, one has to know the spectral distribution $I_0(E)$ of the primary exciting beam, the photoelectric absorption coefficient of the different elements of the sample $\frac{\tau_K^i(E)}{\rho}$, fluorescence yield ω_K^i and emission probability p_α^i (defines the probability of α, β, etc. lines being emitted), attenuation between the sample and the detector, higher order effects in the sample matrix, detector efficiency $\varepsilon\left(E_{K_\alpha}^i\right)$, all the relevant geometrical factors, the sample density distribution and the concentrations of the present elements.

$$I\left(E^i_{K_\alpha}\right) = \int_{E=E^i_{abs}}^{E_{max}} \int_{x=0}^{x=d} \underbrace{\frac{dI_0(E)}{dE}}_{\text{Exciting beam intensity}} \cdot \underbrace{\frac{F\sin\phi}{4\pi r^2}}_{\text{Geometry factor } G_1} \cdot \underbrace{\frac{I_{int}(\phi,x,E)}{I_0}}_{\text{Standing wave}} \cdot \frac{\rho(x)}{\sin\phi} \cdot \tag{5}$$

$$\underbrace{\frac{\tau^i_K(E)}{\rho} \cdot \omega^i_K \cdot p^i_\alpha}_{\text{Fluorescence cross section}} \cdot \underbrace{c^i(x)}_{\text{Element concentration}} \cdot \underbrace{V^i(E)}_{\text{Secondary excitation}} \cdot \tag{6}$$

$$\underbrace{e^{-\left(\frac{\mu(E)}{\rho\sin\phi}\right)\rho x}}_{\text{Exciting beam attenuation}} \cdot \underbrace{e^{-\left(\frac{\mu\left(E^i_{K_\alpha}\right)}{\rho\sin\psi}\right)\rho x}}_{\text{Fluorescence in-sample attenuation}} \cdot G_2(\psi) \cdot \tag{7}$$

$$\underbrace{f\left(E^i_{K_\alpha}\right)}_{\text{Sample-detector attenuation}} \cdot \underbrace{\varepsilon\left(E^i_{K_\alpha}\right)}_{\text{Detector efficiency}} \; dxdE \tag{8}$$

While this expression was not used in this work to theoretically calculate expected intensities from measured samples, it should be kept in mind when interpreting the results. This is especially important for the analysis of light elements, as improvements in any one of the factors named above can be critical in improving the detected intensities, and therefore the counting statistics and reliability of results.

2.4.7 Thin film approximation

If the formula for the detected fluorescence line intensity is considered with a homogeneous and adequately thin sample in mind, almost all sample-specific factors can be simplified down to the sample mass, and all instrument-specific factors can be represented by a sensitivity factor for that fluorescence line. This is the basis of the thin film approximation.

Going through the formula, one can immediately eliminate the sample matrix element, as with a thin sample, its influence is negligible. The geometry factor G_1, elemental concentration c_i, and $\rho/\sin\phi$ can be reduced to the sample mass $dm_i(x)/dx$ multiplied by a constant factor $1/4\pi r^2$.

With this, the integral over x can be calculated, leaving only a factor for the average standing wave intensity $I_{int}(\alpha,E)/I_0(E)$ multiplied by the total mass m_i of element i. What is left is the energy integral, and this is the thin film approximation.

$$I\left(E_{K^i_\alpha}\right) = m^i \cdot \int_{E=E^i_{abs}}^{E_{max}} \underbrace{\frac{\frac{dI_0(E)}{dE}}{4\pi r^2}}_{\text{Exciting beam intensity}} \cdot \underbrace{\frac{I_{int}(\phi,E)}{I_0(E)}}_{\text{Standing wave}} \cdot \underbrace{\frac{\tau^i_K(E)}{\rho} \cdot \omega^i_K \cdot p^i_\alpha}_{\text{Fluorescence cross section}} \cdot \tag{9}$$

$$G_2(\psi) \cdot \underbrace{f\left(E^i_{K_\alpha}\right)}_{\text{Sample-detector attenuation}} \cdot \underbrace{\varepsilon\left(E^i_{K_\alpha}\right)}_{\text{Detector efficiency}} \cdot dE \tag{10}$$

This expression can be further simplified in the case of a monochromatic exciting beam.

$$I\left(E^i_{K_\alpha}\right) = m_i \cdot \frac{I_0(E)}{4\pi r^2} \cdot \frac{I_{int}(\phi, E)}{I_0(E)} \cdot \frac{\tau^i_K(E)}{\rho} \cdot \omega^i_K \cdot p^i_\alpha \cdot G_2(\psi) \cdot f\left(E^i_{K_\alpha}\right) \cdot \varepsilon\left(E^i_{K_\alpha}\right)$$

2.4.8 Total reflection x-ray fluorescence analysis (TXRF)

TXRF attempts to utilize total external reflection and the subsequently formed standing wave field to amplify the intensity of the exciting x-rays, thus boosting excitation and subsequent x-ray fluorescence emission. To accommodate this, TXRF samples are usually placed on highly reflective wafers, or substrates, usually made of quartz, silicon or plexiglass.

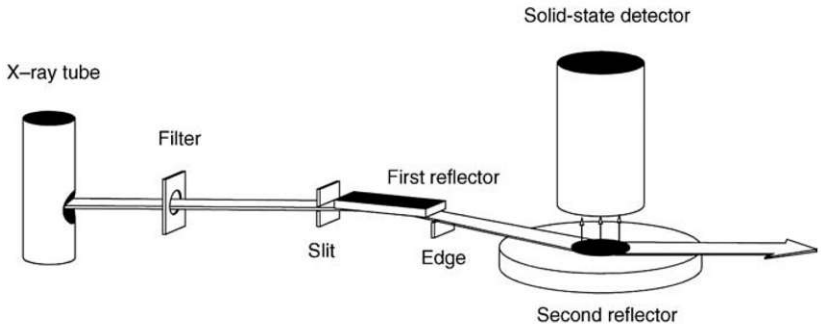

Figure 29: Basic TXRF setup. The first reflector usually acts as a monochromator, while the second reflector is the substrate surface. Figure from Ref. [1, p. 129]

Due to total external reflection, the beam penetration inside the sample bulk is drastically reduced, and therefore the excitation of the substrate is minimized, reducing its fluorescence peak. With the beam totally reflected, the incoming and the reflected beam form a standing wave field that can increase sample excitation up to four times. Furthermore, total reflection critical angles are extremely small, making the beam almost parallel to the substrate surface, and therefore leaving enough room to position the detector window as close as possible and maximize the number of detected photons. Finally, due to samples usually being very thin layers on polished substrate surfaces, thin film approximation can be applied during quantification, making calculating theoretical factors and unknown concentrations much more straightforward.

If the incident angle of the exciting X-Ray beam is varied, a change in the intensity of fluorescence signals can be noticed due to the change in X-Ray penetration of the sample. Due to this effect, different spatial distributions of a material show characteristic signals over an angle range, allowing them to be identified.

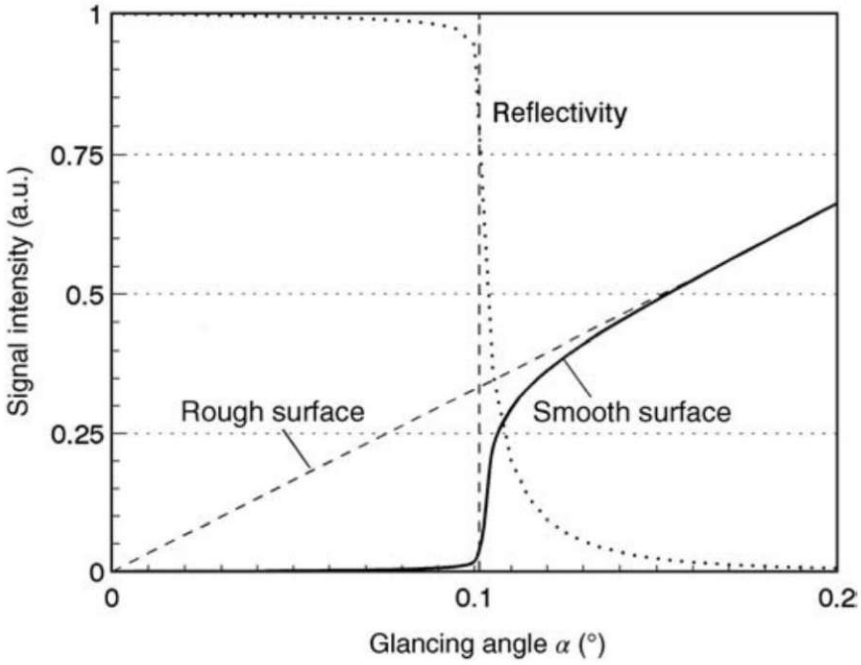

Figure 30: Signal intensity of a thick, flat, and smooth silicon substrate (full line), calculated for an incident Mo-Kα beam. In addition, the reflectivity R is shown with the dotted line, dependent on the glancing angle α. Below $\alpha_{crit} = 0.109°$, total reflection occurs with a steplike increase in reflectivity and a steplike decrease of the signal intensity. The dashed line represents the intensity from a rough Si substrate. Figure and description from Ref. [1, p. 103]

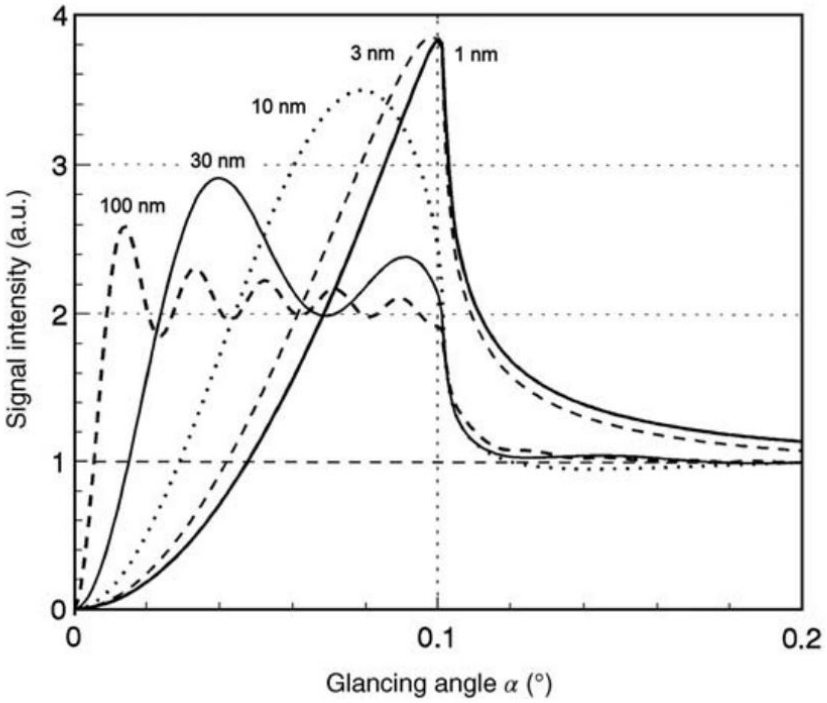

Figure 31: Fluorescence signal of small particles or thin films deposited on a silicon substrate used as a sample carrier. The intensity was calculated for particles, thin films or sections of different thickness but equal mass of the analyte, and plotted against the glancing angle α. A Mo-Kα beam was assumed for excitation. Particles or films more than 100 nm thick show double intensity below the critical angle of 0.1°. Figure and description from Ref. [1. p. 105]

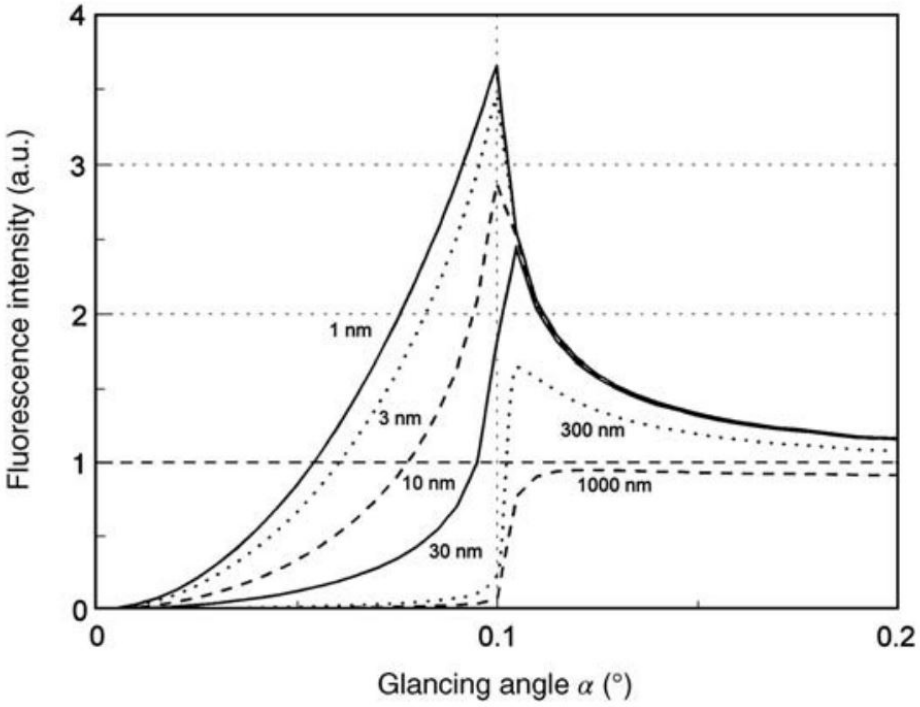

Figure 32: Fluorescence intensity from layers buried in a thick substrate. The intensity dependent on the glancing angle was calculated for layers of different thickness but with a constant area density of the analyte. Silicon was assumed as the substrate, Mo-Kα x-rays as the primary beam. Total reflection occurs in the region below 0.1°. Figure and description from Ref. [1, p. 107]

2.4.9 Sensitivity and calibration

To properly calibrate and characterize an instrument, a series of measurements of known samples must be conducted. Plotting the fluorescence intensities against the known masses of the observed elements nets each element a curve whose incline equals the *sensitivity* of the specific setup to that element. With this data, one can then quantify unknown samples, so long as the experimental setup is not varied.

Alternatively, an *internal standard* can be used. An internal standard is an element that is usually not present in the measured multielement samples, and can easily be detected and quantified. For this to be true, its fluorescence peaks should have minimal or no overlap with peaks of elements already present in the sample. If a known quantity of an internal standard is mixed with samples of known compositions, relative sensitivities of the elements present in those samples in relation to the internal standard can be calculated, thanks to the simplicity of the thin film approximation in the case of TXRF. The relative sensitivities can then be used to quantify samples with unknown compositions after adding a known amount of the same internal standard and measuring the samples under the same conditions.

$$
\begin{aligned}
S_{rel_{i/j}} &= \frac{S^i_{K_\alpha}}{S^j_{K_\alpha}} \\
&= \frac{I\left(E^i_{K_\alpha}\right)/m^i}{I\left(E^j_{K_\alpha}\right)/m^j} \\
&= \frac{\cancel{\frac{I_0(E)}{4\pi r^2}} \cdot \cancel{\frac{I_{int}(\phi,E)}{I_0(E)}} \frac{\tau^i_K(E)}{\rho} \cdot \omega^i_K \cdot p^i_K \cdot \cancel{G_2(\psi)} \cdot f\left(E^i_{K_\alpha}\right) \cdot \varepsilon\left(E^i_{K_\alpha}\right)}{\cancel{\frac{I_0(E)}{4\pi r^2}} \cdot \cancel{\frac{I_{int}(\phi,E)}{I_0(E)}} \frac{\tau^j_K(E)}{\rho} \cdot \omega^j_K \cdot p^j_K \cdot \cancel{G_2(\psi)} \cdot f\left(E^j_{K_\alpha}\right) \cdot \varepsilon\left(E^j_{K_\alpha}\right)} \\
&= \frac{\frac{\tau^i_K(E)}{\rho} \cdot \omega^i_K \cdot p^i_K \cdot f\left(E^i_{K_\alpha}\right) \cdot \varepsilon\left(E^i_{K_\alpha}\right)}{\frac{\tau^j_K(E)}{\rho} \cdot \omega^j_K \cdot p^j_K \cdot f\left(E^j_{K_\alpha}\right) \cdot \varepsilon\left(E^j_{K_\alpha}\right)}
\end{aligned}
\tag{11}
$$

$$
\begin{aligned}
S_{rel_{i/j}} &= \frac{I\left(E^i_{K_\alpha}\right) \cdot m^j}{I\left(E^j_{K_\alpha}\right) \cdot m^i} \\
&= \frac{I\left(E^i_{K_\alpha}\right) \cdot c^j}{I\left(E^j_{K_\alpha}\right) \cdot c^i}
\end{aligned}
\tag{12}
$$

$$
c^i = \frac{I\left(E^i_{K_\alpha}\right)}{I\left(E^j_{K_\alpha}\right)} c^j \cdot \left(S_{rel_{i/j}}\right)^{-1} \tag{13}
$$

As can be seen from the equations above, the relative sensitivity of an element i with regard to the internal standard j in case the thin film approximation stands depends only on the fundamental fluorescence cross section of the each element, as well as the detector efficiency and window transmission for each element. Since all the setup-specific factors like the standing wave intensity, exciting x-ray spectral distribution and geometric factors are kept constant, the relative sensitivity does not change between measurements, allowing for reliable quantification.

2.4.10 Limit of detection

Limit of detection denotes the minimal mass (concentration) an element can have and still have its peak be statistically significant. For this to be possible, the peak must at least be as high as three times the standard deviation of the background signal.

Limit of detection is usually calculated for a measurement time of 1000 seconds. If no such data is available, measured counts per second can simply be multiplied with 1000 seconds to obtain the necessary estimation. An expression for calculating the limit of detection can be found in Ref. [1].

$$
LLD^i_{1000} = \frac{3\sqrt{I_{Bg}}}{I\left(E^i_{K_\alpha}\right)} \cdot m_i
$$

The limit of detection is another measure of an instrument's sensitivity to a certain element, and generally lower values are desired. To improve the limit of detection, two courses of action are possible: increasing the fluorescence intensity, and decreasing the background signal. Both options can prove difficult when working with light elements.

2.5 Light element analysis

To properly analyze the lightest elements, one must overcome a series of fundamental and technical problems that severely hamper excitation, detection and subsequent quantification of samples containing these elements.

X-Ray tubes use metallic anode materials, and are therefore usually monochromatized around a characteristic peak of around several keV. In contrast to this, light elements have absorption edges at several hundred eV, which is significantly lower than the excitation energy, resulting in very poor excitation. This can be seen in the expression for the photoelectric mass absorption coefficient

$$\left(\frac{\tau}{\rho}\right)_j = k_j \frac{Z^3}{E^{8/3}} \tag{14}$$

Since Z is low for light elements, the photoelectric mass absorption coefficient is already decreased, and this is further emphasized by the energy of the exciting x-rays, which the photoelectric mass absorption coefficient is inversely related to. To combat this, chromium x-ray tubes are used, as its one of the lightest metals which can be used as an x-ray anode. Even so, the cubic drop off of the photoelectric mass absorption coefficient with Z severely hampers excitation of carbon.

Besides the low photoelectric mass absorption coefficient of light elements for x-rays, light elements also have a very low fluorescence yield (see Figure 7), meaning that for light elements, the Auger effect has a far greater probability of occurring rather than x-ray fluorescence. For reference, carbon (Z=6) has a fluorescence yield of $2.56 \cdot 10^{-3}$, compared to the fluorescence yield of titanium (Z=22) which equals 0.226. This is an inherent characteristic of light elements, and the only possibility of reducing its influence is in increasing the photoelectric mass absorption coefficient with lower energy excitation, and increasing the overall intensity of the exciting x-ray beam.

Another thing to consider is attenuation, which can occur at various points in the measurement setup. Inside the sample, primary and secondary attenuation can weaken the signal. Primary attenuation, which is attenuation of an element's fluorescence signal in that same element, is very weak for carbon. Secondary attenuation however, poses a much greater issue, as heavier elements present in the sample (contaminants or otherwise) can further reduce the fluorescence intensity through scattering or photoelectric absorption. Attenuation between

the sample and the detector is an issue when conducting measurements at atmospheric pressure, which is why analysis of light elements takes place in vacuum chambers.

Additionally, emitted light element fluorescence experiences significant attenuation when passing through regular beryllium detector windows, and special ultra-thin windows (several hundred nanometers thick) are required for statistically significant intensities to be measurable in reasonable time intervals. These ultrathin windows do not filter electrons however, so additional steps need to be taken to ensure they do not contribute to the background signal. In the case of this specific TXRF spectrometer, the copper collimator fitted over the entrance window also holds two permanent magnets in place. These magnets bend the trajectories of electrons so they do not reach the detector crystal.

3 Experimental Setup

For the purposes of this work, a low Z spectrometer built in-house was used. The following chapter details the geometry and function of said spectrometer, as well as technical specifications of relevant equipment.

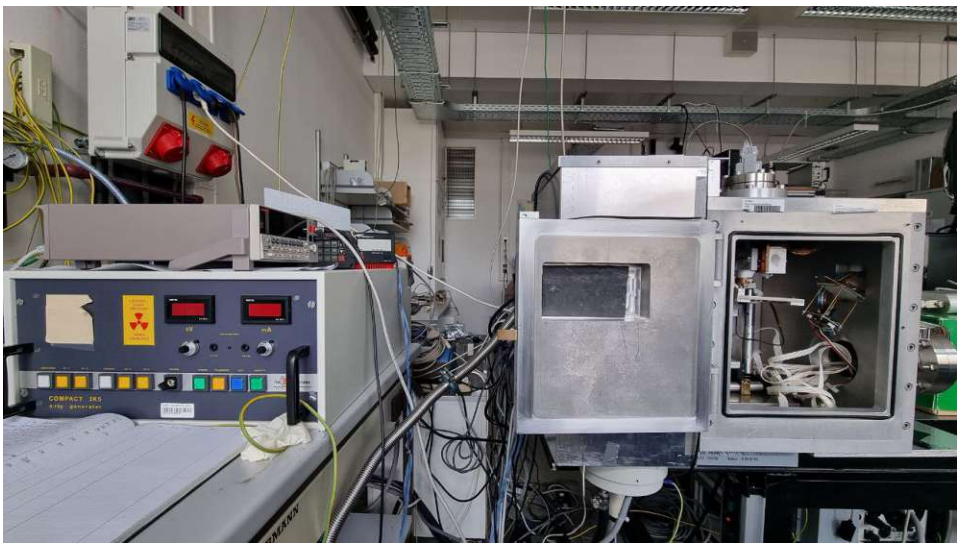

Figure 33: Photo of the complete spectrometer used for this work. From left to right, the setup is composed of the x-ray generator, the x-ray tube inside the shielding (behind the open chamber door) and the vacuum chamber.

3.1 Geometry and concept

The spectrometer consists of three major components: the *x-ray generator*, the shielded *x-ray tube*, and the *vacuum chamber* right beside it. The aluminum vacuum chamber houses most of the setup's moving parts, and is essential for light element detection, as the air would otherwise absorb a lot of the incoming low energy fluorescence.

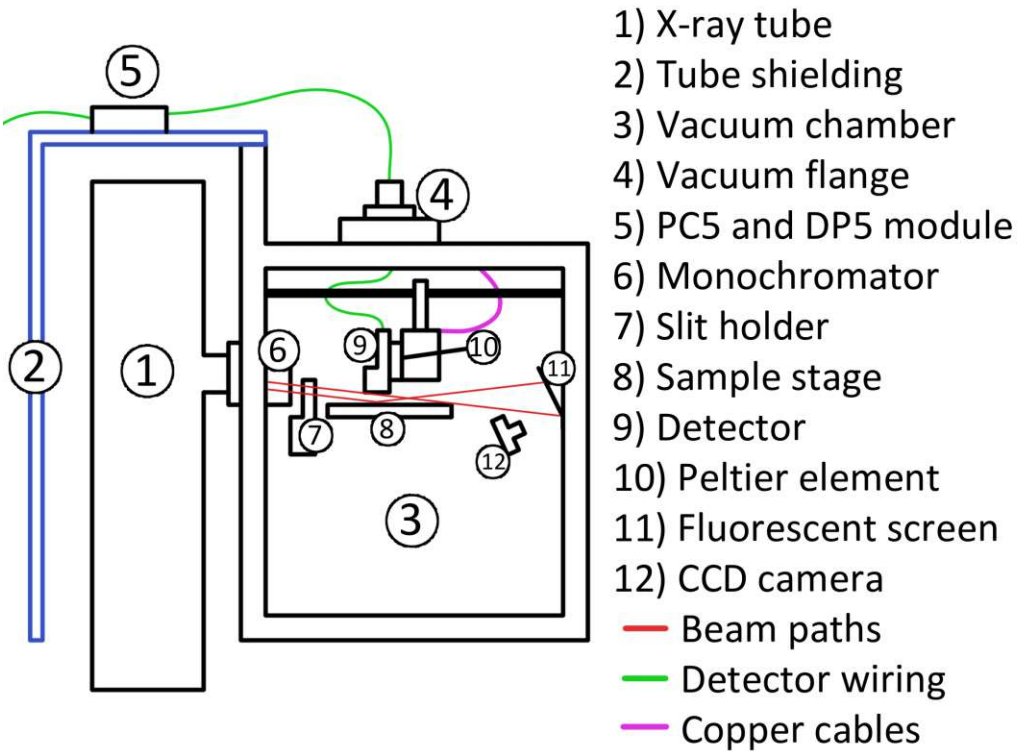

Figure 34: Sketch of the spectrometer. The proportions are not exact, and the x-ray beam angles are exaggerated for visual representation.

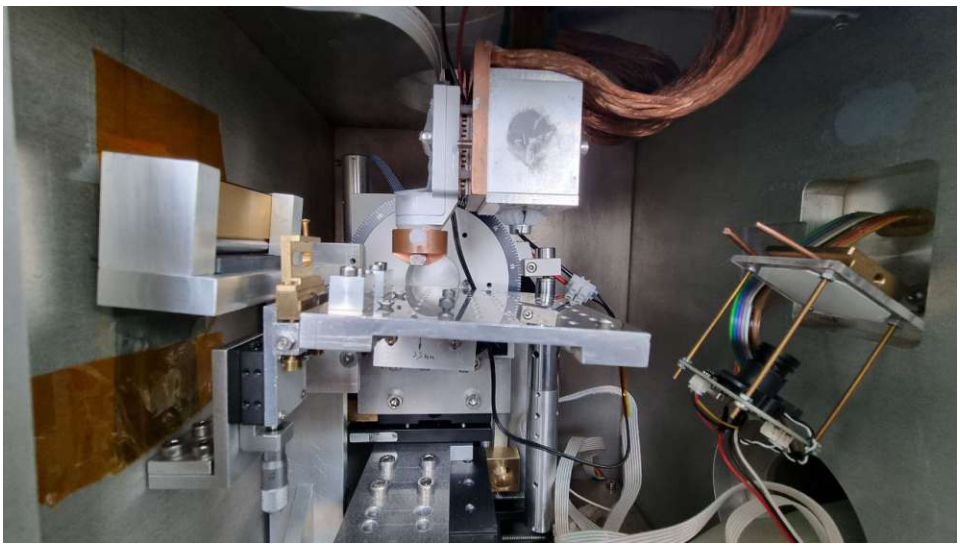

Figure 35: Photo of the inside of the vacuum chamber.

The general geometry and concept of the setup is shown above. The beam enters the vacuum chamber through a 50 μm thick Kapton window, and is reflected off a *monochroma-*

tor, designed to let through CrK_α radiation and suppress the rest of the incoming spectrum. Passing through a slit holder (which can hold a vertical slit) and another horizontal slit, the beam hits the sample standing on an aluminum sample stage located directly beneath the *detector window*, separated with 1-2 mm distance.

With this setup, monochromatisation and small glancing angles needed for TXRF are achieved, also allowing for the sample to be brought very close to the detector, reducing traveling distance, and thus increasing the solid angle the detector sees, and with it the detected fluorescence intensity. In addition to this, a camera has been added opposite of the beam entrance, and can be used to observe the exciting and reflected beam, which can be helpful during initial alignment of the spectrometer.

The sample stage can be moved vertically, and its incline can be controlled, allowing for the sample position on the substrate to be easily found, and the critical angle determined, all in a matter of minutes. Because of this, measuring circumstances can easily be replicated, down to the position of the sample and glancing angle of the incident X-Ray beam.

If necessary, a slit can be inserted into the slit holder in front of the sample stage, though this has not been used in the scope of this work.

Finally, the detector is pointing down towards the sample from directly above, attached to a secured piece of aluminum via a copper plate and a *Peltier* cooling element. It is fitted with a copper *collimator* holding two permanent magnets, which functions as an electron trap. The detector can be moved along a metal beam, but remains firmly secured by a screw during measurements. The cable from the preamplifier to the electronics unit glued to the outside of the spectrometer leads through an air-tight flange.

The spectrometer is operated using a custom-made piece of software installed on a nearby PC unit. While the scanning of samples over a range of coordinates (vertical or angular) is possible, everything can easily be adapted to various sizes and thicknesses of samples. Because of this robust approach, one can use the spectrometer to measure quartz reflectors, plexiglass reflectors, as well as silicon wafer pieces.

3.2 Components

3.2.1 X-ray generator and tube

The X-Ray generator is an *Italstructures* Compact 3K5, usually operated at 30kV and 30 mA. It powers a Panalytical long fine focus tube with a chromium anode. It has a maximum power of 1.9kW, and a maximum voltage of 60kV. The type identifier is PW2278/20. The

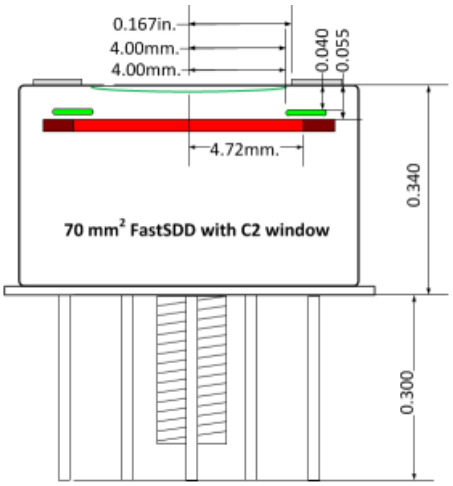

Figure 36: Schematic of the Amptek SDD TO-8 package. Figure from Ref. [2]

tube has a beryllium window with a thickness of 300 micrometers.

The X-Ray tube is mounted directly to the optical table upon which the spectrometer itself is bolted. It is shielded with an aluminum casing which is in direct contact with the vacuum chamber. After the initial alignment of the tube with the entrance slit of the vacuum chamber, and achievement of monochromatisation, the tube is left stationary and not tampered with.

3.2.2 Monochromator

The monochromator used is a repurposed monochromator from an older ATOMIC TXRF system. Due to a lack of official specifications, it was scanned in another spectrometer to determine its Bragg angle for chromium radiation. It was found that the first order Bragg angle for CrK_α was at 1.412 degrees. This information was then used to properly install it in the TXRF spectrometer, and align the instrument.

3.2.3 Detector and cooling system

The detector used was an *Amptek* Fast SDD with a CMOS preamplifier. The OEM configuration includes an AXR detector, featuring a sealed TO-8 package, a heatsink and a PA-230 preamplifier, which then connects via a flexible cable to an outside module that includes the DP5 digital pulse processor, as well as the PC5 power supply.

The detector crystal has an area of 70 mm^2, collimated to 50 mm^2 via an internal multilayer collimator, and a thickness of 500 μm. It uses a "C-Series" C2 ultrathin Si_2N_3 window with an aluminum coating, with a 43.9 percent transmission for carbon K line fluorescence.

The energy resolution at 5.9 kV is between 122 and 129 eV FWHM at a peaking time of 4μs. Most of the time, the detector was operated with a peaking time of 2.4 μs, which was

found to have little influence on the obtained results.

For the detector to operate optimally, it was kept at 220 K (-53 °C). To prevent the heatsink of the preamplifier housing from overheating, additional cooling in the form of copper plating with an Adaptive ET-063-10-13 Peltier element had been installed. To prevent and condensation, an STC-1000 temperature switch was installed, with the intent of cutting power to the Peltier element whenever the detector dropped below a certain temperature. Both the Peltier element and the temperature switch are powered by a Rigol DP832 Programmable DC Power Supply, and keep the preamplifier housing between 19 and 25 °C.

Finally, an electron trap consisting of a copper collimator holding two permanent iron magnets was installed directly onto the TO-8 package, serving as an electron trap for Auger electrons, reducing unwanted noise. This electron trap was reused from a Ketek detector system used previously for this specific spectrometer, as their TO-8 package dimensions were a perfect match. The electron trap has a 5mm diameter opening, allowing for the detector to have an inspected area of 38.48 mm^2.

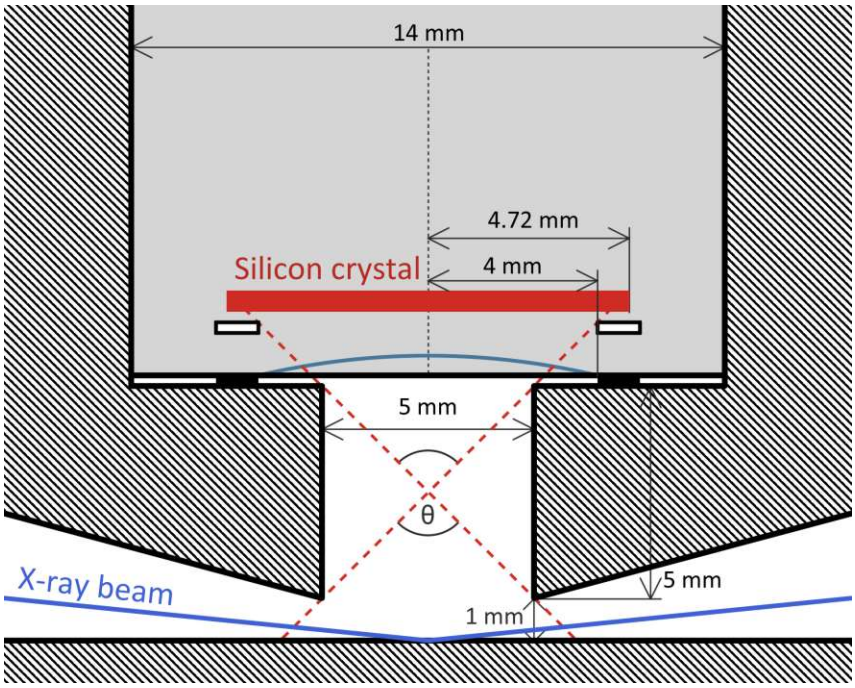

Figure 37: Schematic of the copper collimator opening, as well as the detector's cone of inspection. All relevant dimensions are shown with proper scale with respect to one another. In this case, θ=90°, which yields an inspected area of 38.48 mm^2 at a distance of 1 mm from the end of the collimator.

3.2.4 Miscellaneous

For the purpose of beam and sample alignment, a simple CCD camera was installed inside the vacuum chamber, pointing towards a sheet of fluorescent material that shows the position of the exciting and reflected X-ray beams. The camera provides a video feed directly to the PC unit used to operate the spectrometer, thus allowing for easy insight into the alignment process.

The vacuum chamber needed to be evacuated repeatedly for the different measurements, and to this end, a Hanning electric pump was used. The pressure inside the chamber was kept at around 0.6-0.7 mbar.

3.2.5 Software

The software used as part of this work are the Quantitative X-ray Analysis System (QXAS) developed by IAEA, and JGIXA developed by D. Ingerle. QXAS is a software package that includes the AXIL fitting package (Analysis of X-ray Spectra by Iterative Least-square fitting) and has built-in capabilities and tools for quantitative analysis of unknown samples. JGIXA was developed by D. Ingerle in Java specifically for the purpose of fitting GIXRF angle scans to calculate the thickness, density and roughness of the measured layer (Ref. [27]).

4 Methodology

4.1 Sample preparation

4.1.1 Calibration samples

Carbon calibration samples are prepared on clean, 3 mm thick quartz wafers with a diameter of 30 mm. All wafers are cleaned with Decon 90 and triple distilled water, dried with acetone, and then measured in the TXRF spectrometer before the pipetting process. Upon confirmation of low amounts of contamination, especially when it comes to carbon, the wafers are weighed, and proper amounts of desired solutions pipetted onto their centers. The wafers are then weighed once more to confirm the total mass of solution that was pipetted, before being placed on a heated stove in a ventilated area to dry. Normally, clean wafers are also siliconized before the pipetting process to make their surface hydrophobic and limit the sample solution spreading over a wide area. In the case of samples containing carbon, however, siliconization is avoided due to possible presence of nanoplastics in the solution used in the process.

To prepare analytes with desired masses for calibration, two solutions of trisaminomethane (tris) that contained 10 and 100 ppm of carbon were used. For the samples with desired total carbon mass up to 100 ng, the 10 ppm solution was used, while samples with carbon mass above 100 ng were prepared using the 100 ppm solution. The volume pippeted onto the clean wafers was adjusted with regard to the desired total mass and the concentration of the solution used. A full list of samples follows in Table 1.

Reflector number	Deposited volume of tris solution in μL	C concentration in parts per million	Total mass of carbon in ng
8	N/A	N/A	0
177			22.9
165	3.8	9.97	37.99
29	4.0	9.97	39.89
259	6.0	9.97	59.82
275	7.8	9.97	77.77
6	0.9	100	90
10	1.0	100	100
31	1.5	100	150
38	1.6	100	160
230	1.9	100	190
293	2.1	100	210
139	2.2	100	220
180	2.2	100	220
140			250

Table 1: List of tris calibration samples.

The total masses of carbon on the calibration samples were chosen in such a way as to cover a range of 25 to 250 ng in 20 ng increments. Due to the nature of the manual pipetting process and the step size of the pipettes used, however, the true masses of samples deviated from the intended ones, especially for the samples that used very small deposition volumes and high carbon concentrations. A simple deviation of 0.1 μL when using a solution with a carbon concentration of 100 ppm results in a mass deviation of 10 ng, which is significant if a 20 ng gap is desired between each calibration sample mass. This combination of small deposition volume and high concentration was still necessary, as the clean reflectors could not be siliconized, making it possible for larger deposition volumes to spread outside of the detector's inspected area, making measurements less reliable.

4.1.2 Spin coated samples

All of the spin coated polystyrene samples were prepared by Univeristy of Utrecht, and then delivered by mail for measuring and analysis at the Atominstitut in Vienna. This work focused on two series of such samples: older spin coated samples that were prepared on silicon wafers in 2020, and newer samples that were prepared on quartz wafers in 2022. The spin coating process by definition allows some of the analyte to drip off the edge of the wafer in order to evenly spread a layer of that analyte over the whole surface. This allows for even spreading of the analyte, but does not guarantee the total mass seen by the detector. In order to control the total mass seen by the detector, a second series of samples were prepared with

a revised preparation process in 2022.

The old samples were prepared by Kragenborg J. from the University of Utrecht on silicon wafers 25.4 mm in diameter. These samples were prepared in Utrecht and then shipped to the Atominstitut for evaluation. The following table lists the intended parameters for the first series of samples.

Sample name	Sphere diameter [nm]	Intended surface coverage [ng/mm^2]	Volume of PS solution [μL]	Volume of upw [μL]
PS20_10	20	10	33	467
PS20_15	20	15	50	450
PS20_100	20	100	333	167
PS70_10	70	10	33	467
PS70_15	70	15	50	450
PS70_100	70	100	333	167
PS150_10	150	10	33	467
PS150_15	150	15	50	450
PS150_100	150	100	333	167

Table 2: List of the first series of spin coated samples.

The samples were prepared on clean quartz wafers. The quartz wafers were first cleaned in an ultrapure water (UPW), acetone and ethanol (1:1:1) mixture for 15 minutes using an ultrasonicator, and then an additional 15 minutes in UPW only. Afterwards, the wafers were placed in a mixture of UPW, hydrogen peroxide (30 wt.%, Sigma-Aldrich) and ammonium hydroxide (28-32 wt.% in H_2O, Sigma-Aldrich) (5:1:1), and heated to 65 °C for 30 minutes. This converts the oxide surface layer of the quartz glass into surface hydroxyl groups by partially etching. To quench the etching, the reflectors were placed in room temperature UPW and heated to 95 °C to remove any surface absorbed ammonium species for 30 minutes. The clean wafers are blown dry using N_2, and placed in an oven at 130 °C for 1 hour to dry.

After the wafers are cleaned, 10 μL of the polystyrene solution is pipetted onto a wafer and spincoated at 750 rotations per minute. For reasons not completely known, there were mixups in the preparation process for the older samples, and the surface density of the pipetted analyte was not known for certain. In addition to this, based on previous work done with similar samples, it was noted that around 40% of the deposited analyte remains on the wafer after the spin coating process. Another fact to note is that due to the size of the wafers used, homogeneous spreading of the particles was rather unlikely, and therefore clumping of particles was expected towards the edges of the wafer.

The new samples were prepared by K.B. Siebers from the University of Utrecht. The wafers were provided by the Atominstitut and shipped by post to Utrecht, where they were

cleaned, functionalized and spin coated before being mailed back. While the cleaning process stayed the same, the rest of the preparation process was done as follows:

1. **Functionalizing** The grafting of the hydrophobic layer takes place in a nitrogen glovebox (Labmaster, <1 ppm O_2 and H_2O). The reflectors are placed in a 10 mM solution of octadecyltricholorosilane (ODTS) (99%, Sigma-Alrich) in anhydrous toluene (99.9% stored over 4Åmolecular sieves, Alfa Aesar). After 10 minutes, the reflectors are taken out of the solution and washed with anhydrous toluene. The reflectors are then removed from the glovebox and placed in an oven at 130 °C for 5 minutes to anneal the hydrophobic ODTS layer. In order to selectively remove the hydrophobic layer by UV/ozone treatment, a custom brass photomask was manufactured (see Figure ...). The mask was made to perfectly fit the 30 mm diameter quartz reflectors, and features a hole a hole in the center to allow for a part of the reflector to be exposed to the UV/ozone treatment. Two versions of the mask were made, with hole diameters of 6.5 and 7.5 mm, with the former being used for the sample preparation. The brass mask is placed over the reflector and both are then placed in an UV/ozone cleanser (Osilla Ltd) for 30 minutes.

2. **Spin coating** The specific sample that could be prepared in time for this work to be completed utilized *Fluoresbrite* YG fluorescent polystyrene nanospheres with a diameter of 200 nm. A dilution was made such that a 5 microliter deposition spread over a circular area 6.5 mm in diamater would have a surface density of 10 ng/mm^2. The spin coating process had to be conducted at a lower spinning rate of 500 rpm so as to prevent the analyte from being pushed over the edge of the reflector by the rotation. Higher spinning rates were found to increase the coffee-stain effect at the edges of the hydrophillic area, while lower spinning rates provided no significant differences to stagnant drying.

No definitive information could be found on the surfactants used in the polystyrene sphere solutions. Other products from the same supplier, like the hydrophobic polymer matrices such as polystyrene, list the usage of surfactants shown in Figure 36. The most notable among them is sodium dodecyl sulfate (SDS), which is known to be used as a surfactant in non fluorescent polystyrene nanospheres made by a different supplier and used by the same lab in University of Utrecht that procured the samples used in this work. This implies a possible contamination with sodium and sulfur. Also of note is the presence of carbon chains, which cannot be distinguished from the carbon present in the polystyrene spheres themselves.

Surfactants

Catalog Numbers: BLI4605, BLI6110, BLI3945

DESCRIPTION

Surfactants are commonly utilized with microspheres composed of hydrophobic polymer matrices such as polystyrene to facilitate bead wetting and deter or treat aggregation. Common concentrations are ~0.1% for uncoated polymer beads, and ~0.01% in the storage buffer of coated polymer, magnetic, and silica beads. The type and concentration of surfactant should be optimized to achieve best performance. As surfactant associates with the bead surface and can interfere with binding, it is washed out prior to bead coating or use of the coated microsphere reagent.

TRITON® X-100 NONIONIC SURFACTANT

Triton® X-100 is a nonionic surfactant. It is often used in the storage buffers of coated bead suspensions. Very low concentrations may be used in wash or binding buffers if needed (e.g. 0.0005%). (Molecular Weight: 625.00 [amp])

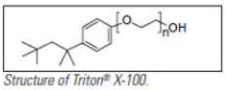

Structure of Triton® X-100.

TWEEN® 20 NONIONIC SURFACTANT

Tween® 20 is a nonionic surfactant. It is often used in the storage buffers of coated bead suspensions. Very low concentrations may be used in wash or binding buffers if needed (e.g. 0.0005%). (Molecular Weight: 1,227.50)

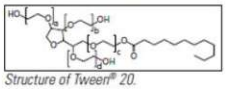

Structure of Tween® 20.

SODIUM DODECYL SULFATE (SDS) ANIONIC SURFACTANT

Sodium dodecyl sulfate (SDS) is an anionic surfactant, which will decrease hydrophobicity and can participate in charge stabilization of the suspension. SDS is a more rigorous surfactant that is commonly used in uncoated polymer bead preparations. (Molecular Weight: 238.38)

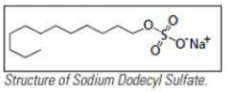

Structure of Sodium Dodecyl Sulfate.

REGISTERED TRADEMARKS

1. Triton® is a registered trademark of The Dow Chemical Company.
2. Tween® is a registered trademark of ICI Americas, Inc.

STORAGE AND HANDLING

Storage Store desiccated at 4°C.

Handling Proper laboratory technique should be followed to safeguard against introduction of contaminants while pipetting.

This product is for research use only and is not intended for use in humans or for *in vitro* diagnostic use.

Figure 38: Short summary of the different surfactants used by the supplier of the fluorescent nanospheres. Figure from Ref. [16].

Finally, the exact fluorescent dye that is used to mark the polystyrene nanospheres is not disclosed by the supplier. A number of different dyes are used for the yellow-green fluorescent marking, and these are listed in Figure 37. All of the dyes are organic in origin and contain carbon, and some may contain nitrogen or fluorine. Again, it is important to note that the spectrometer cannot distinguish between the carbon fluorescence originating from the polystyrene, and that which is coming from the fluorescent dye.

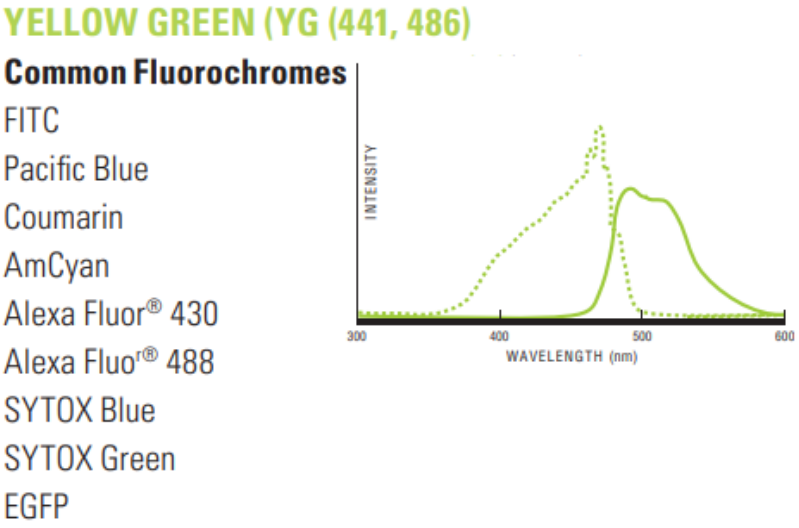

Figure 39: List of different fluorescent dyes used by the supplier of the fluorescent nanospheres. All of the dyes contain carbon. Pacific Blue contains fluorine, and the EGFP dye contains nitrogen. Figure from Ref. [17].

4.1.3 Aluminosilicate samples

To clean the wafers, the surface of the wafers is first wiped off to manually remove most of the previous analytes. The wafers are then cleaned with Decon 90 and triple distilled water, before being placed in an ultrasonic bath while submerged in a 50% solution of nitric acid (HNO_3) for 5 minutes. Afterwards, the wafers are placed in another ultrasonic bath, this time submerged in pure triple distilled water for 5 minutes, before being cleaned with acetone to remove the remaining liquid residue.

To prepare the analytes, 50 mg of a certified reference material is mixed with 2.5 ml of 1 wt.% Triton X-100. Silver is then added as an internal standard, with a concentration of 1000 mg/kg, and the solution is vortexed for 30 seconds. Afterwards, the solution is placed in an ultrasonic bath for 15 minutes, before being vortexed for another 30 seconds. Ten microliters of the solution is then pipetted onto three siliconized quartz wafers and dried on a heating plate for 5-10 minutes.

4.2 Spectrometer operation

4.2.1 Activation

The x-ray generator can only be switched on with the water cooling valves open. If water cooling is present, the generator is manually switched on, and voltage and current are slowly raised to 30 kV and 30 mA respectively. The detector and the peltier cooling assembly are subsequently switched on as well, allowing the detector crystal to be cooled to 220 K while

samples are prepared. The cooling system is left running during operation, and is only shut down once all measurements for the day are complete.

4.2.2 Initial alignment

As the vacuum chamber and x-ray tube are secured to the optical table separately, alignment of the x-ray tube is necessary after each round of maintenance or engineering work that involves moving the vacuum chamber, as was the case when a thicker Kapton was installed over the entrance window of the chamber.

To perform this alignment, the aluminum shielding over the x-ray tube must be removed, and a spindle located at the top of the x-ray tube must be turned until the beam is visible on the camera feed. Once maximum intensity is found, fine tuning can be done by measuring the intensity of the Cr-Ka scatter in air, and leaving the x-ray tube in a position with the highest intensity. The aluminum shielding is then placed back on the x-ray tube, and a radiation check is performed.

4.2.3 Measurement process

Once the spectrometer is properly aligned and switched on, the desired sample can be introduced into the vacuum chamber and placed on the aluminum sample stage. It is held loosely in place by four screws that prevent it from moving during the evacuation of the chamber. Once the chamber is closed, the beam can be switched on, and the vacuum pump started.

Once the pressure inside the chamber falls below 1 mbar, vertical alignment is performed. To accomplish this, the sample stage is moved vertically up towards the detector while the intensity of a particular fluorescence line is observed, usually silicon or any element present in a large concentration in the sample. If both are measured, the fluorescence of elements present in the sample are given priority, as their maximum indicates correct positioning in the case of an off-center sample. Once a maximum of fluorescence is found (see Figure 40), the sample stage is brought to that position, and kept there until all measurements concerning that sample are complete.

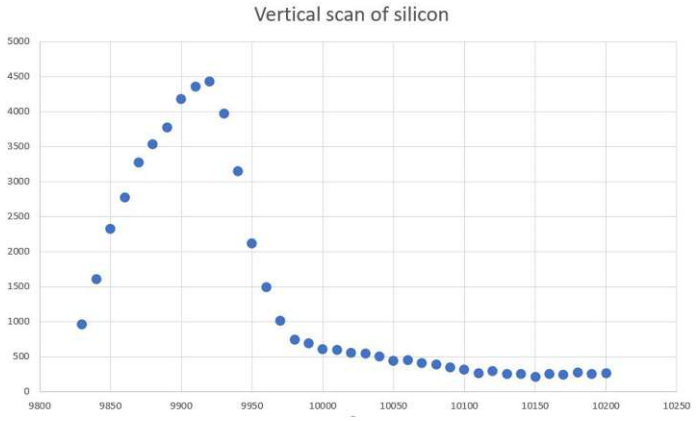

Figure 40: An example of a vertical scan conducted on one of the samples used for the absolute calibration of carbon. The intensity of silicon is plotted over the vertical position of the sample stage n micrometers. A clear peak of fluorescence is visible, which marks the position at which measurements should be done.

After vertical alignment, it is necessary to conduct angle alignment, in order to ensure the best possible reproducibility of results, especially in the case of angle scans of spin-coated samples. To do this, a relatively quick angle scan is performed while following the intensity of silicon fluorescence. This scan usually covers a range of 0.5-0.6°. Once the scan is complete, the characteristic bulk fluorescence signal can be seen, and from it the critical angle can be identified (see Figure 41). Once identified, the angle scale can be calibrated so the critical angle lands on 0.33°, thus making sure that each sample is measured under the same geometric conditions.

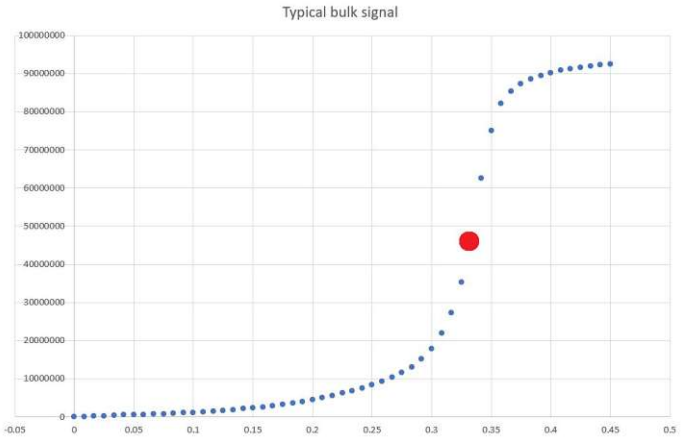

Figure 41: Example of a bulk signal seen when performing an angle scan. The intensity of silicon is plotted over the glancing angle of the x-ray beam in degrees. The big red dot marks the critical angle. The critical angle can always be identified as the region with the steepest incline, or in other words where the second derivative of the curve changes signs, from positive (convex) to negative (concave).

After alignment is complete, the sample can be measured. For dried residue samples, a time of 100 or 1000 seconds is chosen, depending on the amount and sensitivity of the element of interest. For spin-coated samples, an angle scan is performed, covering angles from 0° to 0.45° in around 100 steps, with a total measurement time set to around 20-24 hours, or around 70 hours if a less sensitive sample is in question. The initial angle scan during alignment usually provides enough information about the amount of carbon present to estimate a measuring time for each point that will result in good counting statistics. Once a suitable scanning time is chosen, the spectrometer is left running overnight or during the weekend.

One important note concerning the aluminosilicates is the noticeably larger mass of pipetted samples compared to samples usually measured by the spectrometer. Because of this higher mass, the detected countrate was much higher than what the detector was set up to process, and caused issues with deadtime calculation and spectrum recording. To combat this, the current on the x-ray generator was lowered to 10 mA, thus ensuring a lower intensity of the exciting beam, which in turn brought the measured countrates down to nominal levels.

All data was gathered as .spe and .mca files, and subsequently analyzed with QXAS and jgixa.

5 Polystyrene microspheres

5.1 First series of spin coated samples

Sample name	Carbon nanoparticle diameter [nm]	Intended surface density [ng/mm^2]
PS20-10	20	10
PS20-15	20	15
PS20-100	20	100
PS70-10	70	10
PS70-15	70	15
PS70-100	70	100
PS150-10	150	10
PS150-15	150	15
PS150-100	150	100

Table 3: List of the first series of polystyrene microsphere samples. The first number in the sample name denotes the size of the polystyrene spheres in the analyte, and the second number the intended surface density in ng/mm^2

The first series of spin coated polystyrene nanospheres were already measured with the TXRF spectrometer before the new *Amptek* detector was installed in April of 2021. These measurements were done with a *Ketek* detector, with a *Moxtek* AP3.3 polymer window and an active surface area of 18 mm^2, and the results were far from ideal, with low carbon intensities and large variations over the multiple measurements needed for a complete angle scan. These measurements were then repeated after the installation of the new *Amptek* detector. As was mentioned before, due to certain oversights and miscommunication, the exact surface density was unknown for each sample, making for inconclusive quantification. However, the results were promising enough to warrant further investigation, especially through the establishment of an absolute calibration curve for carbon.

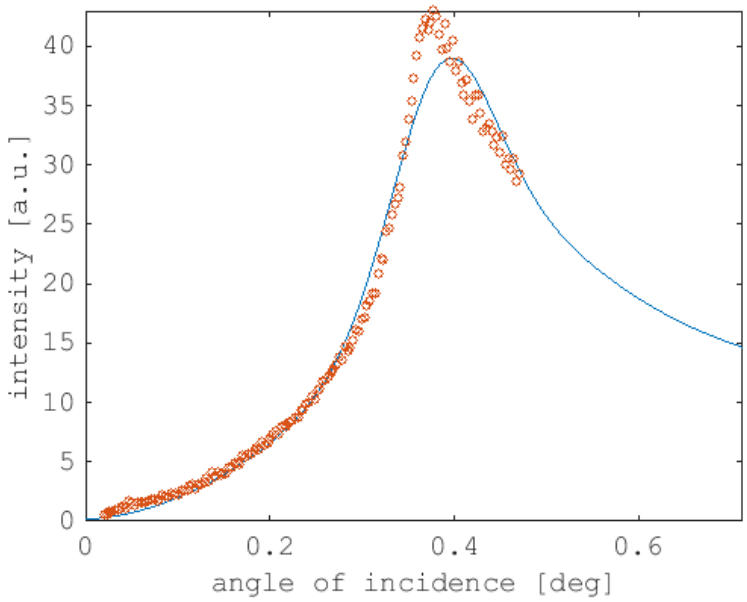

Figure 42: PS20_10 angle scan data, fitted to a simulated curve of a reflecting carbon layer with a thickness of 28.34 nm, and a density of 2.76 g/cm^3.

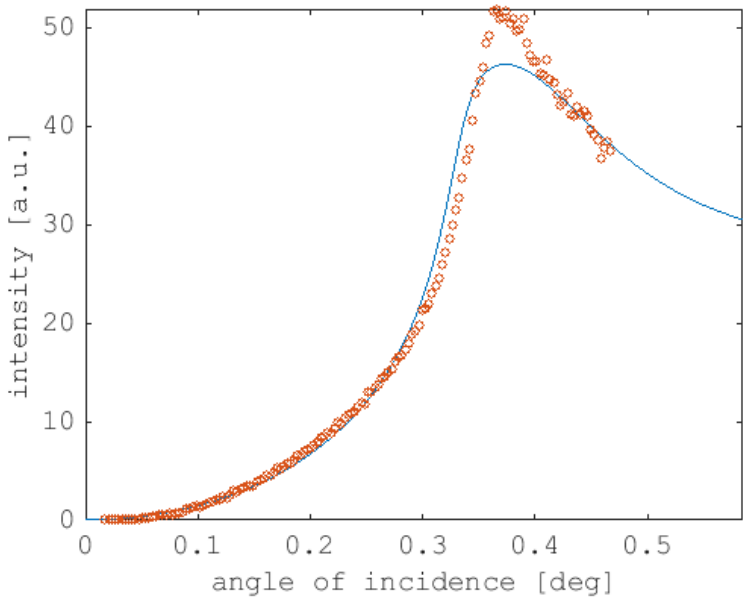

Figure 43: PS20_15 angle scan data, fitted to a simulated curve of a reflecting carbon layer with a thickness of 16.86 nm, and a density of 2.75 g/cm^3.

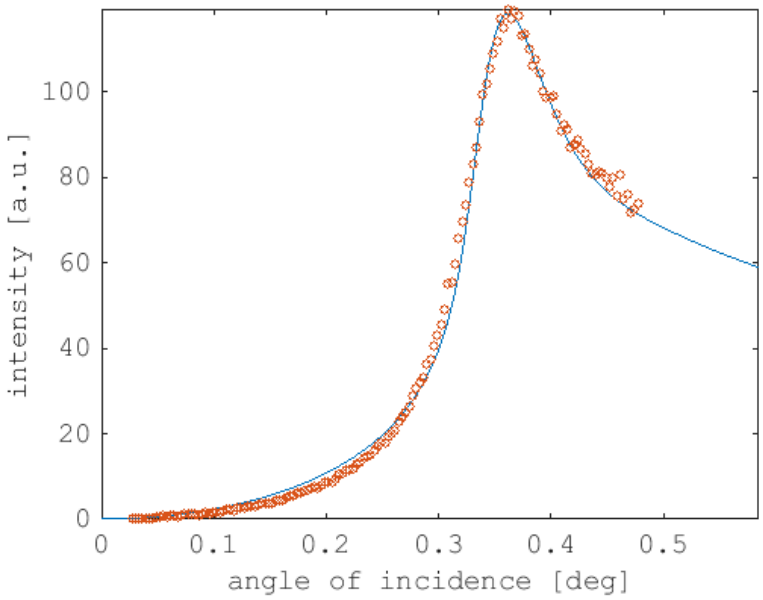

Figure 44: PS20_100 angle scan data, fitted to a simulated curve of a reflecting carbon layer with a thickness of 28.01 nm, and a density of 2.51 g/cm^3.

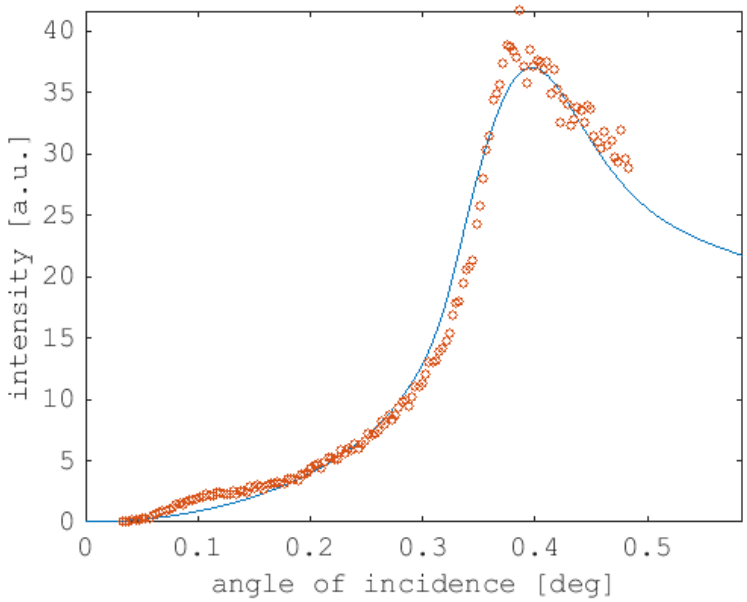

Figure 45: PS70_10 angle scan data, fitted to a simulated curve of a reflecting carbon layer with a thickness of 22.33 nm, and a density of 2.82 g/cm^3.

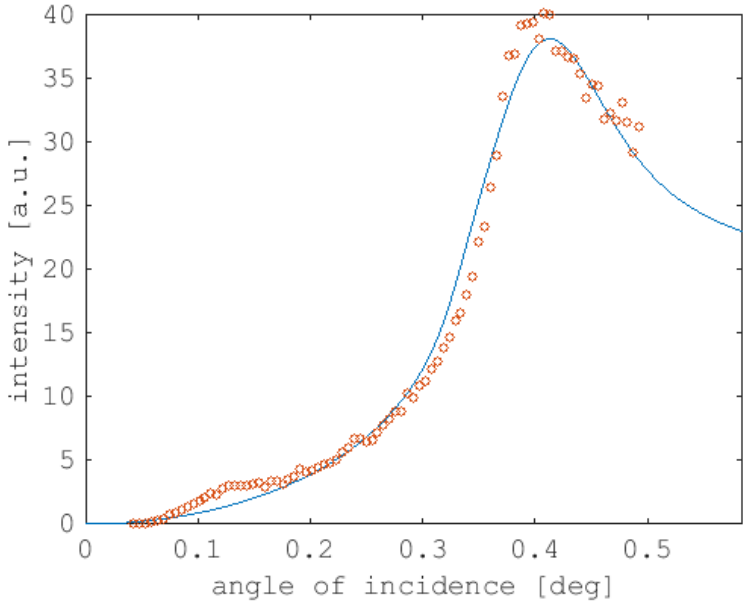

Figure 46: PS70_15 angle scan data, fitted to a simulated curve of a reflecting carbon layer with a thickness of 21.67 nm, and a density of 2.97 g/cm^3.

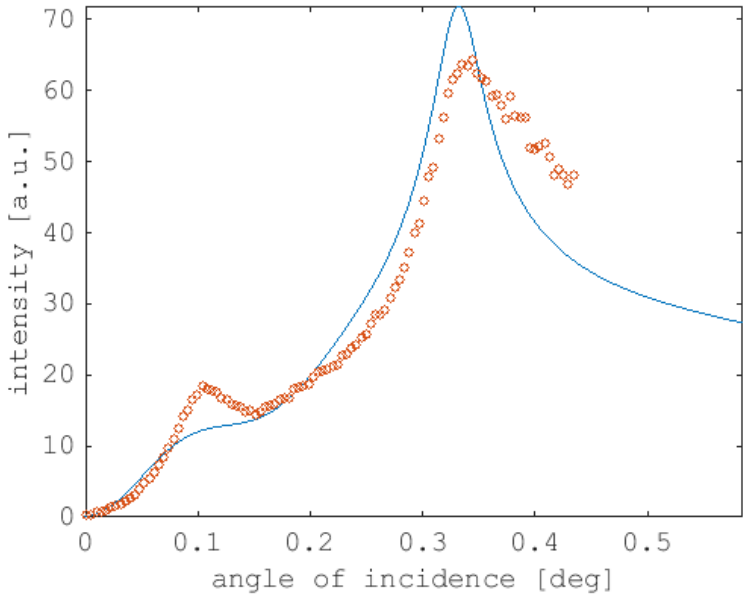

Figure 47: PS70_100 angle scan data, fitted to a simulated curve of two carbon layers, one reflecting and one non-reflecting. The reflecting carbon layer has a thickness of 12.47 nm and a density of 2.14 g/cm^3, and the non-reflecting layer has a thickness of 40 nm, and a density of 0.09 g/cm^3.

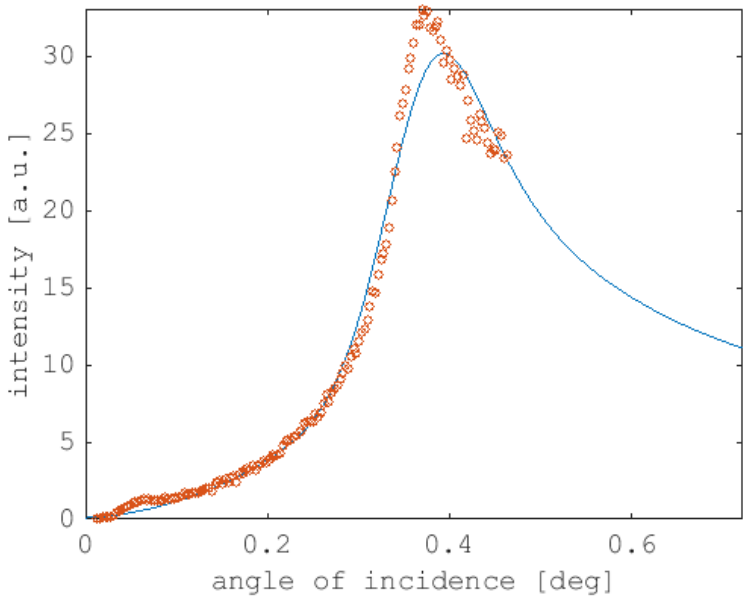

Figure 48: PS150_10 angle scan data, fitted to a simulated curve of a reflecting carbon layer with a thickness of 39 nm, and a density of 2.7 g/cm^3.

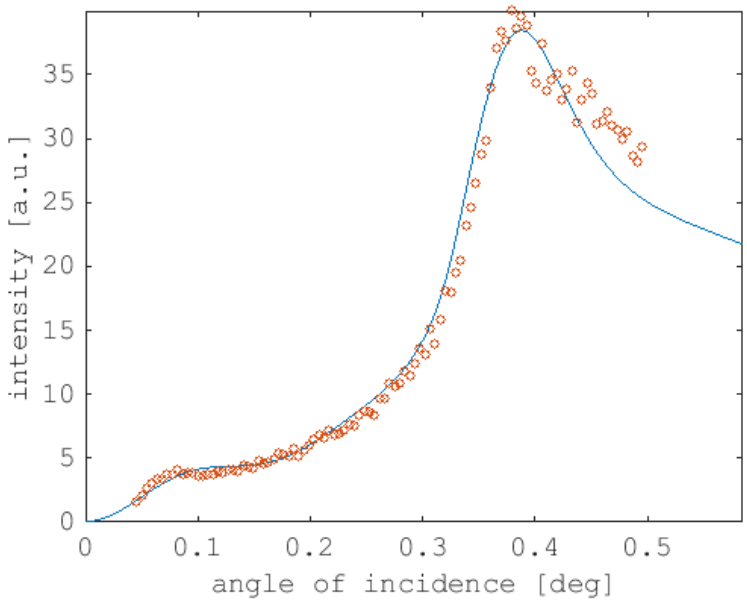

Figure 49: PS150_15 angle scan data, fitted to a simulated curve of two carbon layers, one reflecting and one non-reflecting. The reflecting carbon layer has a thickness of 24.89 nm and a density of 2.74 g/cm^3, and the non-reflecting layer has a thickness of 40 nm, and a density of 0.1 g/cm^3.

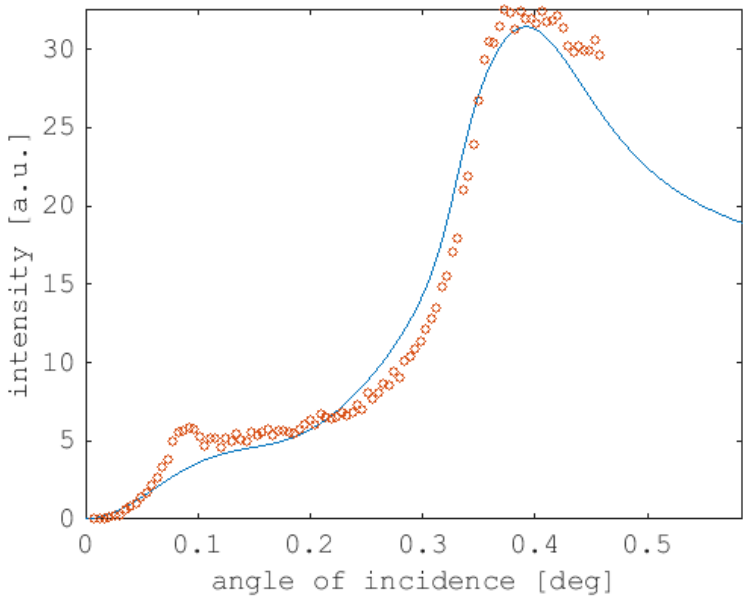

Figure 50: PS150_100 angle scan data, fitted to a simulated curve of two carbon layers, one reflecting and one non-reflecting. The reflecting carbon layer has a thickness of 20.37 nm and a density of 2.8 g/cm^3, and the non-reflecting layer has a thickness of 32.98 nm, and a density of 0.1 g/cm^3.

A couple of things can be noted about the fluorescence signals measured, even without proper quantification:

1. The recorded signals generally show a "thin layer" behavior around the critical angle of quartz. This was to be expected of the PS20 samples, which feature polystyrene nanospheres 20 nm in diameter. The samples with larger spheres, 70 and 150 nm respectively, under the same assumption of forming a homogeneous layer with a thickness equal to the sphere diameter, would then exhibit a different fluorescence signal, rather than a thin layer peak. This is not seen in these measurements.

2. Samples with presumably higher mass density (PS70_15, PS150_15 and PS150_100) show an "early peak" at around 0.1°. While not perfectly fitting of a thin layer, this sort of signal is indeed encountered when dealing with larger particles, which these samples do contain. The low intensity of these early peaks brings the carbon deposition into question, as even though the sample should mostly contain the polystyrene nanospheres, the signal is dominated by the thin layer portion. With no way to properly control the particle deposition at the time, no significant conclusions could be drawn.

3. While quantification regarding the observed mass and the surface density of the samples was impossible, due to a lack of confirmed parameters or a calibration curve, qualitatively the measurements fit a certain pattern. In general, the higher the numbers designating the sample, the higher the intensity observed. The X_10 and X_15 samples

usually had comparable carbon intensities, while the X_100 samples exhibited vastly stronger peaks, although not by an entire order of magnitude, as the naming would suggest. Larger nanosphere diameters mostly match with higher intensities, which isn't surprising.

As can be seen, all the PS20 samples can be fitted with a single reflecting layer, although the fit deviates the most near the peak at the critical angle. PS70 requires a second non-reflecting layer above the reflecting layer to simulate the early peak for the _15 and _100 samples, with the same being true for the PS150 samples.

While these conclusions were certainly enough to show the method working and the instrument as sensitive enough to observe and potentially quantify carbon, there was little concrete data to show for it. To combat this, it was decided that an absolute calibration for carbon should be established, the data from which would then be used to quantify the conducted angle scans and conclude how sensitive the instrument was, and what sort of nanosphere sizes and analyte concentrations would be used for a new series of spin coated samples.

5.2 Calibration and quantification

To properly quantify how sensitive the instrument was to the carbon in the polystyrene nanosphere samples, a calibration had to be established. The calibration standards produced were simple dried residue samples, and were not spin coated like the samples they would be used to quantify. This could potentially pose a problem, as the two different deposition processes inevitably results in different angle dependencies of the carbon fluorescence signal, leading to different intensity ratios at different angles. It was decided that a point should be found, where the theoretical angle signals of two samples with the same mass, with these depositions (particle and layer) would intersect. It was judged that a glancing angle of about 75% of the critical angle should suffice. For convenience, this was adapted to 0.24°, which is about 72.7% of the critical angle of quartz. Because of these reasons, the calibration samples would be measured at an angle of 0.24°, and the calibration data obtained could only be used to quantify results measured at the same angle.

With regards to the masses the calibration standards would cover, it was decided that samples of 20 ng increments would be produced to cover a "gap" between the two old samples made by L. Rachbauer, which had masses of 22.9 ng and 250 ng. A third sample of 3750 ng was already examined but showed signs of self absorption, so the former two were chosen as edges of the range of masses which would be quantified. Twelve new samples were made, listed in Table 1 and measured for 1000 seconds, twice each at a glancing angle of 0.24°. The results can be seen in Figure 51.

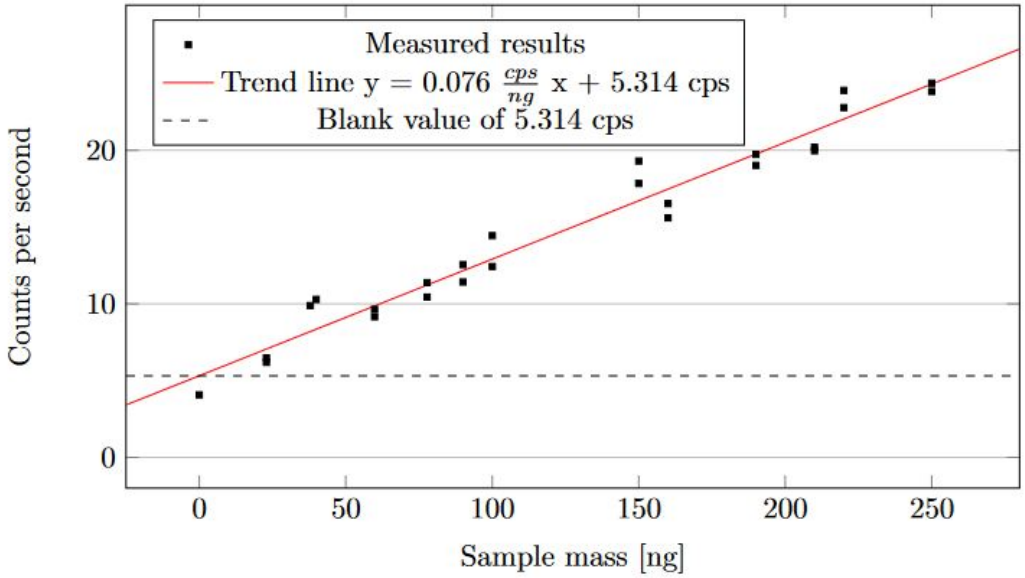

Figure 51: Absolute calibration curve for carbon

The fitted linear curve has an equation of $y = 0.076\frac{cps}{ng} \cdot x + 5.314cps$ What must be noticed immediately is a relatively high blank value, which so far seems to be present on every clean wafer measured. This might very well stem from the presence of nanoplastics in solutions and water used to clean the wafers, as it is very hard to filter out. Taking into consideration the given incline of the calibration curve, the blank value would be equal to about 70 ng of carbon present on any given wafer surface. However, this value can vary from wafer to wafer, depending on the cleaning process and random chance, as well as the amount present in the atmosphere and the water used to make solutions. This blank intensity must be subtracted when calculating detection limits.

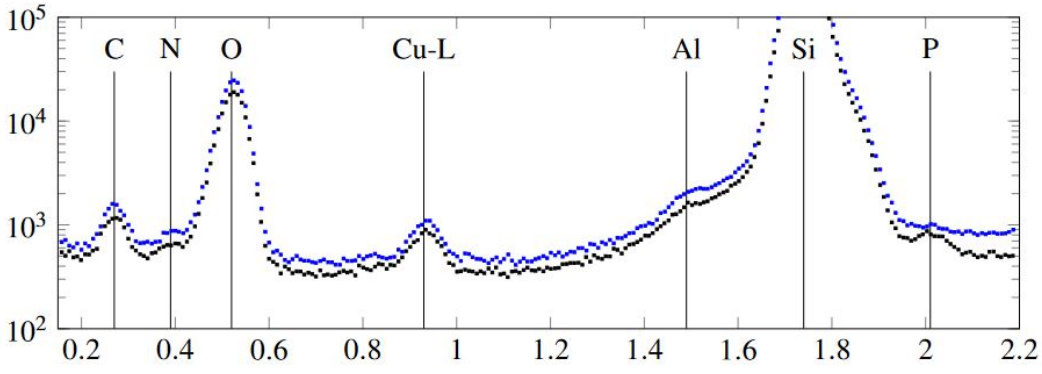

Figure 52: Low energy part of the spectra for the blank sample (black dots) and the sample containing 22.9 ng of carbon (blue dots).

Sample mass [ng]	Corrected counts per second	Background counts per second	Limit of detection [ng]
22.9	0.87	7.68	6.9
22.9	1.17	7.78	5.19
37.88	4.58	5.78	1.89
39.89	4.98	5.7	1.82
59.82	4.33	6.78	3.42
59.82	3.85	6.52	3.77
77.77	5.13	7.19	3.86
77.77	6.07	7.55	3.34
90	7.24	6.02	2.9
90	6.11	5.79	3.36
100	9.13	6.56	2.66
100	7.12	6.22	3.32
150	12.53	7.77	3.17
150	13.99	7.51	2.79
160	10.29	7.13	3.52
160	11.22	6.76	3.52
190	14.42	6.65	3.22
190	13.71	6.53	3.36
210	14.66	7.83	3.8
210	14.89	7.06	3.55
220	18.59	7.27	3.03
220	17.47	7.45	3.26
250	18.52	6.99	3.39
250	19.05	6.78	3.24
Mean limit of detection			**3.45**

Table 4: Corrected intensities and limits of detection for calibration samples.

It can immediately be noted that the instrument is very sensitive to carbon, at least compared to the setup used before the installation of the *Amptek* detector. A simple comparison with the sensitivity and detection limits values obtained by L. Rachbauer (Ref. [5]) shows a drastic increase in sensitivity, but higher detection limits. While the increased sensitivity is chiefly thanks to the increased detector active area and the ultrathin window used, the detection limits being higher has two main causes.

1. The background signal in the low energy regions of spectra seems relatively high (see Figure 53). While thermal noise would be the first suspect, this seems unlikely, as the detector crystal is constantly kept at around 215-220 K, which is more than sufficient to minimize leakage current and thermal noise. The most likely scenario is an increase

in electronic noise from the unwanted electrons that reach the detector crystal. While the electron trap should prevent them from reaching the crystal, it is possible that the magnetic field is not strong enough.

2. L. Rachbauer operated on the assumption that the blank value of his samples was zero. This phenomenon was not taken into account until calibration was done using the *Amptek* detector, and the corrected intensity values would therefore be lower in that case, even for the previous setup. This increases the perceived discrepancy between the results.

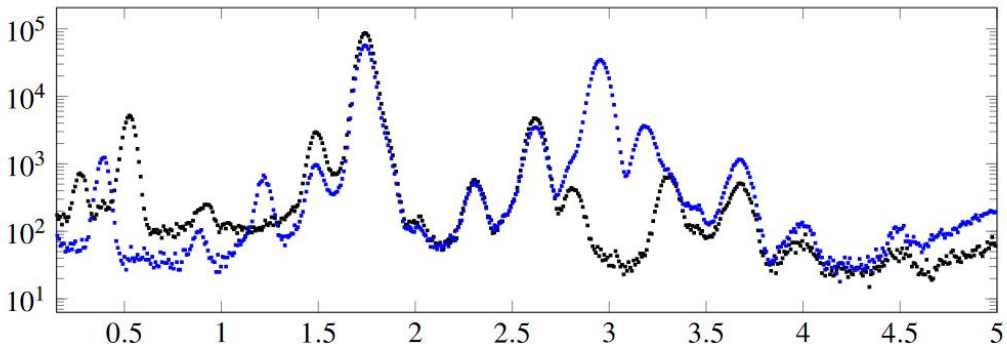

Figure 53: Two spectra of a sample containing 250 ng of carbon, one measured for 200 seconds in vacuum (black), and the other for the same duration in air (blue).

While nothing concrete can be done about the blank value present on the samples, a short investigation into background reduction was done, the results of which are presented later. The results of the calibration could be used to quantify the previously conducted angle scans, with their carbon intensities at a glancing angle of 0.24°put into the obtained calibration equation so that corresponding mass estimates could be calculated. The results of this quantification can be seen in Table 4.

Sample name	Counts per second at ω=0.24	Estimated mass [ng]	Estimated surface density [ng/mm^2]
PS20-1	6.58	16.66	0.43
PS20-10	14.22	117.16	3.04
PS20-15	15.82	138.24	3.59
PS20-100	24.26	249.29	6.48
PS70-10	10.19	64.16	1.67
PS70-15	10.36	66.39	1.73
PS70-100	24.3	249.82	6.49
PS150-10	8.37	40.21	1.04
PS150-15	11.2	77.45	1.01
PS150-100	23.82	243.5	6.33

Table 5: Mass and surface density estimates for the first set of polystyrene nanosphere samples

As can be seen, the estimated observed masses of the samples fall squarely in the mass range defined by the calibration samples. If the calibration data is taken as representative of the instrument's sensitivity to carbon in the case of polystyrene nanosphere angle scans at a glancing angle of 0.24°, then the mass and surface density estimations can be taken as guidelines for making new samples.

5.3 Second series of spin coated samples

Sample name	Polystyrene nanosphere diameter [nm]	Surface density [ng/mm^2]
Blank #482	N/A	N/A
PS_FUNC	N/A	N/A
PS_UPW	N/A	N/A
PS200_10	200	10

Table 6: List of the second series of polystyrene microsphere samples. PS_FUNC refers to a sample that only had its surface functionalized, as per the preparation procedure, without any analyte spin coated. PS_UPW contains only ultrapure water spin coated onto the reflector. The blank is a reflector with absolutely no treatment whatsoever, and was taken randomly from the clean quartz reflectors available at the Atominstut.

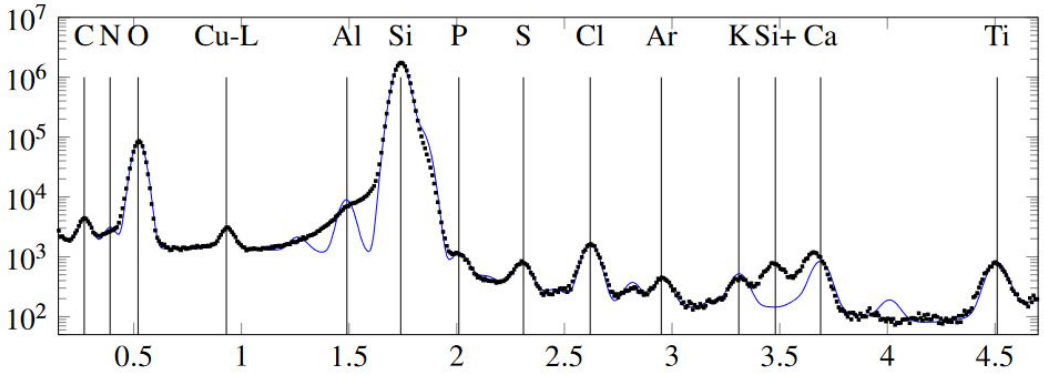

Figure 54: A spectrum of the blank sample, measured at a glancing angle of 0.24° for 3000 seconds.

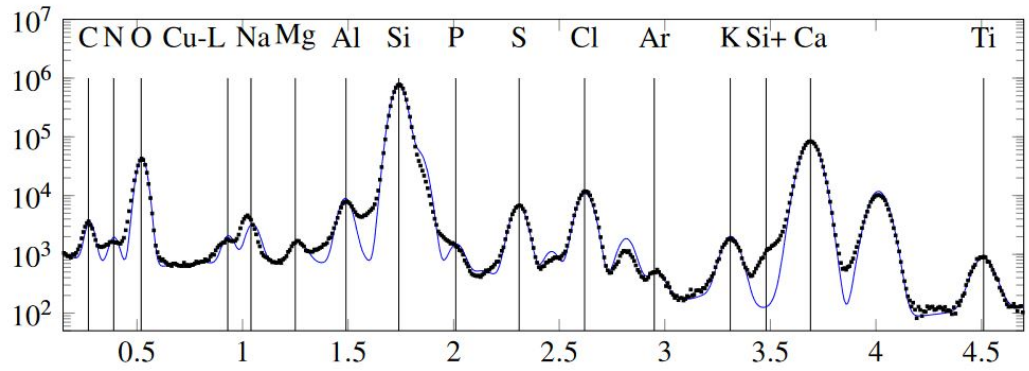

Figure 55: A spectrum of the functionalized sample, measured at a glancing angle of 0.24° for 3000 seconds.

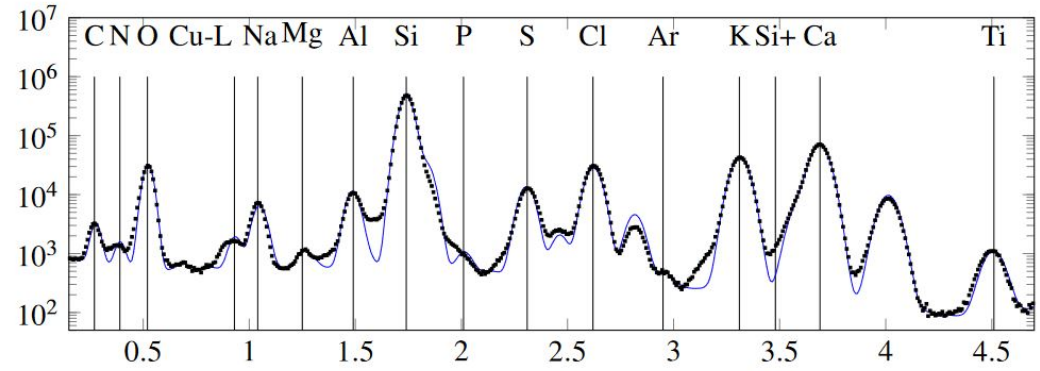

Figure 56: A spectrum of the ultrapure water sample, measured at a glancing angle of 0.24° for 2000 seconds.

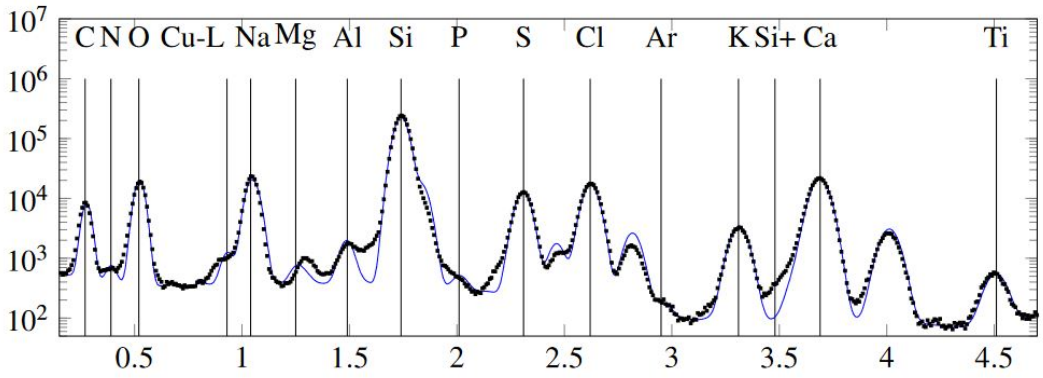

Figure 57: A spectrum of the sample containing 200 nm polystyrene nanospheres, measured at a glancing angle of 0.24° for 850 seconds.

The second set of polystyrene nanosphere samples were prepared after the calibration data provided some insight into the instrument's sensitivity to the previously measured spin coated samples. To account for the previous lack of defined parameters, the new samples would be functionalized with a hydrophobic layer that would ensure the analyte would only be present in the area inspected by the detector, thus guaranteeing that all of the analyte that is pipetted onto the reflector would be detected. This functionalization was also done to decrease the coffee stain effect on the dried analyte. In order to control the deposition of the polystyrene nanospheres, a different type of nanospheres marked with fluorescent dye were used, making them observable with confocal fluorescence microscopy (CFM). This control was done by the partners at the University of Utrecht before being shipped to the Atominstitut.

Due to time constraints, only three samples could be prepared. Since carbon contaminations could come from any of the different steps undertaken during sample preparation, it was decided that measuring samples that represented these steps would be a good idea. Therefore, besides one sample containing the polystyrene nanospheres, three more samples were measured: one completely blank reflector, one reflector functionalized with the hydrophobic layer but containing no analyte, and one reflector functionalized with the hydrophobic layer with ultrapure water spin coated on it.

The samples were measured and analyzed in the same way as the previous ones. The results can be seen below.

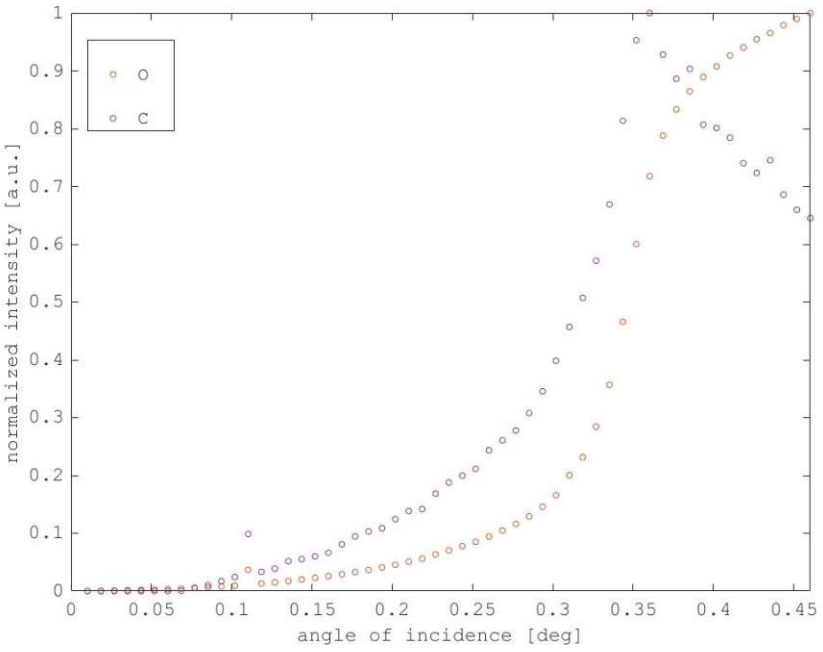

(a) Carbon fluorescence signal of the blank sample.

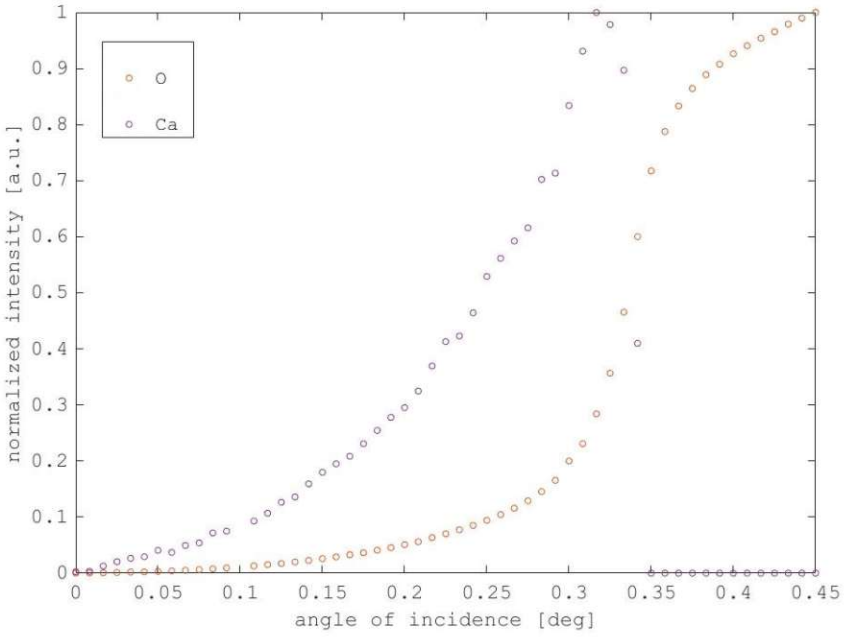

(b) Calcium fluorescence signal of the blank sample.

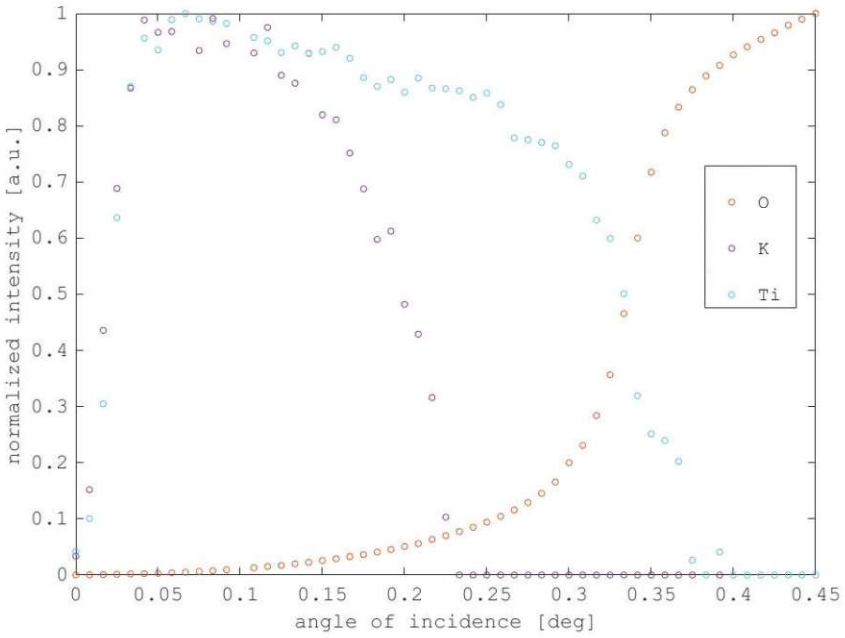

(c) Potassium and titanium fluorescence signals of the blank sample.

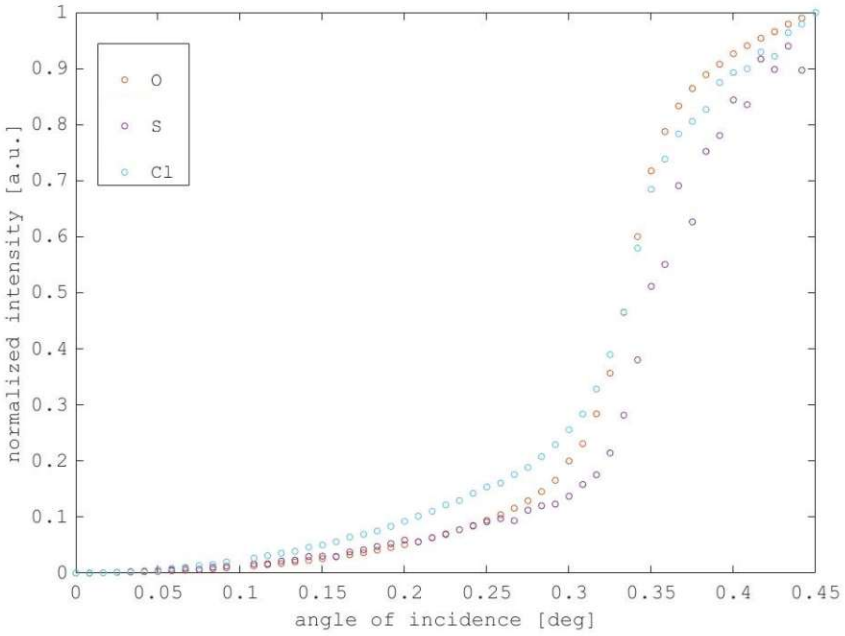

(d) Sulfur and chlorine fluorescence signals of the blank sample.

Figure 58: Fluorescence signals of the different elements present in the blank sample, grouped by signal type. Oxygen fluorescence signal was included in every plot for reference. Intensities are normalized.

As seen in Figure 58, different elements exhibit different fluorescence signals over the course of an entire angle scan. Carbon shows a classical thin layer signal, while the other contaminants fall into one of two groups:

1. **Particle residue signal** These elements exhibit a relatively constant intensity over a large angle range below the critical angle, before dropping to lower or zero intensity after the critical angle. This signal is typically seen in the case of analyte dried on a substrate with no spin coating.

2. **Modified layer signal** These elements generally show a steady rise of intensity in the angle range below the critical angle, peak near the critical angle, before dropping to low or zero intensity after the critical angle. While this behavior suggests a layer-like deposition, the signal is usually slightly modified and can feature an early rise and different slope inclines, implying that the structure of the element at hand is not a pure layer.

Two special cases can be seen in the case of the blank signal, those being sulfur and chlorine, which exhibit a bulk fluorescence signal. These elements are not present in the substrate, and this sort of signal does not appear in any of the other measurements.

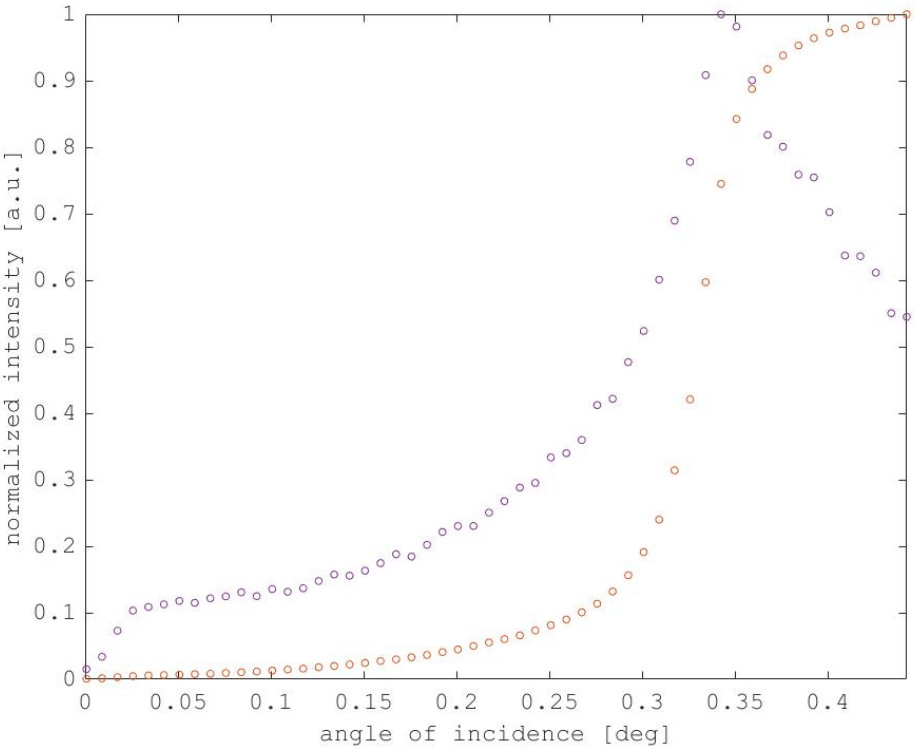

(a) Carbon fluorescence signal of the functionalized sample.

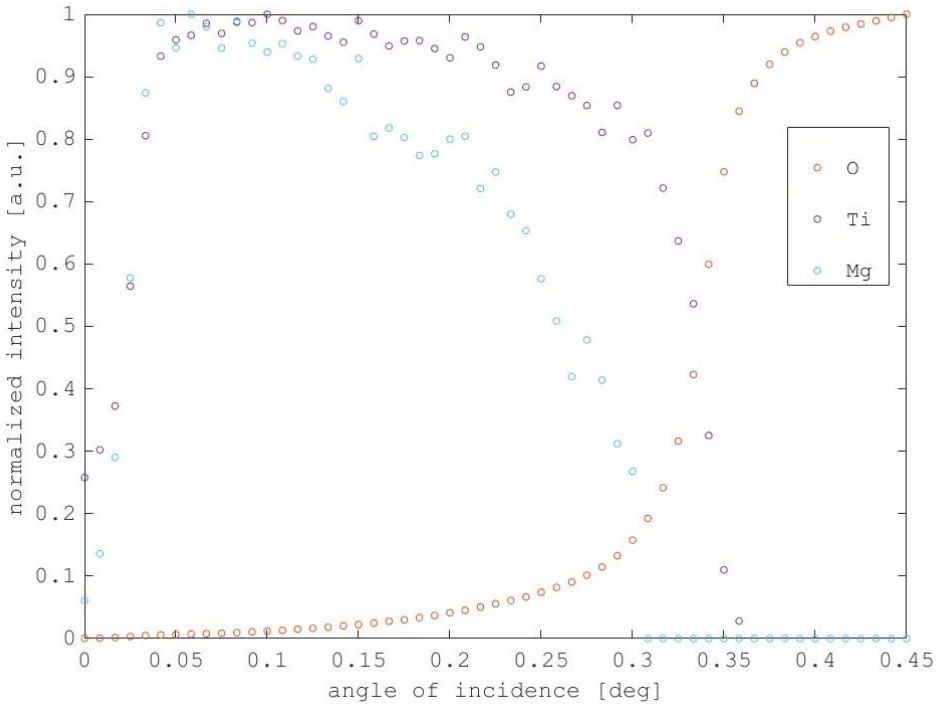

(b) Titanium and magnesium fluorescence signals of the functionalized sample.

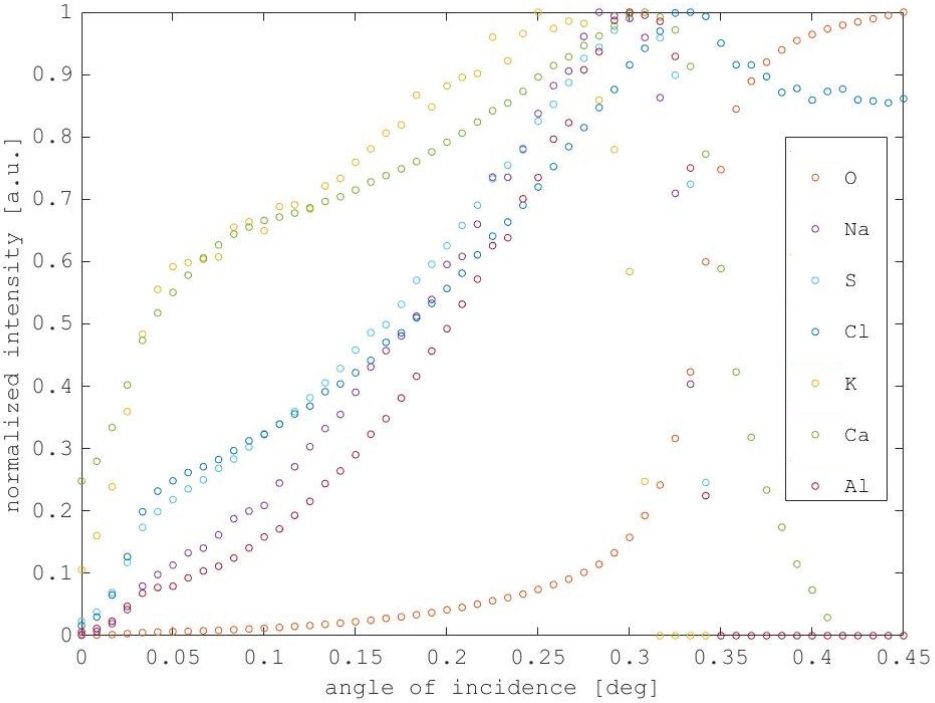

(c) Fluorescence signals of sodium, sulfur, chlorine, potassium, calcium and aluminum of the functionalized sample.

Figure 59: Fluorescence signals of the different elements present in the functionalized sample (PS_FUNC), grouped by signal type. Oxygen signal was included in every plot for reference. Intensities are normalized.

It can be seen that a vast array of different elements are present in the sample, most of which exhibit a modified layer behavior. All of these elements show an early rise in intensity, at a glancing angle of around 0.05°, and a peak slightly before or near the critical angle. It should be taken into account that calcium and potassium (green and yellow data points in Figure 59 c)) intensities suffer from an overlap with the SiKα sum peak, which sits at an energy of 3.48 keV. As the glancing angle approaches the critical angle, the sum peak increases and starts to drown out the peaks of potassium and calcium. This is observed as a drop in intensity near the critical angle, and a deconvolution software would be needed to properly quantify these two elements past this point. In the scope of this work, angle scan analysis was done with the raw spectral data obtained from measurement, therefore peak deconvolution would be an important point in future work.

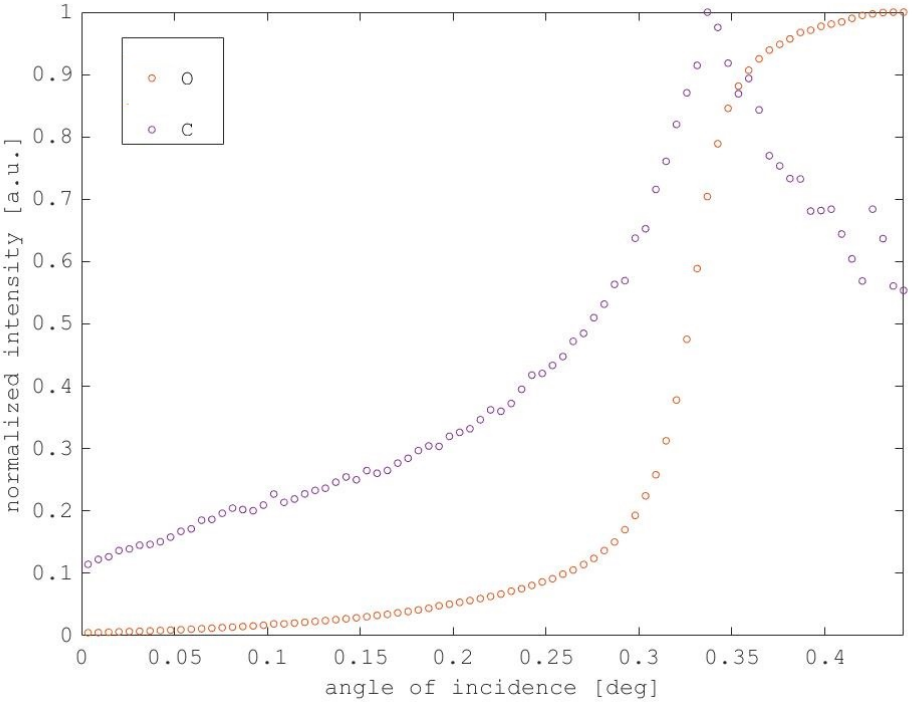

(a) Carbon fluorescence signal of the ultrapure water sample.

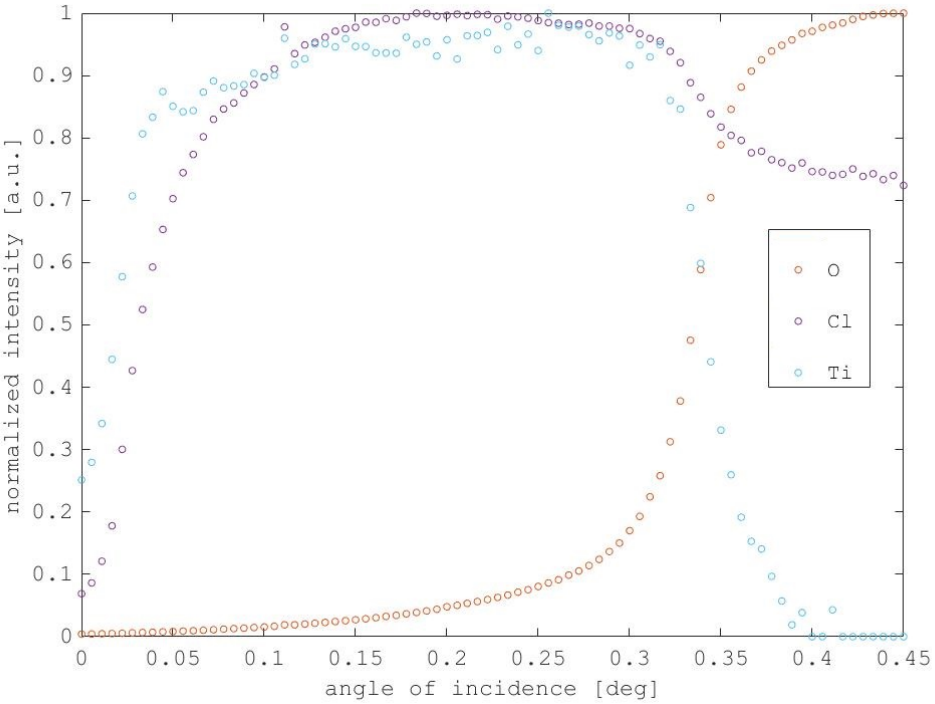

(b) Chlorine and titanium fluorescence signals of the ultrapure water sample.

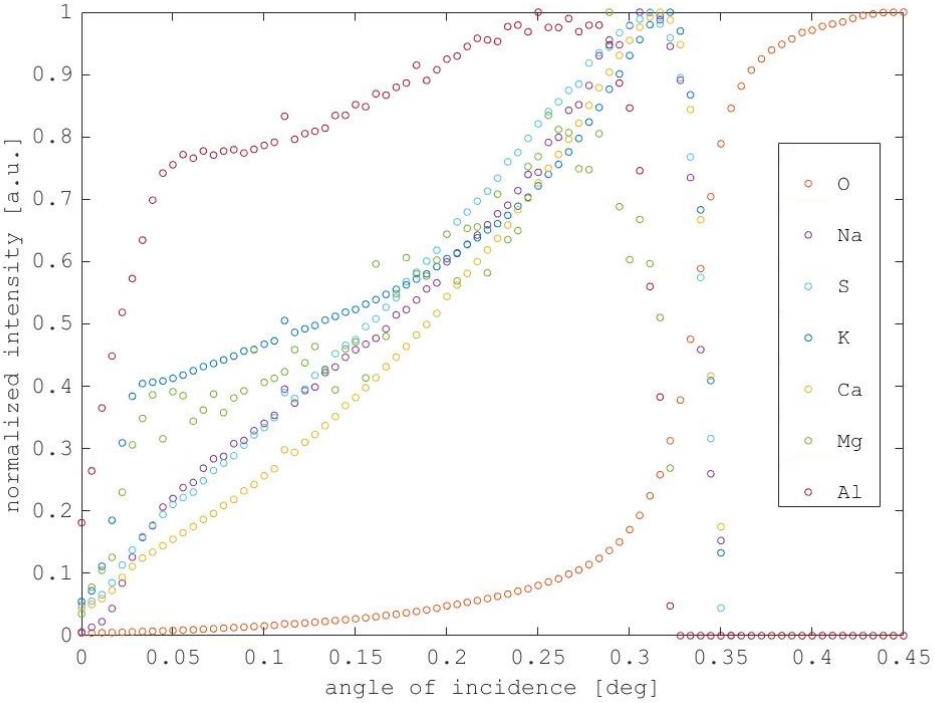

(c) Fluorescence signals of sodium, sulfur, potassium, calcium, magnesium and aluminum of the ultrapure water sample.

Figure 60: Fluorescence signals of the different elements present in the ultrapure water sample (PS_UPW), grouped by signal type. Oxygen signal was included in every plot for reference. Intensities are normalized.

As with the functionalized sample, the carbon signal for the ultrapure water sample follows a layer curve, with an early rise at very low angles. This early rise seems to be in the "negative" angles in this case, which might very well be a consequence of a slightly offset angle scale. Again, the same two principal signal types are seen as with the previous samples.

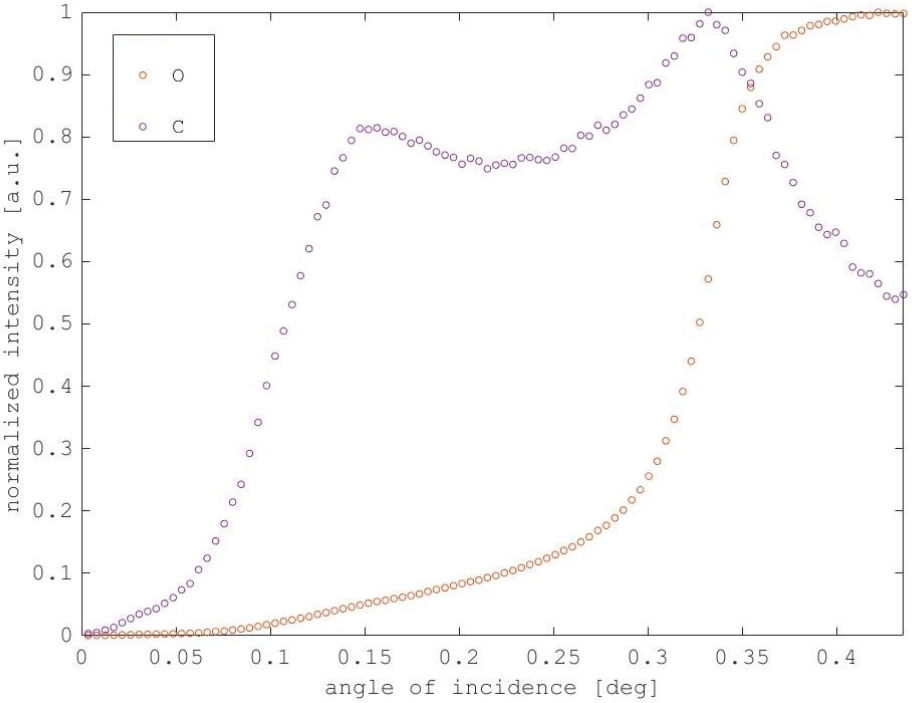

(a) Carbon fluorescence signal of the polystyrene sample.

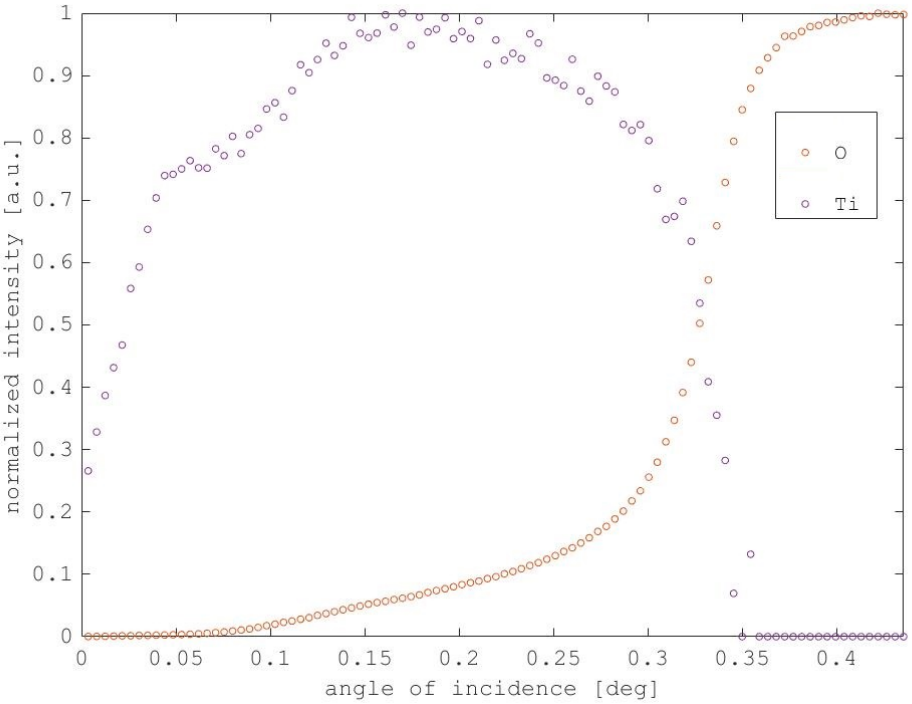

(b) Titanium fluorescence signal of the polystyrene sample.

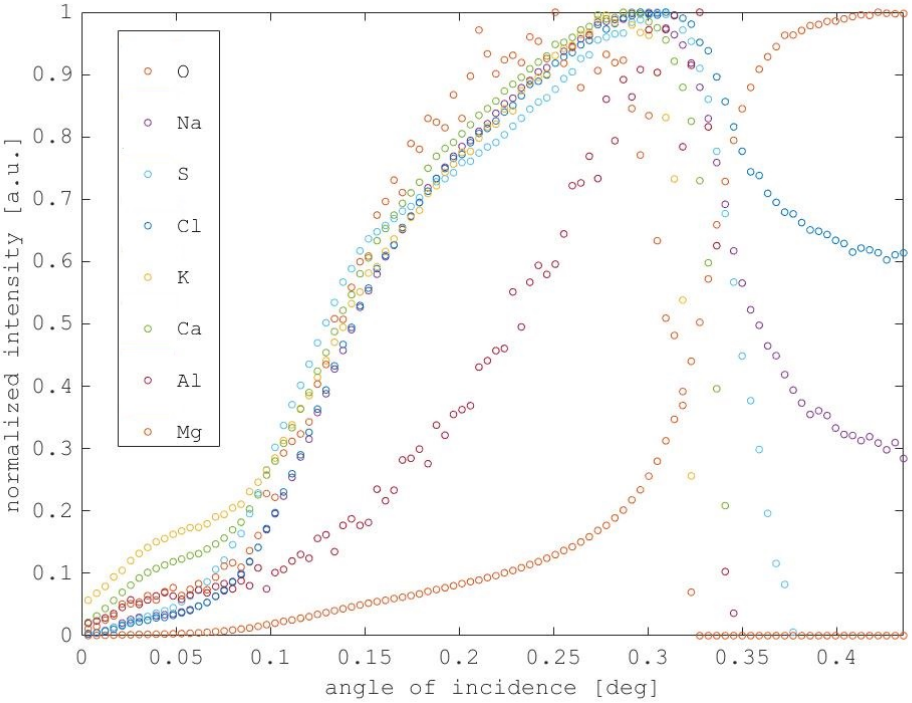

(c) Fluorescence signals of sodium, sulfur, chlorine, potassium, calcium, magnesium and aluminum of the polystyrene sample.

Figure 61: Fluorescence signals of the different elements present in the polystyrene sample (PS200_10), grouped by signal type. Oxygen signal was included in every plot for reference. Intensities are normalized.

In the case of the sample containing the polystyrene nanospheres, carbon exhibits much stronger intensities, and a signal similar to the PS150_100 sample, but with a much more pronounced early peak.

In order to gain some insight into the relative intensities of the elements present in these samples, spectra from a similar angle were taken to be analyzed in QXAS, with the AXIL peak fitting package. A glancing angle of around 0.24°was chosen, since the carbon calibration data should be valid for that glancing angle value. Summary of this analysis can be seen in Table 6.

Sample name	C cps	Na cps	Mg cps	Al cps	S cps	Cl cps	K cps	Ca cps	Ti cps
Blank no. 482	7.31	0	0	25.12	1.79	5.36	1.44	2.85	2.89
PS-FUNC	5.88	5.29	2.37	25.09	22.36	39.44	7.61	356.06	3.52
PS-UPW	8.49	18.5	2.17	50.34	71.42	157.33	266.31	441.41	7.21
PS200-10	57.38	147.02	3.5	17.18	152.43	213.59	47.54	317.89	7.71

Table 7: Intensities per second of different elements present in the second series of spin coated samples. All intensities were obtained by fitting spectra measured during the angle scan at or around a glancing angle of 0.24°. Intensities are presented in counts per second to account for the different measurement times of the samples.

If the element intensities are grouped by sample or element, a visual presentation shows some general trends.

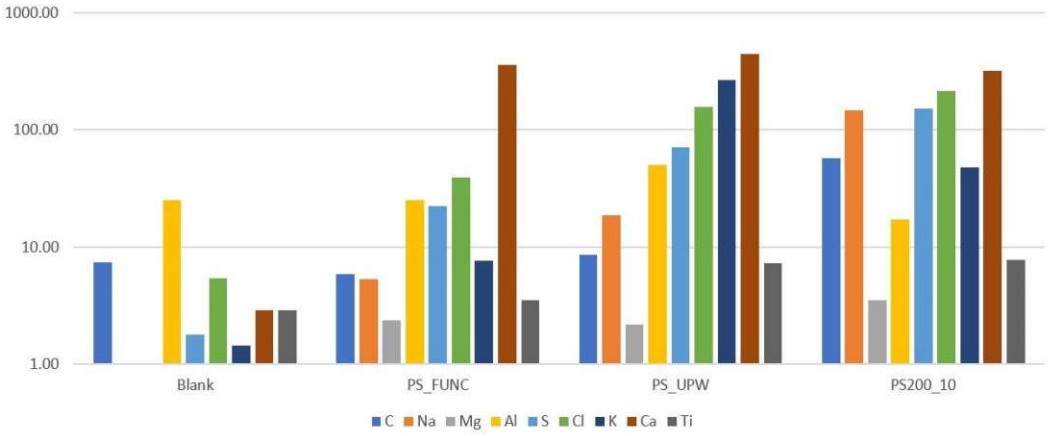

(a) Element intensities grouped by sample name, presented on a logarithmic scale.

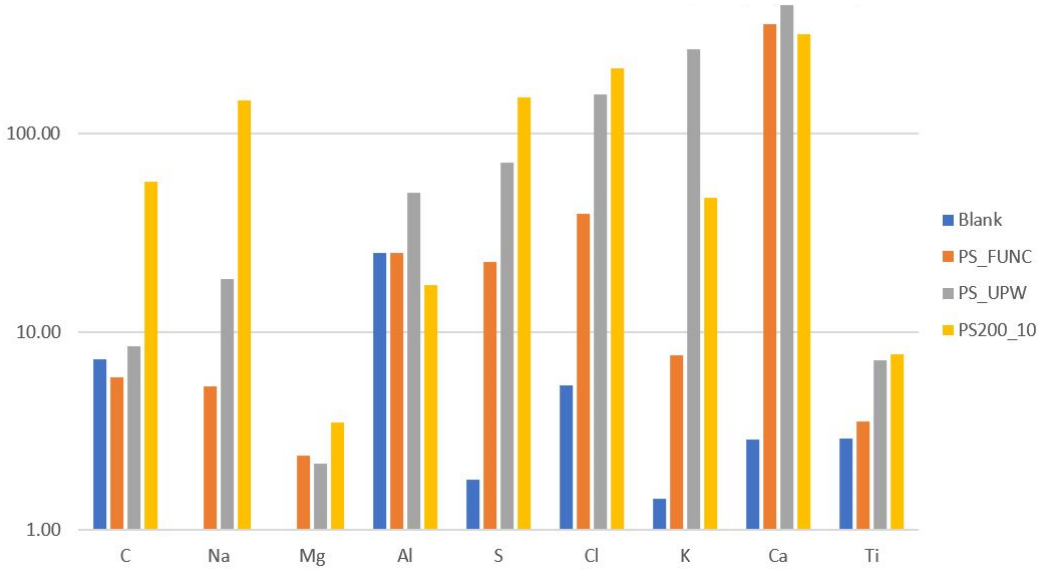

(b) Element intensities grouped by element, presented on a logarithmic scale.

Figure 62: Visual comparison of observed element intensities in the second series of spin coated samples at a glancing angle of around 0.24°.

In general, intensities of elements seem to increase after each step of the preparation process. Sodium, sulfur, chlorine and carbon exemplify this the best, as can be seen in Figure 62 b). Carbon shows expected behavior, as its intensity in the blank, functionalized and ultrapure water samples only slightly deviates from the blank value established by the calibration line. The intensity of the PS200_10 sample is off by a factor of 2 in comparison to the expectation drawn from the calibration data. Taking the carbon intensity directly from the scan at a glancing angle of 0.24°, a mass estimate of 684.74 ng can be calculated from an intensity of 57.38 cps using the calibration curve equation ($y = 0.076\frac{cps}{ng}x + 5.34cps$). As seen from Table 5, the surface density of carbon is known to be 10 ng/mm^2, which corresponds to a total mass of carbon of 324.6 ng for a surface of 32,46 mm^2. While this is by no means perfect, the estimate lands in the correct order of magnitude.

The other elements present could come from virtually any part of the preparation process. Sulfur most probably comes from the ligands present in the fluorescent dyes used to mark the polystyrene. Aluminum is present in the setup, and the various alkaline elements and chlorine could very well come from all the preparation steps that involve water. In fact, there is currently no guarantee for the level of cleanliness of the water used to dissolve the polystyrene spheres in. Titanium is not surprising, as the spectrometer is extremely sensitive to it, and the slightest amount would be detected. New measurements are currently being planned to further investigate the presence of these elements.

5.4 Further investigations

5.4.1 Background signal

During the measurements, especially when doing the carbon calibration, it was noticed that the background signal is pretty high in the low energy region, which is particularly relevant to quantification of carbon. Efforts were then undertaken to ascertain possible improvements to the spectrometer, although not much could be done due to time restraints.

Firstly, it was thought that the background signal came from electrons that were somehow getting through the electron trap. To confirm this, a sample was measured in atmospheric pressure, under the assumption that the air would absorb the incoming electrons and eliminate the extra background. Indeed, the observed spectrum showed a different background signal, which was lower in the low energy region of the spectrum.

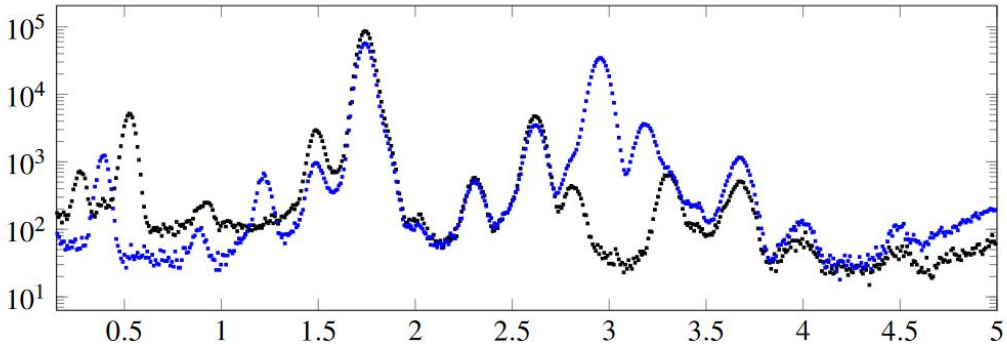

Figure 63: Measurements of a sample containing 250 ng of carbon in vacuum (black) and air (blue), both lasting 200 seconds.

After the presence of background electrons was confirmed, methods were discussed to reduce the signal. As a first measure, the influence of slits were tested. To test this, a sodium fluoride sample was measured under the same angle without the slit, with a slit of 250 microns, and with a slit of 50 microns. No difference was observed between any of the three spectra, ruling out slits as a possible solution to the background problem.

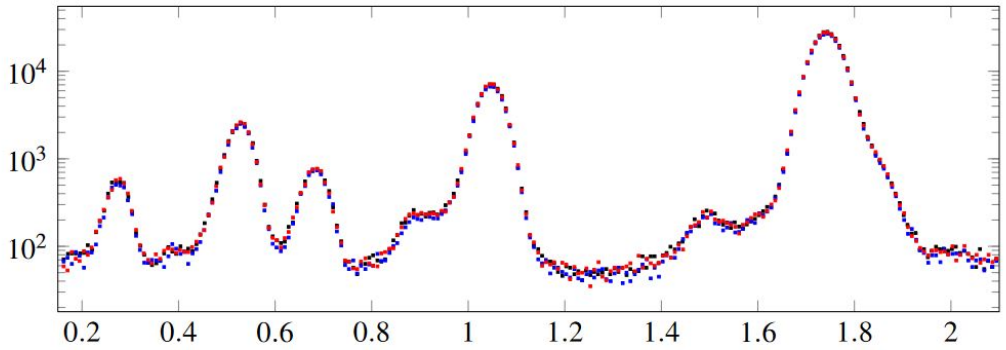

Figure 64: Measurements of a sample containing 250 ng of sodium fluoride using no slit (black), a 250 micrometer slit (blue) and a 50 micrometer slit (red). All measurements lasted 100 seconds.

Another proposed idea was to strengthen the magnetic field of the electron trap and thus reduce the number of electrons that reach the detector crystal. Since the idea of making a new collimator with a larger opening to fit the new detector was already proposed earlier, it was decided that the new collimator would have a 50 mm^2 opening, and be made out of iron, so that the iron between the magnets would magnify and focus the magnetic field, thus increasing its intensity. This collimator was manufactured and tested, but failed to provide any sort of bending magnetic field for the electrons, making the resulting spectrum entirely composed of electron noise. It is now clear that the rest of the collimator focused the magnetic lines of the two permanent magnets away from the collimator's opening, therefore having an effect completely opposite of the desired one.

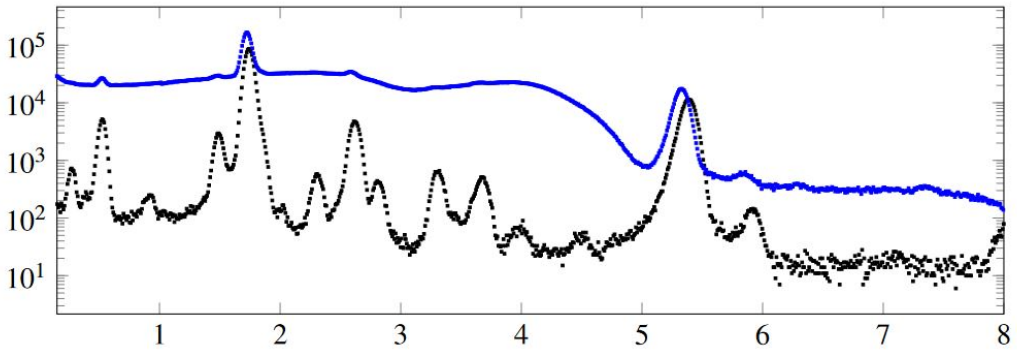

Figure 65: Measurements of a sample containing 250 ng of carbon done with the old copper collimator (black) and the new iron collimator (blue), both lasting 200 seconds.

5.4.2 Contaminant origin

As can be seen from the scan results presented above, a lot of contaminants were detected in the newly measured samples. Namely, strong fluorescence peaks of sodium, sulfur, chlorine, potassium, calcium and titanium were detected during measurement, especially when considering the PS200_10 sample (see Figure 57). The different intensities of these contaminants for the different samples suggest that different steps in the preparation process may have contributed to the intensity seen in the sample containing the polystyrene nanospheres. Closer inspection into the preparation process revealed a discrepancy between the inspected area value provided to the partners at the University of Utrecht (32.46 mm^2) and the true surface area inspected by the detector, which is 38.48 mm^2. This discrepancy was a result of misinterpretation of the technical drawings of the collimator made by L.Rachbauer, leading to false dimensions for the collimator being used for the inspected area calculations. After correcting for this, it could be concluded that the detector's inspected area was greater than the hydrophilic surface in the center of the reflector. It was then possible that the detector was seeing parts of the hydrophobic surface of the reflector, for which there was no guarantee of what contaminants would be present.

To test whether this fact had an impact on the measured spectra, a test was devised, wherein a sample would be placed inside the vacuum chamber, and all alignment steps properly carried out. With the exciting x-ray beam being reflected directly beneath the detector, the detector could manually be moved vertically up and down, thus changing its inspected area. The photomask used in sample preparation has a central hole 6.5 mm wide. In accordance with this fact, three positions for measurement were chosen:

1. Distance between the tip of the collimator and the surface of the reflector is 1 mm, which corresponds to an inspected area of 38.48 mm^2, or a circle with a 7 mm diameter. This position was used as a reference point, and is the position at which all the previous measurements were done.

2. Distance between the tip of the collimator and the surface of the reflector is 0.4 mm, which corresponds to an inspected area of 26.42 mm^2, or a circle with a 5.8 mm diameter. At this distance from the reflector, the detector is guaranteed to only see the hydrophilic part of the reflector.

3. Distance between the tip of the collimator and the surface of the reflector is 2 mm, which corresponds to an inspected area of 63.62 mm^2, or a circle with a 9 mm diameter. At this distance from the reflector, the detector is guaranteed to also see the hydrophobic part of the reflector.

The samples chosen for this testing were PS_FUNC and PS_UPW, as the high intensities of contaminants and carbon present in PS200_10 would probably make seeing any notable difference between the spectra recorded at different positions somewhat difficult.

Distance between collimator and reflector in mm	C cps	Si cps	Cl cps	Ca cps	Input countrate
0.4	32.24	30490.57	106.42	337.71	41457
1	28.62	29722.93	90.08	271.51	40130
2	20.9	30758.82	97.17	306.79	41712

Table 8: Intensities of carbon, silicon, chlorine and calcium depending on the distance from the collimator and the reflector for the PS_FUNC sample. Measurements were done for 100 seconds at the critical angle to boost the carbon fluorescence. No discernable discontinuity in intensity was observed.

Distance between collimator and reflector in mm	C cps	Si cps	Cl cps	Ca cps	Input countrate
0.4	30.99	20028.97	216.04	719.09	28160
1	25.05	20022.28	192.67	654.7	27899
2	17.27	20054.9	164.74	567.02	27571

Table 9: Intensities of carbon, silicon, chlorine and calcium depending on the distance from the collimator and the reflector for the PS_UPW sample. Measurements were done for 1000 seconds at the critical angle to boost the carbon fluorescence. No discernable discontinuity in intensity was observed.

If any of the elements are more strongly present in the outside hydrophobic area, then a jump in intensity should be visible when the hydrophobic area comes into view, most strongly for position 3. For all elements involved, there was no unexpected difference between the three spectra, suggesting that all the elements present in the spectrum are either spread across the whole surface of the reflector, or only concentrated in the hydrophilic part of the reflector, which the detector would see no matter the distance. These measurements prove the validity of the previously done angle scans, even with the additional surface visible, but imply possible contaminations during the preparation, handling or shipping of the samples. The discussion surrounding this issue is still ongoing as of the time of writing of this work.

6 Aluminosilicates

The second part of this work focuses on the measurements performed for I. Allegretta from the University of Bari, which concerned the chemical analysis of aluminosilicates with TXRF, with a focus on light elements like magnesium and sodium. To this end, six different certified reference materials (CRM) of aluminosilicate rocks were measured, and the calibration data was used to quantify three other aluminosilicate reference materials with the internal standard method for validation. For each element, the recovery rates were calculated, which are ratios between the concentration data obtained with the internal standard method and the certified concentration data for a particular CRM.

Name of CRM	Purpose
MICA-Mg (Phlogopite)	Calibration
ZW-C (Zinnwaldite)	Validation
DR-N2 (Diorite)	Validation
GS-N (Granite)	Validation
UB-N (Serpentine)	Calibration
AL-I (Albite)	Calibration
AN-G (Anorthosite)	Calibration
BE-N (Basalt)	Calibration
WS-E (Dolerite)	Calibration

Table 10: List of CRM used. For each CRM, three wafers were pipetted with the sample solution. Compositions of all the CRM can be found in Ref. [3]

The samples were to be measured for 1000 seconds each, at half the critical angle of quartz, at 30 kV and 30 mA. However, during measurement it was observed that the input rates observed by the detector were above the detector's choking point. To ensure this was not the case, the current of the x-ray generator was lowered to 10 mA, which put the input rate back into an acceptable range.

The results from the measurement of the six calibration CRM samples were used to obtain sensitivity data relative to silver, which was added as an internal standard during sample preparation. Silver was chosen because it's Lα lines are at an energy of around 3 keV, which results in very strong excitation and no overlap with the elements present in the samples.

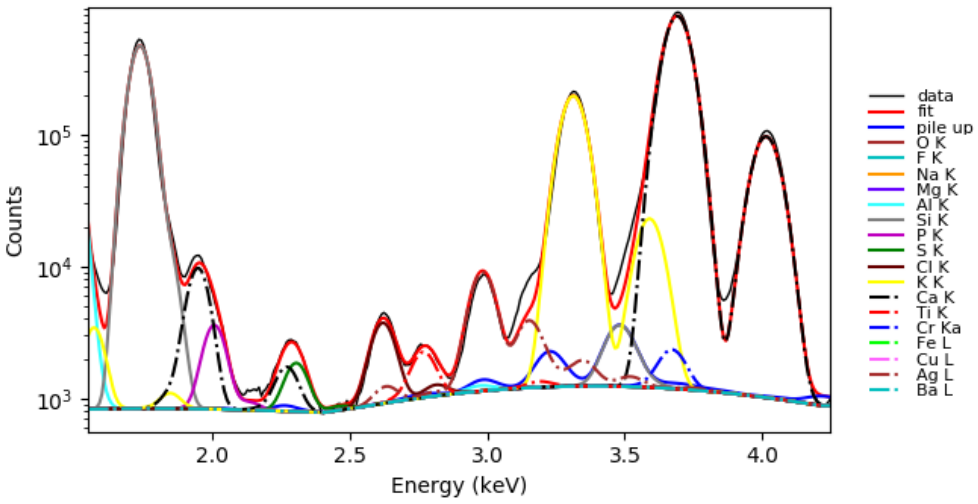

(a) Close-up of a spectrum, showing the overlaps of the calcium $K\beta_1$ escape peak (black dashed line) with the phosphorus K line (purple) and the sulfur K line (dark green).

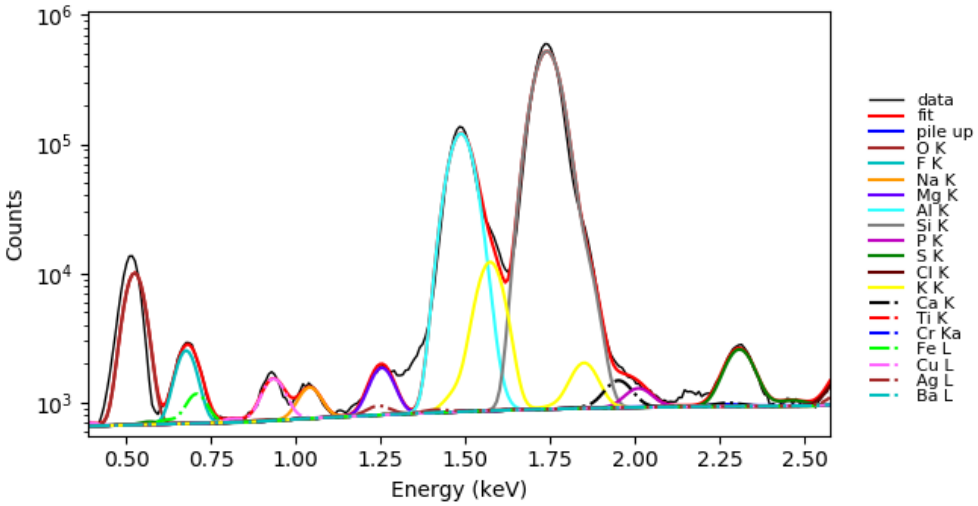

(b) Close-up of a spectrum, showing the overlap of the iron $L\alpha_1$ line and the fluorine K line (dark cyan).

Figure 66: Examples of overlaps that plague the multielement spectra of CRMs used during calibration and validation. Figures from Ref. [4].

A few facts need to be pointed out concerning a few of the elements for which the quantification is more challenging due to the circumstances.

- Phosphorus (2.01 keV) overlaps with the Ca-Ka escape peak (1.95 keV) in the spectra, so the measured intensity can be unreliable. The calcium escape peak can be rather pronounced as calcium was usually present in high concentrations in the samples measured.

- Sulfur (2.31 keV) suffers from the same issue as mentioned above, and overlaps with the Ca-Kb escape peak (2.27 keV). To minimize the impact of this fact on the obtained data, two calibration samples with the highest concentrations of calcium were not taken into account when calculating the sensitivity value for sulfur.
- Iron is detected and quantified using its L lines, which are rather weak and overlap with fluorine's K line, leading to poor counting statistics and less reliable results.
- Silicon is present in the samples as well as in the substrate, so higher deviations are to be expected, depending on geometrical factors and penetration depth.

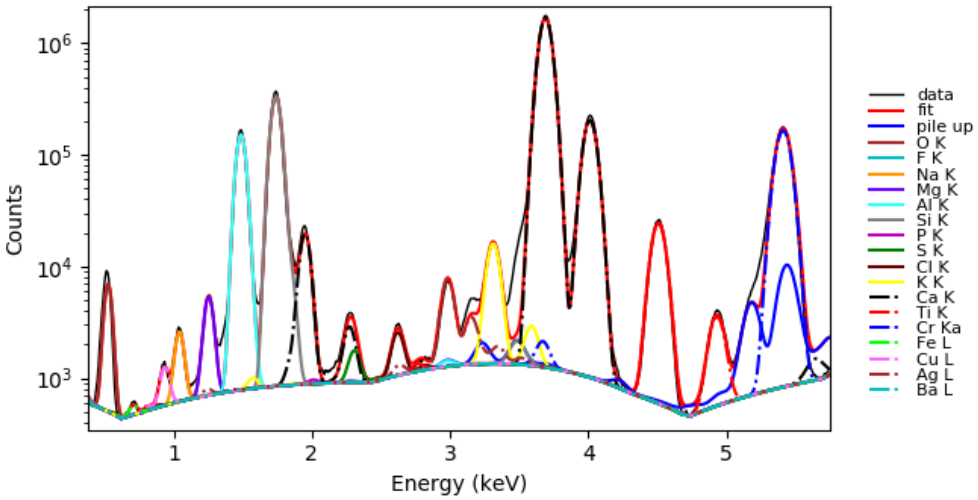

(a) Example AN-G spectrum.

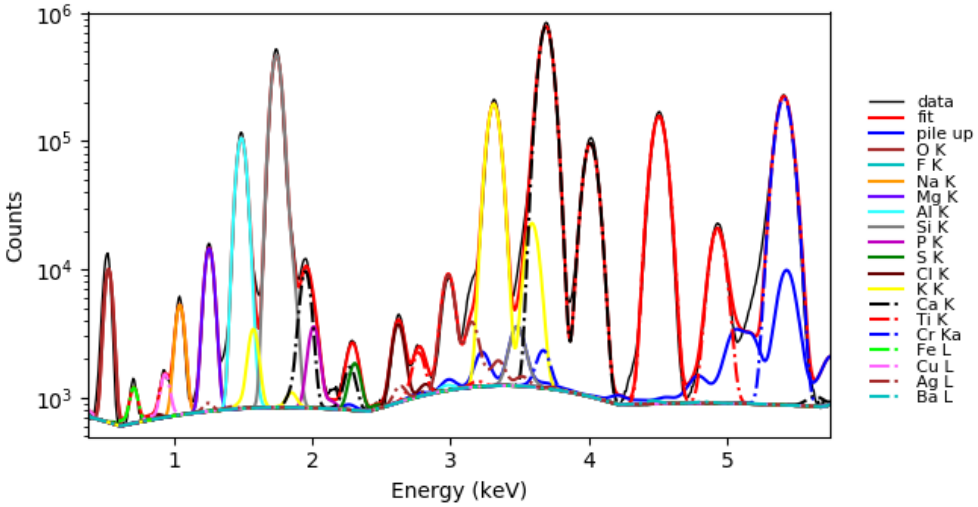

(b) Example DR-N2 spectrum.

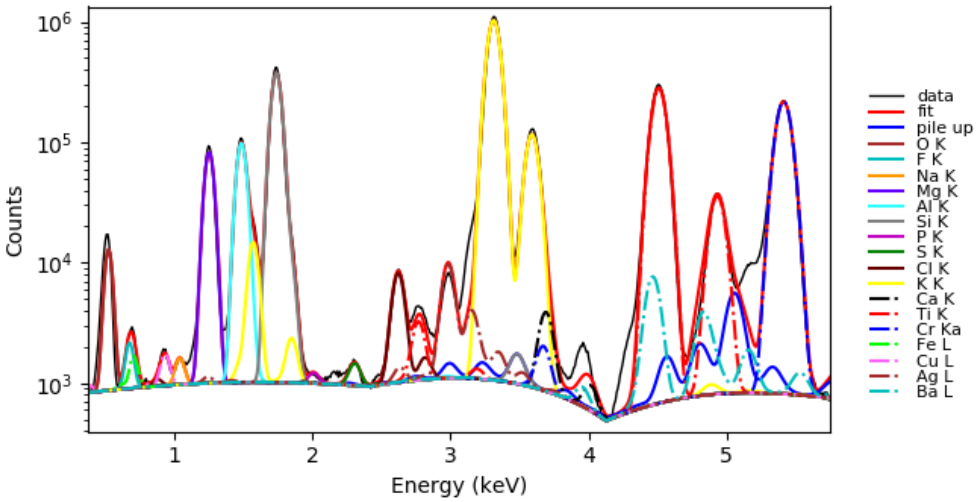

(c) Example MICA-Mg spectrum.

Figure 67: Example spectra of some of the calibration CRM. Fitting and evaluation was done by I. Allegretta in PyMCA. Figures from Ref. [4].

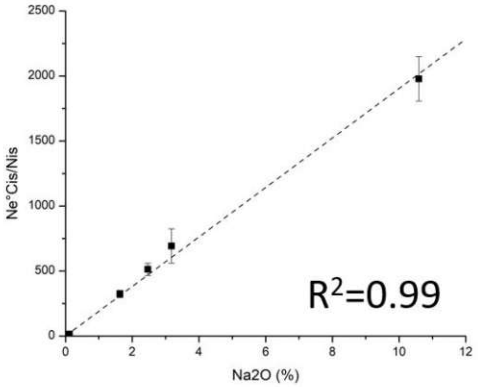

(a) Na_2O sensitivity

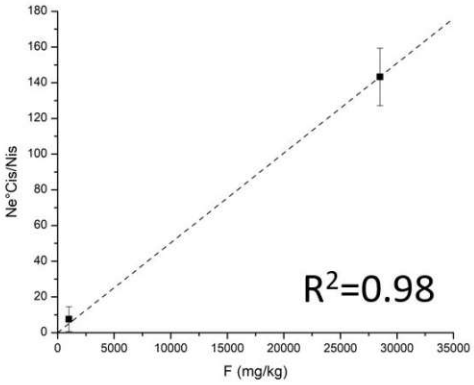

(b) F sensitivity

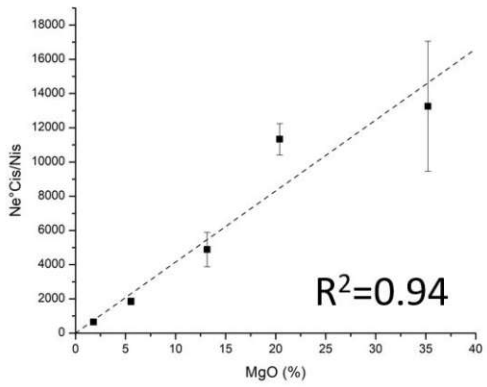

(c) MgO sensitivity

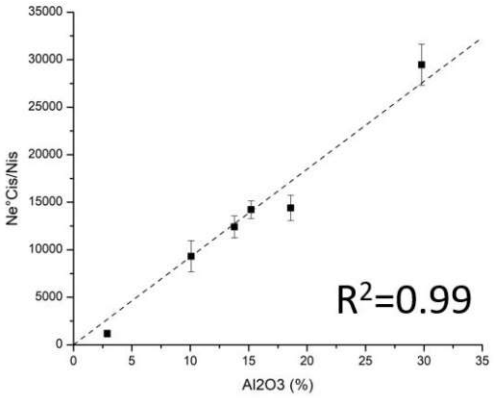

(d) Al_2O_3 sensitivity

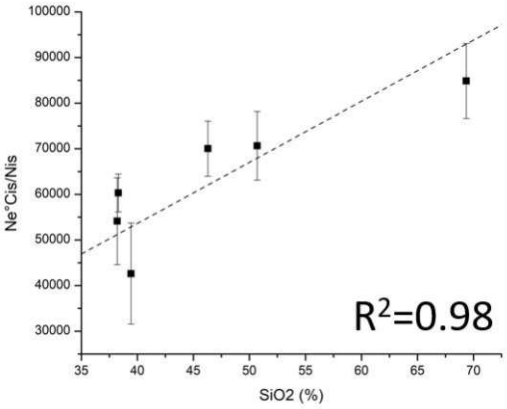

(e) SiO_2 sensitivity

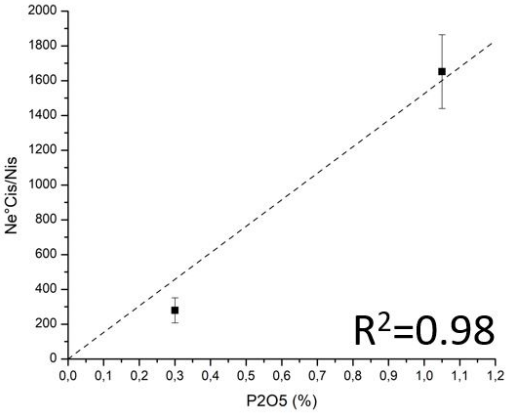

(f) P_2O_5 sensitivity

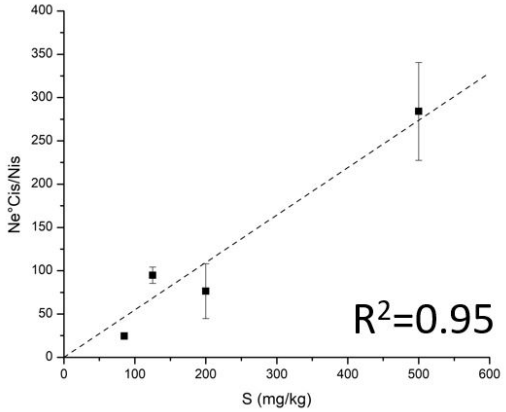

(g) S sensitivity

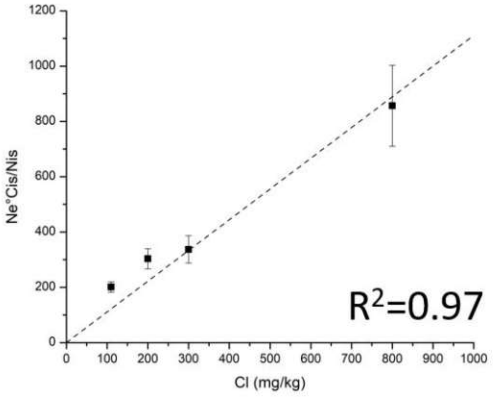

(h) Cl sensitivity

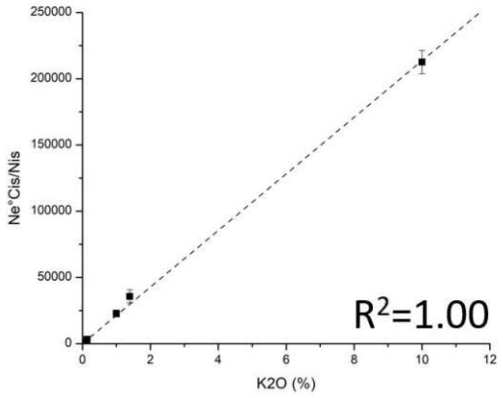

(i) K_2O sensitivity

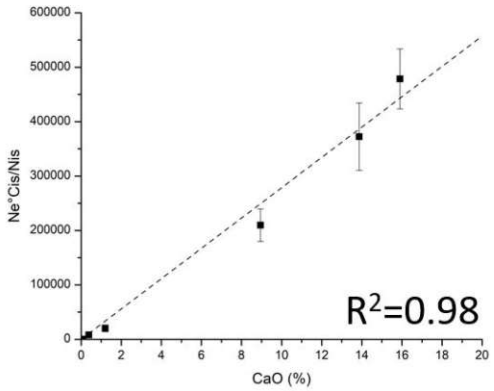

(j) CaO sensitivity

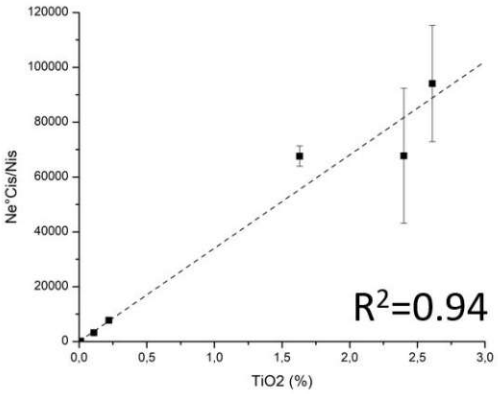

(k) TiO_2 sensitivity

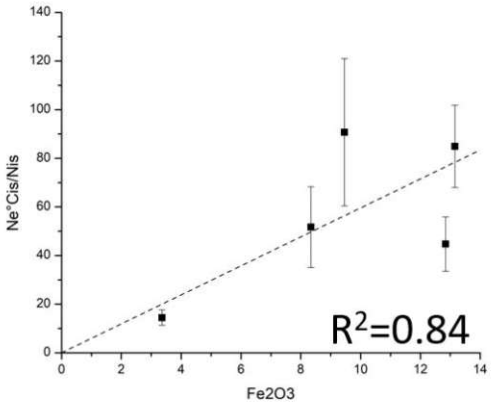

(l) Fe_2O_3 sensitivity

Figure 68: Calibration data obtained from aluminosilicate CRM measurements. Figures from Ref. [4]

As can be seen from the figures above, the data shows good linearity for all elements except the above mentioned problematic ones. Special focus should be put on the results obtained for sodium, fluorine and magnesium, as these are the lightest elements this spectrometer can detect, and the main reason it was picked for this task. It should be noted that two of the CRM used for calibration contained fluorine, resulting in only two data points in the sensitivity graph. The other two CRM that contained fluorine were used for validation. If these data points are added to the sensitivity plot, the linearity is respected and the sensitivity stays the same. Because of this, it was deemed sufficient to use only two data points for calculating fluorine's relative sensitivity to silver.

The calibration data was validated by measuring the ZW-C, CS-N and DR-N samples, again with a known concentration of silver added as an internal standard. Using the relative sensitivity values obtained from the calibration data, concentrations of the detected elements

can be calculated from the measured intensities and compared to the certified values for the CRM in question. This comparison is done by calculating recovery values for each element, which are simple ratios between the concentration values calculated with the internal standard method, and the certified concentration values for that particular CRM.

CRM		Na2O	MgO	Al2O3	SiO2	P2O5	K2O	CaO	TiO2	Fe2O3	F	S	Cl
ZW-C	Average	0,46	0,14	20,99	67,75	0,02	7,93	0,35	0,05	14,72	54826	434	118
	std.dv	0,09	0,03	3,83	10,49	0,01	1,56	0,07	0,01	2,96	10037	108	2
	Recovery	139,02	87,01	113,74	125,47	72,88	102,73	93,99	100,83	155,57	101	145	393
	Err%	20,21	20,80	18,25	15,48	35,56	19,69	19,55	20,35	20,13	18	25	2
GS-N	Average	4,17	2,45	15,21	73,22	0,12	4,98	2,36	0,81	3,63	998	151	524
	std.dv	0,29	0,12	0,65	4,74	0,02	0,10	0,12	0,03	0,48	48	14	16
	Recovery	110,60	106,57	103,70	111,27	44,32	107,64	94,32	119,47	96,81	95	108	116
	Err%	6,94	4,99	4,29	6,48	17,44	2,04	5,17	4,29	13,34	5	9	3
DR-N	Average	2,93	4,08	15,66	51,94	0,11	1,70	5,73	1,01	11,20	1004	299	417
	std.dv	0,70	0,86	3,14	11,67	0,01	0,23	1,04	0,15	2,57	984	26	58
	Recovery	98,15	92,64	89,36	98,28	42,22	100,28	81,26	92,83	115,49	201	86	104
	Err%	23,97	21,10	20,02	22,48	11,18	13,59	18,18	14,59	22,96	98	9	14

Figure 69: Recovery values for the inspected elements in the CRM samples used for validation. Table from Ref. [4]

CRM	Na2O	MgO	Al2O3	SiO2	P2O5	K2O	CaO	TiO2	Fe2O3	F	S	Cl
	%									mg/kg		
ZW-C	0,33	0,16	18,45	54,00	0,025	7,72	0,37	0,05	9,46	54500	300,00	30,00
GS-N	3,77	2,3	14,67	65,8	0,28	4,63	2,5	0,68	3,75	1050	140,00	450,00
DR-N	2,99	4,4	17,52	52,85	0,25	1,7	7,05	1,09	9,7	500	350,00	400,00

Figure 70: Given concentration values for the inspected elements in the CRM samples used for validation. Table from Ref. [4]

As can be seen in the tables above, good recovery values are obtained for most elements, with a few caveats. As expected, the elements listed above as being problematic have indeed proven to give worse recovery values, especially phosphorus due to its overlap with the CaKα escape peak. Sodium also shows subpar recovery in samples where it is present in small concentrations. This might be influenced by the low concentration in those samples, compounding the poor excitation of sodium and the absorption effects. Another thing of note is the high error value, showing the large deviations observed in the intensities of elements in materials ZW-C and DR-N.

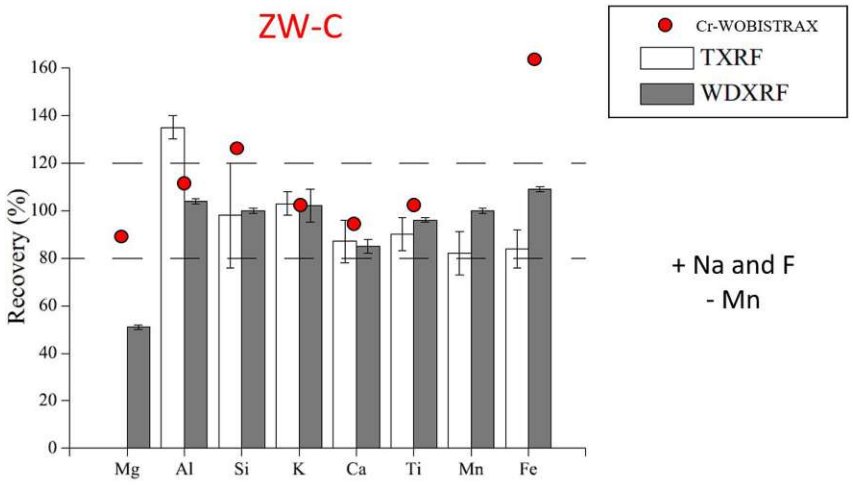

Figure 71: Comparison of the recovery rates (ratio between calculated and measured values) for the different x-ray methods used to quantify aluminosilicate samples. Figure from Ref. [4].

Figure 63 shows the comparison between recovery rates for the different methods used to quantify aluminosilicates, differentiating between standard WDXRF and TXRF setups, as well as the specific TXRF spectrometer used in this work. Most elements have acceptable recovery rates, with the exception of silicon, which is present in the substrate, and iron, which is quantified using the weaker L lines. The notable advantage that this setup has over the previously used spectrometers is its ability to provide better results for magnesium, as well as the option to quantify fluorine and sodium. Both of these elements are very important for chemical analysis of soil and clay samples, and this fact cannot be understated.

7 Conclusion

As can be seen from the results discussed above, the instrument is well suited to light element analysis. Quantification of the aluminosilicate certified reference materials shows good performance over a range of elements relevant for mineralogical studies. The measurements of the polystyrene nanospheres, while difficult to quantify, demonstrate a working concept. Improvements are still possible, however.

Firstly, the instrument could benefit from a dual anode x-ray tube, one which combined chromium and a heavier metal, like rhodium or tungsten. This was suggested by I. Allegretta, and this addition to the TXRF technique in general would broaden the spectrum of elements that could be measured and quantified. This is especially useful for mineralogical and geological studies, as quantification of metals alongside lighter elements is useful in analyzing the chemical composition of clays and soil with a single spectrometer.

Secondly, the measured spectra show a significant background signal, especially in the low energy regions. This hampers the spectrometer's ability to detect extremely low quantities of the lightest elements, most notably carbon. The current working theory is that this background comes from Auger and photoelectrons, so improving the electron trap should mitigate this problem. While the experiment with the iron collimator was ultimately unsuccessful, finding stronger permanent magnets of a similar size to the ones being used now seems like the next step.

Furthermore, the addition of an x-ray reflectivity detector might help with quantifying the polystyrene nanosphere samples, or any similar samples for which depth information is required. While the camera that is currently in place makes operation of the instrument more convenient, an x-ray reflectivity detector might be used in the same manner to allow for easier alignment, while also providing additional valuable data for quantification.

Finally, even though quantification of the carbon nanosphere samples has proven to be quite the challenge, the instrument is very capable of detecting carbon with good statistics and giving insight into phenomena occurring during the deposition process. Due to time constraints, no more samples could be analyzed, but future work should focus around careful quantification of different samples with controlled deposition parameters, in order to get a full picture of how sensitive the spectrometer is to particle size and particle density.

8 References

1. Klockenkaemper, R., von Bohlen, A. (2015). *Total-reflection X-ray fluorescence analysis and related methods.—Second edition.* ISBN 978-1-118-46027-6.

2. https://www.amptek.com/internal-products/70-mm2-fast-sdd.

3. https://sarm.cnrs.fr/pages/geostandards.php#.

4. Allegretta, I., Krstajic, D., Wobrauschek, P., Kregsamer, P., Ingerle, D., Streli, C., Terzano, R. (2022). *Direct analysis of light elements in aluminosilicates using a Low-Z TXRF spectrometer.* EXRS 2022. *(To be published)*

5. Rachbauer, L. (2020). *Towards quantification of carbon in nanoplastic samples using TXRF: Optimization and Characterization of a low-Z spectrometer.* Diploma thesis, TU Wien.

6. *A Diagram of the Electromagnetic Spectrum, Showing the Type, Wavelength (with Examples), Frequency, the Black Body Emission Temperature. (2007)*
URL: https://commons.wikimedia.org/wiki/File:EM_Spectrum_Properties_edit.svg

7. W. Demtroder (2004). *Experimentalphysik: Elektrizitat und Optik, 3. Edition, Springer*.

8. A. A. Araneda (2015). *Development of a methodology for the determination of a TXRF spectrometer sensitivity curve*. DOI:10.13140/RG.2.2.18736.92163

9. K. Maher (2001). *The x-ray energy spectrum generated by an x-ray tube.* URL: https://commons.wikimedia.org/w/index.php?curid=12711485

10. Bury, C.S., Brooks-Bartlett, J.C., Walsh, S.P. and Garman, E.F. (2018), *Estimate your dose: RADDOSE-3D.* Protein Science, 27: 217-228. https://doi.org/10.1002/pro.3302

11. J. Tuszynski (2007). *Mass attenuation coefficient of iron with contribution sources of attenuation. Wikipedia, the free Encyclopedia*.
https://commons.wikimedia.org/wiki/File:Attenuation_Coefficient_Iron.svg

12. S. Singh, R. Versaci, A. Laso Garcia, L. Morejon et al. (2018). *Compact high energy x-ray spectrometer based on forward Compton scattering for high intensity laser plasma experiments.* Rev. Sci. Instrum. 89, 085118; https://doi.org/10.1063/1.5040979

13. J. Hyun, P. Plot, T. Sen (2018). *Optics and bremsstrahlung estimates for channeling radiation experiments at FAST.* URL: https://www.researchgate.net/publication/323276352_Optics_and_bremsstrahlung_estimates_for_channeling_radiation_experiments_at_FAST.

14. A. Attwood, *Reflection and Refraction* (2004). UC Berkley EE213 & AST210.
https://people.eecs.berkeley.edu/attwood/sxr2009/lecnotes/04_Reflection_And_Refraction_2009.pdf.

15. G. R. Putland (2019). *Behavior of a ray incident from a medium of higher refractive index n_1 to a medium of lower refractive index n_2, at increasing angles of incidence.* URL: https://commons.wikimedia.org/wiki/File:ReflexionTotal_en.svg

16. *Surfactant datasheet* (2016). Polysciences Inc. URL: https://www.polysciences.com/india/awfile/index/attach/file/TDS_912.pdf/

17. *Fluorophore reference listing*. Polysciences Inc. URL: https://www.polysciences.com/india/awfile/index/attach/file/SS_PSI_Fluorophore_Ref_Listing.pdf/

18. Larson, R. G. (2017). *In Retrospect: Twenty years of drying droplets*. Nature vol. 550 466–467.

19. Deegan, R. D. et al. (1997). *Capillary flow as the cause of ring stains from dried liquid drops*. Nature 389, 827–829.

20. Sahu, N. & Panigrahi, S. (2009). *Fundamental understanding and modeling of spin coating process: A review*. Indian J. Phys vol. 83.

21. Prost, J., Wobrauschek, P., Streli, C. (2018). *Dual energy-band excitation from a low power Rh anode X-ray tube for the simultaneous determination of low Z and high Z elements (Na-U) using total-reflection X-ray fluorescence analysis (TXRF)*. Review of Scientific Instruments, 89(9), 093108. https://doi.org/10.1063/1.5044527

22. Wobrauschek, P. (2007). *Total reflection x-ray fluorescence analysis-a review*. X-Ray Spectrometry, 36(5), 289–300. https://doi.org/10.1002/xrs.985

23. Streli, C. (2007). *Total Reflection X-Ray Fluorescence Analysis of Low Z elements: Development and Applications*. In C. Vazquez (Ed.), Topics in X-Ray Spectrometry (pp. 95–103). Comision Nacional de Energia Atomica; CNEA. https://doi.org/10.1002/xrs.1300200106

24. Hoefler, H., Streli, C., Wobrauschek, P., Óvári, M., Záray, G. (2006). *Analysis of low Z elements in various environmental samples with total reflection X-ray fluorescence (TXRF) spectrometry*. Spectrochimica Acta Part B: Atomic Spectroscopy, 61(10–11), 1135–1140. https://doi.org/10.1016/j.sab.2006.07.005

25. Rauwolf, M., Ingerle, D., Pemmer, B., Wobrauschek, P., Streli, C., Pahlke, A. (2014). *Low Z TXRF measurements with a new Ketek SDD detector*. EXRS2014.

26. Bambynek, W., Crasemann, B., Fink, R. W., Freund, H.-U., Mark, H., Swift, C. D., … Rao, P. V. (1972). *X-Ray Fluorescence Yields, Auger, and Coster-Kronig Transition Probabilities*. Reviews of Modern Physics, 44(4), 716–813. URL: https://doi.org/10.1103/RevModPhys.44.716

27. Ingerle, D., Pepponi, G., Meirer, F., Wobrauschek, P., & Streli, C. (2016). *JGIXA — A software package for the calculation and fitting of grazing incidence X-ray fluorescence and X-ray reflectivity data for the characterization of nanometer-layers and ultra-shallow-implants*. Spectrochimica Acta Part B: Atomic Spectroscopy, 118, 20–28. https://doi.org/10.1016/j.sab.2016.02.010